Department of Precision and Microsystems Engineering

# Pressure monitoring inside the nozzle of a fused filament fabrication 3D printer

S. de Vries

Report no : 2022.076
Coach : Dr. P. Fanzio
Professor : Asst. Prof. C. Ayas
Specialisation : High-Tech Engineering
Type of report : Master thesis
Date : December 16, 2022

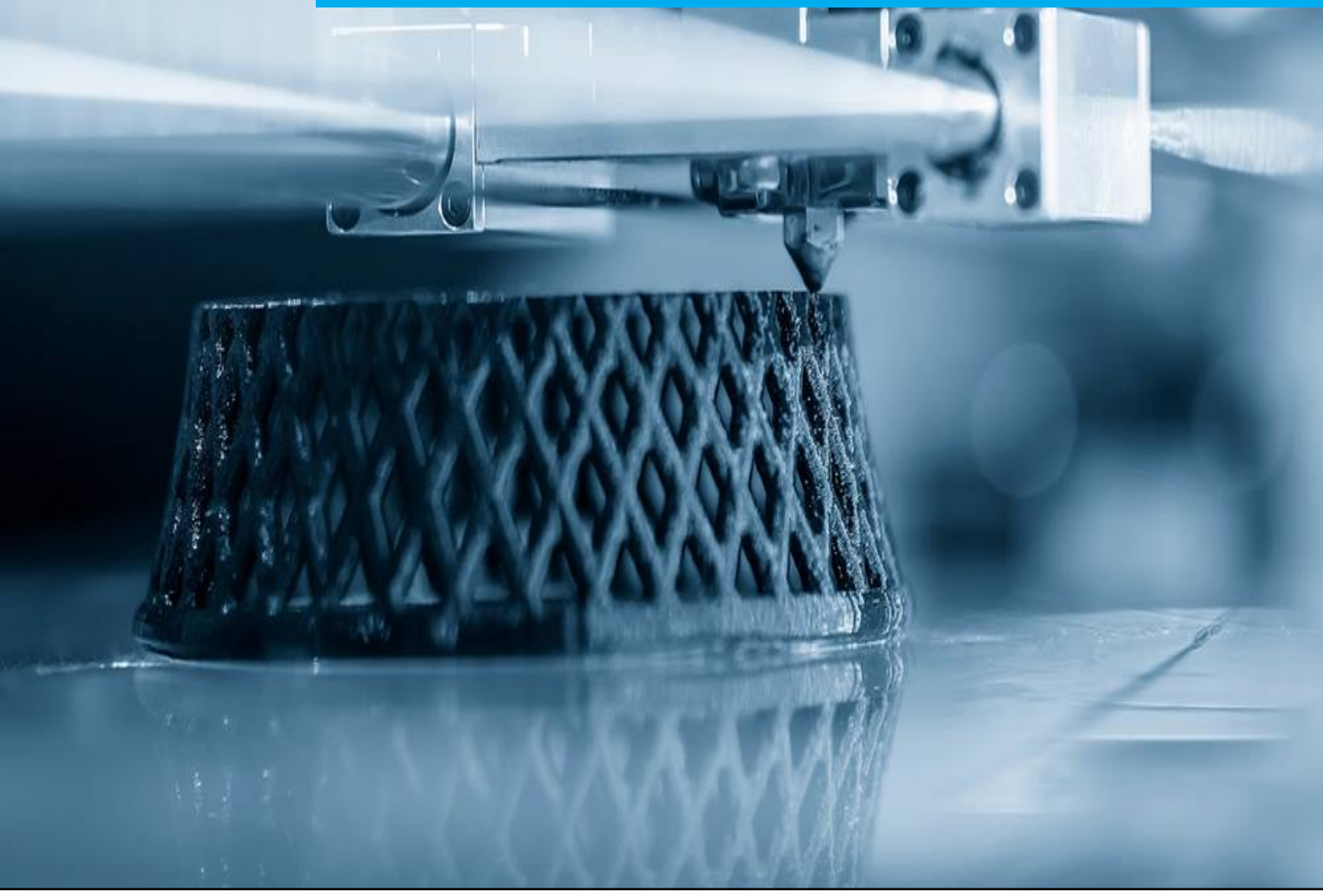

TU Delft Delft University of Technology

Challenge the future


A collaboration between UltiMaker and Delft University of Technology

# Graduation Internship

Pressure monitoring inside the nozzle of a fused filament fabrication 3D printer

by

**S. de Vries**

In partial fulfillment of the requirements for the degree of

**Master of Science**

in

**Mechanical Engineering**

*Author:*
S. de Vries sietse.devries@hotmail.com

*TU Delft Supervisor:*
Asst. Prof. C. Ayas c.ayas@tudelft.nl

*Ultimaker Supervisors:*
Dr. P. Fanzio paola.fanzio@ultimaker.com
S. T. Kent, MEng sam.kent@ultimaker.com
J.A.T. van der Hilst j.vanderhilst@ultimaker.com

December 11, 2022

# Contents

# 1 Preface

My first contact with 3D printing was during my BSc thesis, where I used 3D printed parts as an aid to build a model rowboat. I did not know much about the technology, other than that it was relatively new and that I was immediately intrigued by it. During the first lockdown of the Covid pandemic, I bought a cheap 3D printer to explore a creative indoor hobby. It was a success, I loved it. To be able to create any shape you can imagine, right in your own house, within a few hours is absolutely astonishing. My interest grew and at some point I asked myself: 'You study High-Tech Engineering, why not combine your education with your hobby and find a graduation project in the field of 3D printing?' I did some research to find interesting 3D printer companies in the Netherlands and I quickly landed at Ultimaker, which I knew for their slicing software Cura. I phoned them and asked if they had a research project. This graduation thesis is the result.

I am really happy to be able to contribute to such a fascinating technology, which is still relatively unexplored. The potential of the technology is huge and I am very curious what the future holds. I would like to thank Janine van der Hilst, Louise Plas and Paola Fanzio for their quick collaboration to set-up this graduation project on a short notice. Secondly, I would like to thank Paola Fanzio and Sam Kent for supervising me through the entire project and always being on standby to advice or help me. Thirdly, many thanks to the employees of Ultimaker who showed a lot of interest, offered their help and wanted to contribute to the project such as Koos Welling, Maqsood Alam, Ron van Dorssen, Siert Wijnia, Marc Joosen and Johan Versteegh. I am also grateful for the interesting and motivating conversations with Francisco Galindo-Rosales and Tomás Schuller Almeida Graça Barbosa from University of Porto. Last but not least, I would like to thank Can Ayas for supervising me on behalf of Delft University of Technology and together with Angelo Accardo and Paola Fanzio forming the graduation committee.

# 2 Introduction

At the brink of the fourth industrial revolution, additive manufacturing (AM), commonly referred to as 3D printing, is a vital and uprising technology [1]. In contrast to conventional manufacturing methods, AM techniques add material layer-by-layer to form three-dimensional objects. This opens up the possibility to construct complex geometries because it is not limited by the accessibility of removal tools [2–4]. This design freedom can be beneficial in a wide range of applications. The aerospace and automotive industries use AM because it enables them to manufacture strong and lightweight components [5]. Architects, designers and engineers use AM to be able to quickly visualise complex physical models [6, 7]. Pharmacists, doctors and dentists use AM to produce custom-tailored drugs and implants [8–11].

## 2.1 Fused Filament Fabrication

Additive manufacturing is the overarching term for various different layer-by-layer manufacturing techniques. Fused filament fabrication (FFF) is the most used AM technique [2] that uses extrusion of molten polymers.

### *2.1.1 Working principle*

With the help of computer-aided design (CAD) software, any 3D object can be virtually modelled and transferred into stereolitography (STL) files [5]. Slicing software is used to decompose STL files into a multitude of stacked 2-dimensional layers; slices. Slicing of a 3D object is shown in Figure 1.

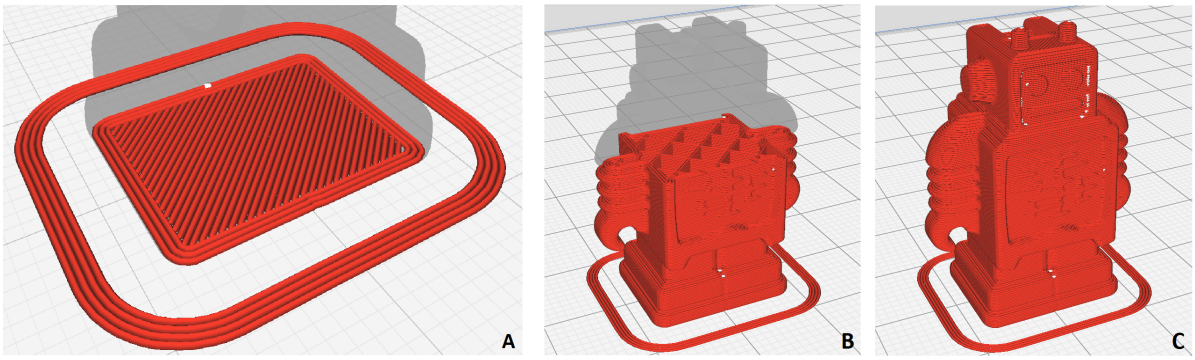


Figure 1: Slicing of a 3D object by Ultimaker Cura (slicing software). In red: (A) shows the first layer of the object and the lines that make up the layer, (B) shows the object after 80 layers will have been deposited and (C) shows the completed object.

The slicing software translates a single layer into a set of lines (Figure 1A) which is saved as a g-code file that the FFF based 3D printer can read.

The printer uses an extruder motor with a feeder gear to push solid polymer filament into a heated liquefier to melt the material. The solid filament, which is not heated yet, enters the liquefier and serves as a piston to push the molten material through a nozzle [12]. A schematic of this process is shown in Figure 2.

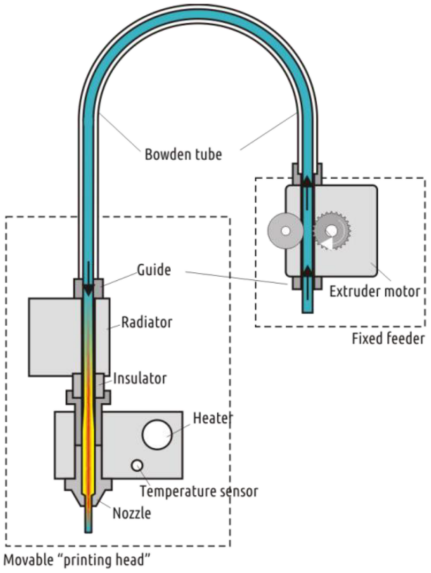


Figure 2: Schematic of the printing process in an FFF based 3D printer. Image from Kuznetsov et al [13].

The 3D printer has a moveable printhead which moves in the desired pattern in the horizontal plane while extruding to lay down a single layer of molten polymer on top of a platform called printbed. The deposited material cools down and solidifies. After the first layer has been deposited, the nozzle moves up with respect to the printed object. The printer then moves its printhead while extruding to deposit a second layer on top of the previous one. This process is repeated until all the layers are deposited and the final 3D object is created. An illustration of the working principle is shown in Figure 3.

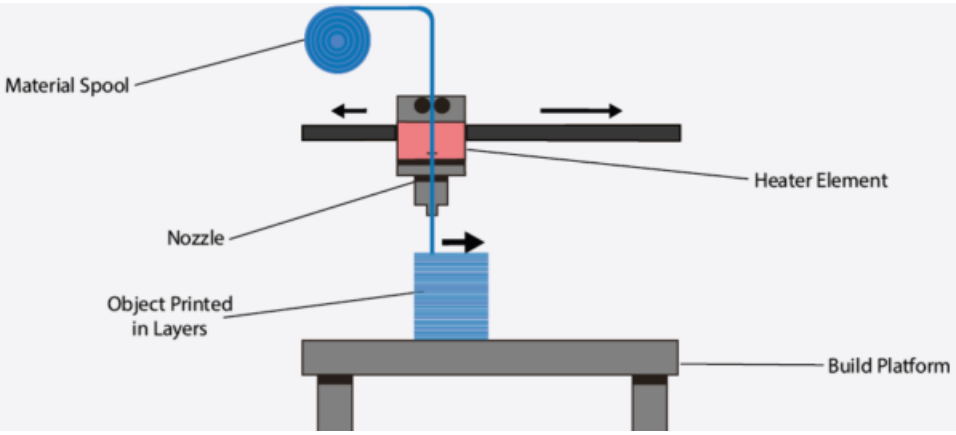


Figure 3: The working principle of an FFF based 3D printer. Image from `https://pick3dprinter.com/fff-3d-printer/`.

### *2.1.2 Application*

Currently, FFF is used mainly for rapid prototyping [14]. Due to its low investment cost, engineers and designers are enabled to quickly produce and improve iterations of prototypes. With the help of FFF they can cheaply speed up the design process. Researchers and students can rapidly reproduce models for analyses, comprehension and other educational purposes [5],[15].

Due to the advancements of printers and materials on the market, FFF is increasingly used to manufacture end-of-use parts as well. However, there is much to be improved before FFF can be

considered a revolutionary manufacturing technique. It has yet to become a reliable technique to repeatedly create end-of-use, custom-made parts that are not only visually acceptable, but also mechanically strong. To achieve this, a deeper understanding of the extrusion process is required.

## 2.2 Extrusion process

The extrusion process is the part of the printing process where the filament is melted in the liquefier and pushed out through an outlet onto the printbed. The liquefier consists of a cold-end and a nozzle. A simple illustration is shown in Figure 4.

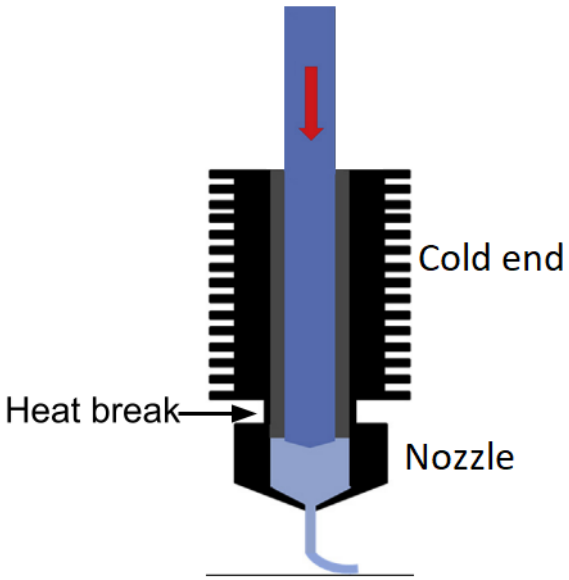


Figure 4: Illustration of the liquefier consisting of a cold-end and a nozzle. Image from Filmer et al. [16].

Filament enters the liquefier from the top and is pushed down the cold-end into the nozzle. The nozzle is a heated chamber that melts the polymer so that it can flow through an outlet called 'nozzle die'. That way the molten polymer is extruded onto the printbed. The still solid filament acts as a plunger to push the molten filament out. The cold-end is an actively cooled chamber to make sure that the incoming filament remains solid. The cold-end and nozzle are separated by a heat break; a thin-walled cylinder that prevents heat exchange.

### *2.2.1 Print quality*

The effect of the extrusion process on the print quality can be categorised into three aspects; visual quality, mechanical quality and print productivity. The visual quality of a print is purely based on aesthetics. The 3D printing community often uses a benchmark print in the shape of a small steamboat to assess the visual properties of a print, shown in Figure 5. There are numerous phenomena happening during the printing process that negatively influence the visual quality, a lot of which is due to uncontrolled extrusion.

Figure 5: Two benchmark boats. The one on the left shows clearly visible defects and inconsistencies, whereas the boat on the right already shows more improvements. Image from `https://www.youmagine.com/contributions/591`.

Examples are under-extrusion, over-extrusion and stringing. Under-extrusion happens when too little molten material is pushed out of the nozzle die and causes voids in the print. Over-extrusion happens when too much molten material is pushed out of the nozzle which results in excess material on the outside of the print. Stringing happens when molten polymer oozes out of the nozzle die when the printhead moves over an open area; an area in which no filament should be extruded. Figure 6 shows these errors.

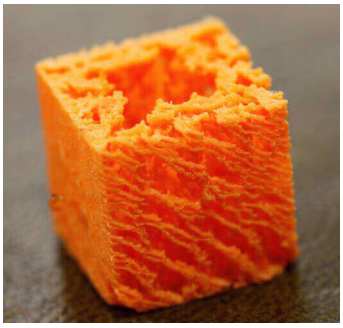

(a) Under-extrusion causes voids in the print.

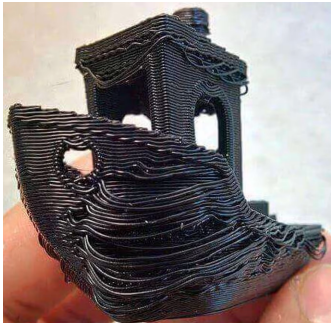

(b) Over-extrusion causes excess material in the print.

(c) Stringing is caused by unwanted oozing of the melt.

Figure 6: Images from `https://all3dp.com/1/common-3d-printing-problems-troubleshooting-3d-printer-issues/`

Two visually identical parts can differ in properties such as brittleness, stiffness and yield strength [17]. Moreover, chemical properties, wear resistance and dimensional accuracy can be included in print quality evaluation. Mechanical quality depends on the type of filament and the extrusion process. For example, under-extrusion weakens the printed part.

Print productivity has to do with the time it takes to produce a printed object. It is a combination of print speed and reliability. Faster prints increase production saving time and reducing production costs. However, printing fast is not productive if it takes twice to get the print right. Usually, a trade-off is chosen between visual or mechanical properties and print productivity. At higher printing speeds, more material must be deposited in the same time window. This means a faster melt flow and a larger heat flux. Therefore, the extrusion process greatly influences the print productivity.

Slice settings (such as layer height) and printer hardware influence print quality. Companies are continually competing to put the best slicing software and 3D printers on the market. However, extrusion is relatively hard to control and causes a major roadblock in the development of 3D printers [18]. Unreliable extrusion causes unpredictable deficiencies such as nozzle clogging and inconsistent extrusion. Unpredictable, inconsistent extrusion is unacceptable when pursuing high quality prints.

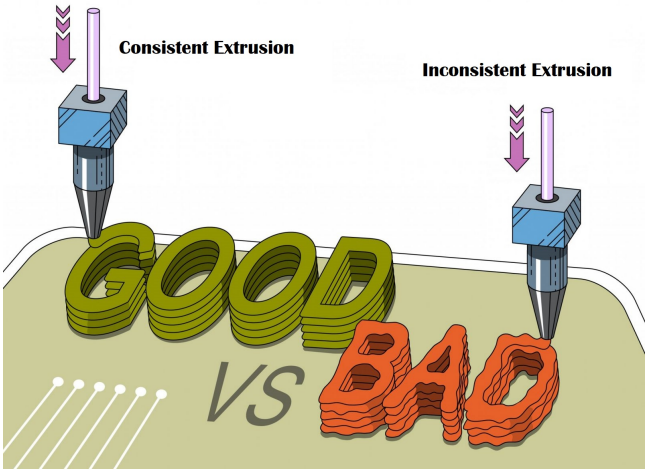


Figure 7: Original image from `http://bootsindustries.com/the-importance-of-high-quality-3d-printer-filament/`.

Extrusion is a complex process. The non-linear behaviour of the polymer and the dependencies of temperature, shear-rate, viscosity and pressure contribute to the complexity of the process that is hard to simulate and predict [3, 16, 19, 20]. A simplified schematic of the dynamics in the liquefier is shown in Figure 8.

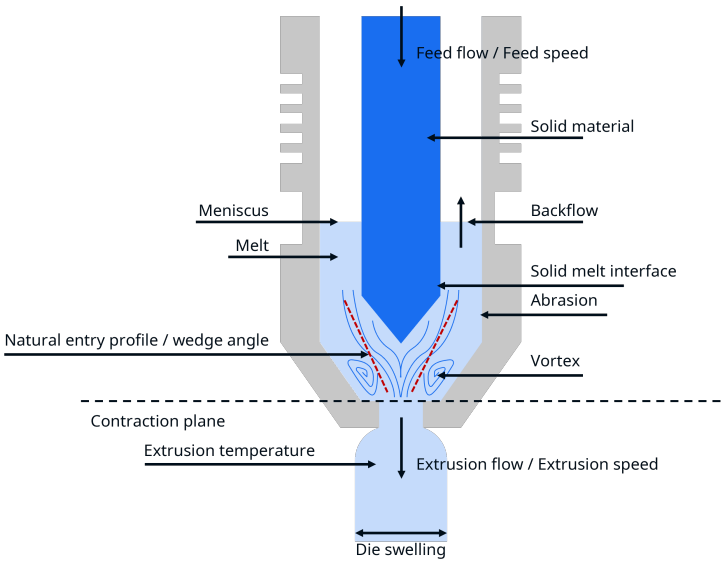


Figure 8: Simplified schematic overview of the dynamics within the liquefier. The various phenomena are explained in the text.

Filament is pushed down and melted by the nozzle. The still solid filament acts as a plunger to push the melt down, creating a pressure difference and a flow of molten polymer. The molten polymer is pushed out through the nozzle die. There is a clearance between the solid filament and the liquefier wall, which means that the molten polymer also flows upwards in the opposite direction of the solid filament. The upward movement of the melt is called backflow. The

highest point of the backflow is called the meniscus. Due to the viscosity of the polymer, the melt sticks to the wall of the liquefier and to the solid filament. This creates a velocity profile of the backflow as shown in Figure 9. The velocity profile creates vortices in the melt, disturbing the flow and adding complexity. The vortex behaviour is influenced by pressure, viscosity and temperature [12]. Additionally, there are vortices in the melt due to the viscoelasticity of the polymers [21].

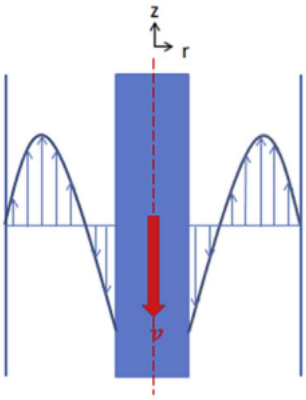


Figure 9: Velocity profile of the molten filament inside the liquefier. Image taken from Gilmer et al. [16].

The polymer is shear thinning which means that the viscosity not only depends on the temperature, but also on the shear rate of the polymer [19]. The shear rate is a measure of the velocity gradient between layers within the melt. The temperature depends on the amount of heat added, the amount of material in the nozzle, the speed at which cold filament is added and the heat transfer rates of the nozzle and of the melt. Moreover, the temperature is not uniform throughout the liquefier. The heat transfer rate of the non-Newtonian polymer is a function of shear rate and can change when the flow behaviour changes [12]. The geometry of the nozzle influences the vortices and the pressure drop [22, 23]. The melt shows elastic behaviour [12], is compressible and expands due to temperature [22]. The filament enters the liquefier at an angle and is not straight causing the filament to hit the liquefier wall and melt quicker on one side. This influences the heat flux, the velocity profile of the backflow and the pressure gradient. The filament has a small variable diameter which affects the amount of material in the liquefier, the temperature and the pressure. Another layer of complexity is added because the filament does not instantly change from a solid to a liquid state. The state-change is gradual which can cause buckling [16, 18]. Additionally, this means that there is a large gradient of temperature, shear rate and viscosity in the region between solid and molten polymer. In other words, the complex dynamics and the many dependencies of the variables create an extrusion process that is challenging to calculate and predict.

However, pressure links all of the phenomena [24]. The melt flow, temperature, viscoelasticity, compressibility and vortices all have an effect on the pressure inside the nozzle. Therefore, it is crucial to know the pressure in the extrusion process to understand its complex dynamics. Existing numerical models try to predict the pressure, but they make assumptions and simplify the actual process to get an estimate. Therefore, it is necessary to experimentally measure the pressure inside the nozzle of an FFF 3D printer.

### *2.2.2 Pressure monitoring*

Measuring and controlling pressure is challenging. The extrusion process of an FFF based 3D printer poses an extreme environment for sensors to measure pressure. For example, the sensor

has to be miniature, because the diameter of standard nozzles is around 3 mm, with an outlet die of 0.4 mm. Additionally, FFF based 3D printers operate at temperatures of at least 200 °C, so the sensor has to be heat resistant. Pressure is expected to be as high as 10 MPa. In the nozzle, the temperatures will drop and the polymer changes state. A sensor placed directly in the flow must therefore be able to withstand solidification on its measuring membrane, multiple times. The sensor must influence the flow of the molten material as little as possible to minimise the observer effect. Measuring the absolute pressure by means of piezoelectric sensors is not a viable option because they dissipate charge over time and need to be constantly re-calibrated for longer measurements [25]. Nevertheless, a few attempts at pressure monitoring have been made and compared to numerical models, which is explained below.

## 2.3 State of the art

In 2004, Bellini et al. [19] created a relatively simple mathematical model of the dynamics within the liquefier and a transfer function approach to predict flow rates and compared them to the flow rates of a 3D printer. Their measured flow rates were not the same as their predictions, however their data was in the same order of magnitude, paving the way for further research.

In 2019, Anderegg et al. [22] published an article in which they used the research of Bellini et al. to calculate the pressure drop and compared the results with experimental data using a piezoresistive pressure transducer. Because of the small dimensions of standard nozzles and the relatively large dimensions of micro piezoresistive pressure transducers, they created their own larger version of a nozzle to experiment with. Their test set-up can be seen in Figure 10. Because of their large set-up, they used a larger heating block and suffered some problems controlling a stable nozzle temperature. However, for small flow rates and a revised PID control loop they eliminated the problem and found that their pressure predictions were approximately 73% of the experimental values.

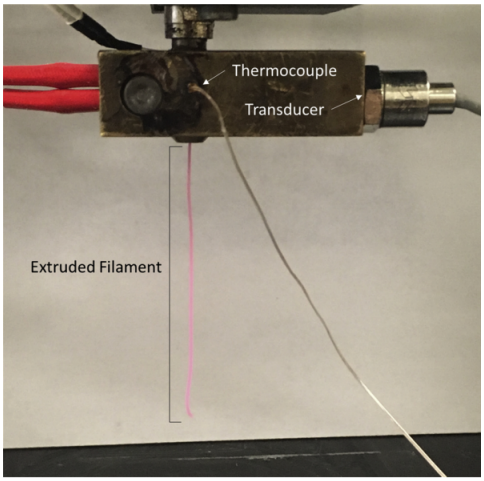


Figure 10: Experimental set-up of Anderegg et al. [22] using a piezoresistive pressure transducer and a custom-built large nozzle and heater block.

In the same year, T. J. Coogan and D. O. Kazmer [20, 26] published two articles in which they used a custom-made in-line rheometer to calculate the viscosity of materials using experimental pressure data. Their design consisted of a custom-made nozzle, a load-transfer column, a thermocouple, clamps and a load cell. A schematic is shown in Figure 11.

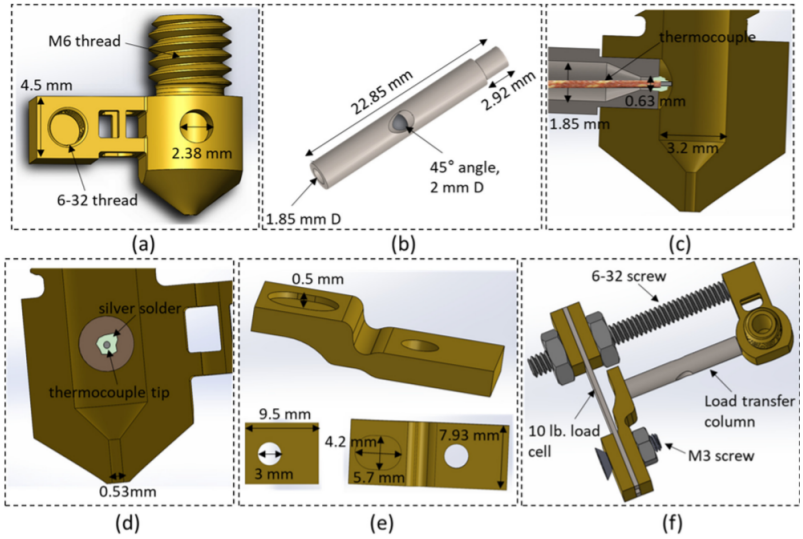


Figure 11: Schematic of the custom-made in-line rheometer by Coogan and Kazmer [20].

Their experiments "found to provide very accurate viscosity measurements" [20]. However, there were some issues with their design. It is not robust; it occupies space around the nozzle, conducts heat away from the nozzle and is prone to damage if it hits anything or if too large pressures are applied. They recorded filament leakage which meant that they had to clean the nozzle and reinstall the set-up after long prints. For future research they suggest to further minimize leakage through higher precision machining and by using the same materials in different components for better thermal expansion matching.

In 2021, Moretti et al. [27] published an article in which they compared theoretical forces on the filament with experimental data using two load cells to measure the compressive force of the filament right before it enters the liquefier as shown in Figure 12.

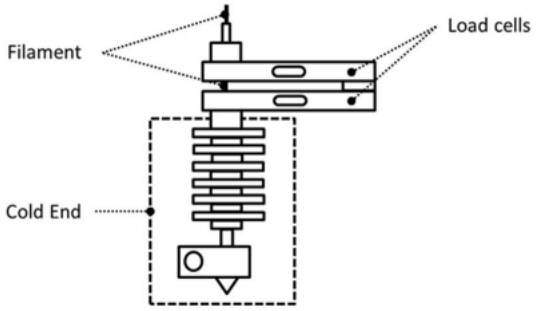


Figure 12: Schematic of the setup to measure pressure using load cells as done by Moretti et al. [27].

The theoretical compressive force was calculated by multiplying the theoretical pressure drop by the area of the filament. This way of testing is relatively easy to build and has close to no influences on the printing process. Consequently, some entrance effects are neglected and the "simulation model appears incapable of capturing the trends generally visible in the experimental data and the simulation consistently results in underestimation" [27]. Similarly, Serdeczny et al. [18] used a load cell to measure the force of the filament acting on the liquefier. However, they related it directly to the flow rather than the pressure.

In 2018, Tlegenov et al. [28] did research into nozzle clogging detection. They simulated the clogging of the nozzle by decreasing the temperature of the melt while keeping the feed-rate

constant. This was done to increase the viscosity decreasing the flow rate or even fully stop the melt from flowing. Consequently the force acting on the liquefier increases which causes different vibrations with different frequencies which they captured using a beam and an accelerometer as can be seen in Figure 13.

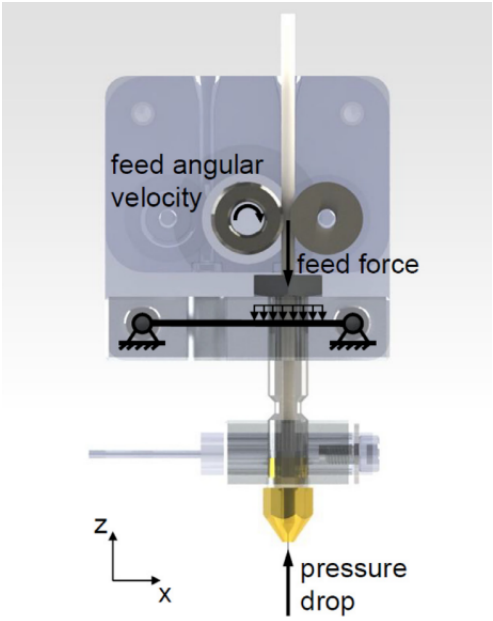


Figure 13: Schematic of the setup to measure the critical nozzle clogging force as done by Tlegenov et al.[28].

Tlegenov et al. [28] concluded that nozzle conditions can be monitored this way. Relating different eigenfrequencies to pressure values inside the nozzle has not been done. Moving the printhead induces more unwanted vibrations, so this method can only work in printers with moving printbeds and stationary nozzles.

To the author's knowledge, no other research has been conducted on monitoring the pressure drop of an FFF based 3D printer.

## 2.4 Research gap and conclusion

Currently, the extrusion is controlled by changing the temperature, the filament feed-rate and the printing speed. The printing speed is the speed at which the print head moves. As explained above, the complexities and dependencies of the variables and phenomena that happen inside the liquefier make the extrusion control unreliable. Improved extrusion control is key for the future development of fused filament fabrication. A better understanding of the dynamics of the extrusion process is needed to improve extrusion control. A reliable way of monitoring pressure is the next step in a better understanding of the dynamics of the extrusion process. However, previous research shows that it is not clear whether pressure can be monitored in the nozzle of an FFF 3D printer.

The scope of this thesis is to provide experimental pressure data for a better understanding of the complex flow of melt during extrusion. A novel way of monitoring the pressure inside the nozzle of fused filament fabrication 3D printers will be presented. The results from this study are repeatable and give insights on the key aspects that influence the dynamics within the nozzle of an FFF 3D printer. This project enables new possibilities in terms of extrusion process monitoring and the development of new extrusion control strategies.

# Paper


## Abstract

**Fused filament fabrication (FFF) is the most used additive manufacturing technique that uses a heated nozzle to melt a polymer and a feeder to extrude it on a buildplate. The dependencies of temperature, shear-rate, viscosity and pressure of the melt create complex dynamics within the nozzle, which causes inconsistent extrusion. To improve extrusion control, a better understanding of the dynamics within the nozzle is required. The greatest knowledge gap comes from a lack of experimental data on the pressure inside the nozzle, due to the challenging environment for sensors. This study presents a novel way of monitoring the pressure inside the nozzle of an FFF 3D printer. A pin that is in direct contact with the melt transfers the force applied by the melt through a hole in the nozzle to an externally mounted load cell. The set-up has proven to provide reliable, repeatable pressure data in steady-state, static extrusion. The experimental data on different nozzle geometries and materials, with different flows and temperatures, has been compared to theoretical pressure calculations to identify non-linearities that influence the pressure such as entrance effects, temperature non-uniformity and viscoelastic behaviour of the melt. The proposed design can be used to gain more knowledge on the extrusion process to further develop extrusion control.**


## Introduction

Additive manufacturing (AM), commonly referred to as 3D printing, is becoming an increasingly popular technology [1]. AM techniques add material layer-by-layer to form three dimensional objects. This opens up the possibility to construct complex geometries because it is not limited by the accessibility of subtractive tools [2]. Fused filament fabrication (FFF) is the most used AM technique [2]. It uses a feeder and a heated nozzle to melt a polymer and extrude it on a build plate. The still solid polymer, called filament, acts as a plunger to push the melt through the outlet of the nozzle. The outlet is referred to as nozzle die. The nozzle is mounted to a printing head which can be moved in a horizontal plane. The melt solidifies and forms a single layer of solid plastic. The build plate is lowered and a second layer is extruded on top of the first layer. Figure 14 illustrates the working principle. Development of printers and materials over the past decades has increased print quality. However, nowadays FFF is mainly used for rapid prototyping [14]. The technology is not reliable enough to repeatedly create end-of-use parts. The dependencies of temperature, shear-rate, viscosity and pressure of the melt create complex dynamics within the nozzle.

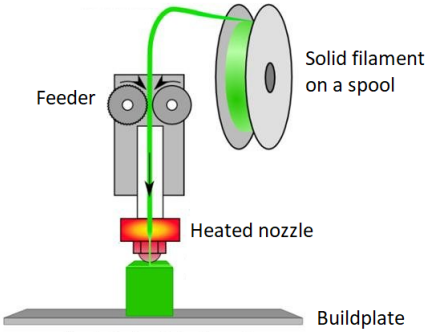


Figure 14: Image from [29].

This causes inconsistent extrusion. A better understanding of the extrusion process is required to improve extrusion and increase the print quality of FFF. The two most important parameters that influence the extrusion process are melt temperature and melt pressure [24]. They are the key variables that determine how well the polymer is extruded. Temperature is relatively easy to measure and control. Monitoring and controlling pressure is challenging. The small dimensions of the nozzle and the high temperatures of the melt pose a challenging environment and it rules out the use of readily available pressure sensors. Currently, there is no reliable method to measure the pressure inside the nozzle of an FFF based 3D printer. Consequently, there

is a lack of experimental pressure data that can verify nozzle pressure simulations. This study presents a novel way of measuring the pressure inside the nozzle of an FFF based 3D printer. The set-up designed in this study is compared to existing pressure monitoring techniques and related to theoretically calculated pressure values to assess the flaws of the experiment and theory. This study will provide repeatable pressure measurements at multiple flows and temperatures, with a range of nozzles and materials, that unprecedentedly capture non-linearities in the extrusion process. This knowledge will help indicate important aspects during the extrusion process, such as entrance effects, temperature non-uniformity and elastic effects and poses a basis for the improvement of extrusion control in FFF based 3D printers.

## Experiment design

In order to monitor the pressure inside the nozzle of an FFF based 3D printer, an experimental set-up has been developed. It was designed to work on an Ultimaker nozzle, which are typically made of brass. Their dimensions are in the range of a few millimeters, see Figure 15.

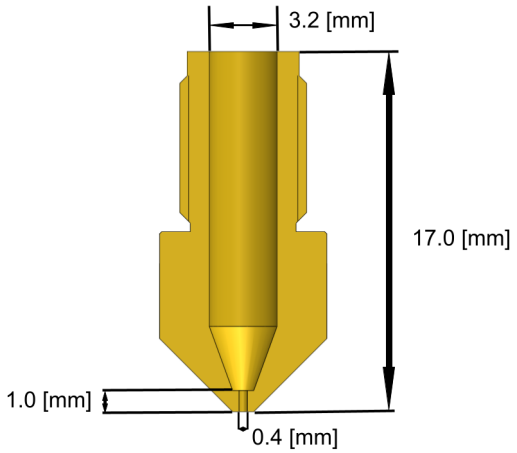


Figure 15: A typical nozzle used in an Ultimaker 3D printer.

Therefore, a pressure sensor that would directly measure the pressure in the flow has to be small. It has to be temperature resistant because nozzle temperatures range from 200 °C to 280 °C during printing, depending on the material used. The sensor must be able to withstand the pressures in the nozzle, which are estimated to reach up to 94 bar, see Appendix A.1 for an explanation of the estimation. In between extrusion, the polymer cools down and transitions to solid state. The measuring membrane of the sensor must be able to withstand this state-change without suffering damage. Additionally, the sensor must be able to measure absolute pressure for long periods of time, eliminating piezoelectric sensors [25]. The absence of readily available pressure transducers that meet all of the requirements has led to a new pressure monitoring design.

*Pressure monitoring concept*

The chosen concept makes use of a pin that is in direct contact with the melt. Through a hole in the nozzle, the pin transfers the applied force of the melt to an external sensor, see Figure 16.

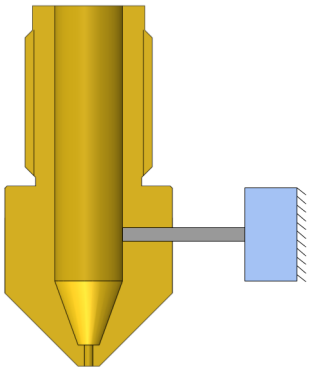

Figure 16: Pressure monitoring concept. A pin (gray) transfers the melt pressure to an external sensor (blue).

By placing the sensor outside the liquefier, the sensor is not directly in contact with the melt. Therefore, the sensor is not susceptible to high temperatures and to the polymer changing state. Moreover, the dimensions of the sensor can be higher. This simplifies the search for a suitable sensor drastically. However, it induces other problems such as leakage. Appendix A.1 describes in more detail how this concept was selected.

*Pressure monitoring, elaborate design*

To realise this design, a hole was made in the side of a standard Ultimaker nozzle. The hole had to have enough clearance for the pin to move freely, whilst being tight enough to prevent leakage. Additionally, the pin had to be

machined with a smooth surface. A sliding fit H7/g6 was chosen, which is used for fits with very small clearances for accurate guiding of shafts. During extrusion, nozzle temperatures rise up to at least 200 °C. Due to thermal expansion, both the pin and the hole expand. To avoid a mismatch in thermal expansion, the pin was manufactured from the same material as the nozzle, brass CuZn39Pb3. The inner wall of the nozzle is circular, whereas the frontal surface area of the pin is flat. This creates a ledge inside the nozzle which will influence the flow. To reduce this effect, the dimensions of the hole and the pin should be as small as possible. A smaller hole and pin diameter have more advantages. The heat that conducts away from the nozzle is lower, and the force that is transferred is lower with a smaller frontal surface area, according to

$$P = \frac{F}{A}, \tag{1}$$

where $P$ is pressure, $F$ is force and $A$ is the area at which the force applies. When the force is smaller, a smaller sensor can be used without losing sensitivity, which is favourable because of the limited space around the nozzle. However, the manufacturability of the pin decreases with smaller dimensions, increasing the cost. A trade-off was chosen between the advantages of a smaller pin and the costs related to manufacturing it, resulting in a pin diameter of 1 mm. The end of the pin touching the load cell was rounded to decrease heat conduction to the load cell. To prevent locking and buckling of the pin, a brass guiding tube was press-fit into the nozzle to serve as guidance for the pin. The final modified nozzle and the pin are shown in Figure 17.

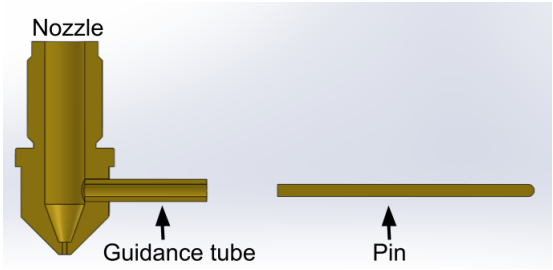


Figure 17: Custom-made equipment for pressure monitoring inside an Ultimaker nozzle.

A 0.78kg micro load cell, Wheatstone bridge sensor was selected. This sensor is relatively robust, enables multiple mounting options, is easy to use and cost efficient. With an expected maximum pressure of 94 bar, and a pin diameter of 1 mm, the expected maximum force is 7.4 N according to Equation 1. This lies within the range of the load cell. Specifications on the load cell can be found in Appendix A.2.

*Complete assembly*

The experiment was conducted as a proof-of-concept in a static environment; extrusion in open air with no printhead movement. Nevertheless, the pressure monitoring set-up was designed to fit in an Ultimaker printhead whilst printing, for further research. This is described in more detail in Appendix D.3. In order to capture more details of the extrusion process, a larger experiment design has been assembled. Figure 18 shows a schematic of the test set-up, Figures 19 and 20 show images of the test set-up. In the experiment an MS16HS7P4070 stepper motor feeds the filament into the liquefier. From now on this will be referred to as 'feeder' and its input velocity is controllable. The velocity of the feeder determines the filament throughput, which is expressed as displaced filament volume per unit of time, with unit $mm^3/s$. However, the feeder can slip, for example due to large friction forces. To account for this phenomena, an ERN 1023 rotary encoder is installed to measure the real filament flow-rate. A Bowden tube guides the filament into the liquefier. Bowden tubes have a low coefficient of friction and are used in 3D printers to guide the filament. The filament is pushed through the cold end into the nozzle, where it is melted. The force by which the feeder pushes the filament is captured by a 35kg Wheatstone bridge load cell. The assembly of the nozzle is the same as in Ultimaker printers; the nozzle is mounted to the cold end and heated through a heater block, which serves as a thermal inertia to reduce peak temperature fluctuations. The temperature of the heater block is controlled through a 25 Watt heater cartridge and a platinum 100 ohm (PT100) temperature sensor, which are PID calibrated with values kp is 0.04, ki is 20.0 and kd is 10.0.

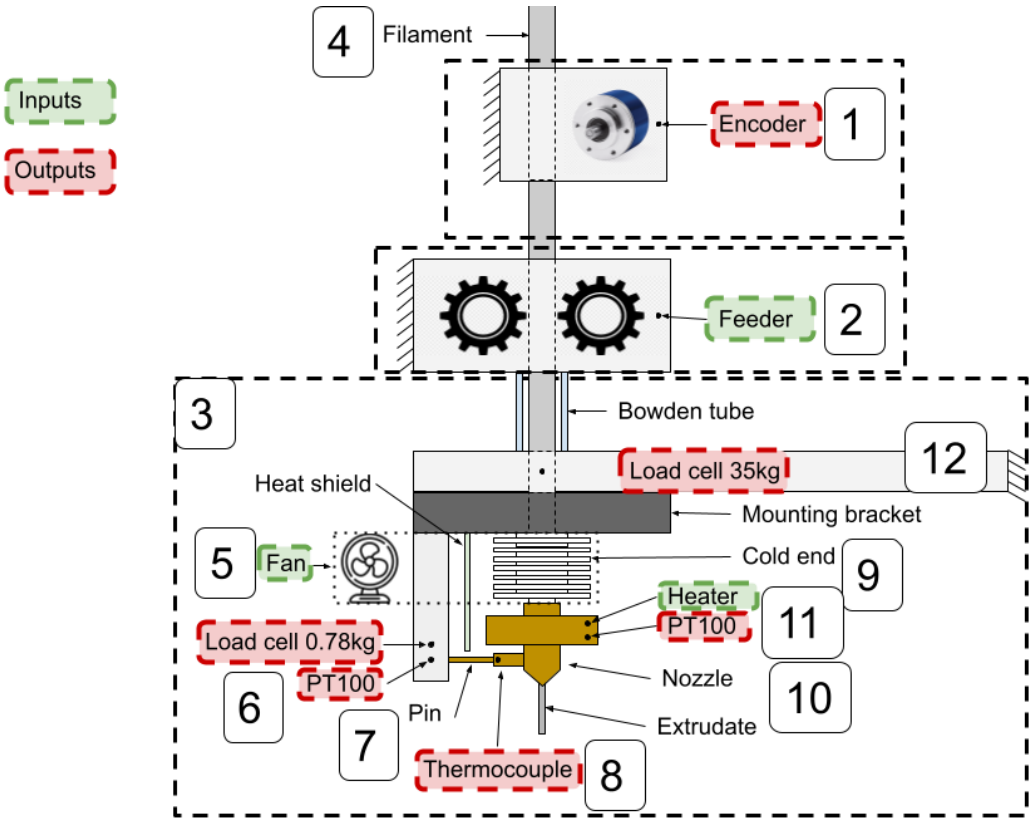


Figure 18: Schematic of the complete test set-up. The items highlighted in green are user inputs and can be controlled. The items highlighted in red are measured outputs which are logged at 1 kHz using Beckhoff data acquisition modules connected to real-time TwinCAT software using EtherCAT. The data from those sensors are logged on the same timestamp. The numbers 1 to 12 are for comparison with Figures 19 and 20.

A Conatex TM12K02GG2 thermocouple is glued to the end of the guidance tube with Permasol Sauereisen No. 31 A/B adhesive. This is a temperature resistant glue that serves as a good heat conductor. The pin that is in contact with the melt transfers the force to a 0.78kg Wheatstone bridge load cell, as described in subsection *Pressure monitoring, elaborate design*. The temperature of the load cell is monitored with a PT100. A droplet of Griffon unilube is applied between the pin and the load cell for lubrication. A heat shield made of aluminum foil is installed to prevent the 0.78kg load cell from overheating. A Sunon 40x40x10 axial fan is used to cool the cold end and the load cell. Both load cells, the fan, the heat shield and the cold end were attached to a custom-made aluminum mounting bracket. Logging of the sensors was done at 1 kHz using Beckhoff data acquisition modules connected to real-time TwinCAT software using EtherCAT. The data points are logged on the same timestamp. Appendix A.3 describes the calibration process of each sensor. A readily available static extrusion device has been used as a base for this assembly. An elaborate explanation of how the set-up was assembled can be found in Appendix A.4.

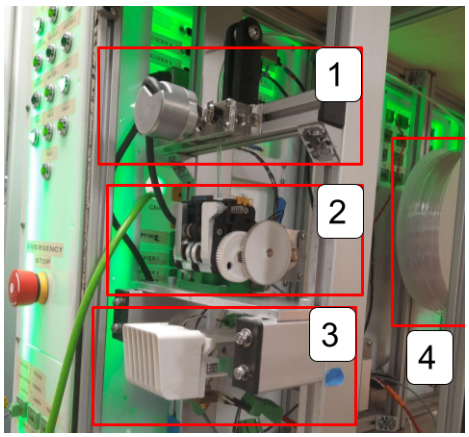


Figure 19: The complete test set-up. 1: Rotary encoder. 2: Feeder. 3: Modified nozzle assembly. 4: Filament.

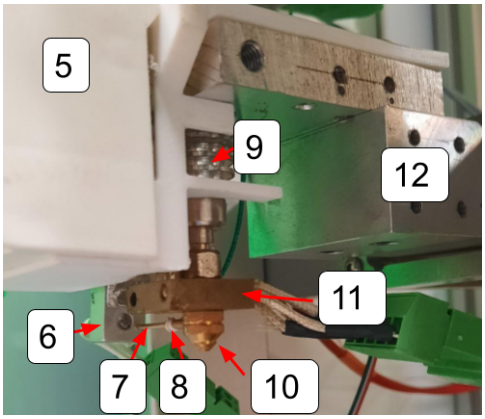


Figure 20: A closeup of the set-up around the modified nozzle. 5: Fan. 6: 0.78kg load cell and PT100. 7: Pin. 8: Thermocouple. 9: Cold end. 10: Nozzle. 11: Heater and PT100. 12: 35kg load cell.

## Methods

*Materials*

The primary experiments were conducted using a polymer called Ultimaker transparent polylactic acid (PLA). It has a melting temperature of $T_m$ is 151.8 °C. The polymer is wound on a spool as a filament with a diameter of $D_f$ is 2.85 ± 0.10 mm. Print temperatures ($T_p$) range from 195 °C to 220 °C. Further experiments have been conducted on Ultimaker transparent polycarbonate (PC), Ultimaker transparent glycol-modified polyethylene terephthalate (PETG) and black DSM Novamid ID1030 polyamide 6/66 (Nylon). Their thermal properties can be found in Table 1.

| Material | $T_m$ (°C) | $T_p$ (°C) | D (mm) |
|---|---|---|---|
| PLA | 151.8 | 195-215 | 2.85±0.10 |
| PC | 152.5* | 260-280 | 2.85±0.05 |
| PETG | 225.0* | 230-245 | 2.85±0.05 |
| Nylon | 200 | 250-275 | 2.85±0.05 |

Table 1: Thermal properties of the materials used. $T_m$ is the melt temperature, $T_p$ is the print temperature range and D is the diameter of the filament. The data is acquired from technical datasheets [30–33]. *Amorphous material, so the melting point is a transition range. The number described here is the mean of the melting range.

All the materials are non-Newtonian, viscoelastic, pseudoplastic polymers. This means that their resistance to flow (viscosity) is not linearly dependent on its rate of deformation (shear rate). Moreover, pseudoplastic fluids are shear-thinning, which means their viscosity is lower at higher shear rates. Additionally, their viscosity is higher at lower temperatures. A viscosity-shear rate curve of PLA at a temperature of 200 °C is shown in Figure 21. This data was provided by a research partner of Ultimaker.

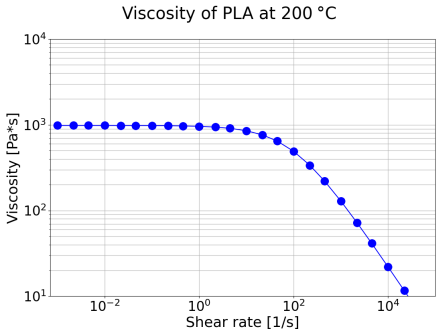


Figure 21: Viscosity vs shear rate for PLA at 200 °C. Note that the axes are on a logarithmic scale.

The viscosity curve for multiple temperatures is obtained by combining the Cross equation with the Arrhenius equation. The Cross equation states

$$\eta(T,\dot{\gamma}) = \frac{\eta_0(T)}{1 + (\lambda(T) * \dot{\gamma})^a} \tag{2}$$

where $\eta(T,\dot{\gamma})$ is the viscosity, $T$ is the temperature, $\eta_0(T)$ is the zero shear rate viscosity, $\lambda(T)$ is the relaxation time and $a$ is the shear-thinning constant. The zero shear rate viscosity $\eta_0$ and the relaxation time $\lambda$ are temperature dependent. Their values are calculated as

$$\eta_0(T) = a_T * \eta_0(T_{\text{ref}}) \tag{3a}$$

$$\lambda(T) = a_T * \lambda(T_{\text{ref}}) \tag{3b}$$

where $a_{\text{T}}$ is the Arrhenius equation and $T_{\text{ref}}$ is the reference temperature. The Arrhenius equation compensates for the difference in temperature according to

$$a_T = \exp\left(\frac{E_a}{R} * \left(\frac{1}{T} - \frac{1}{T_{\text{ref}}}\right)\right) \tag{4}$$

where $E_a$ is the Arrhenius activation energy and $R$ is the gas constant. The Cross-Arrhenius equations have been used to calculate the viscosity curves for PLA at different temperatures, shown in Figure 22.

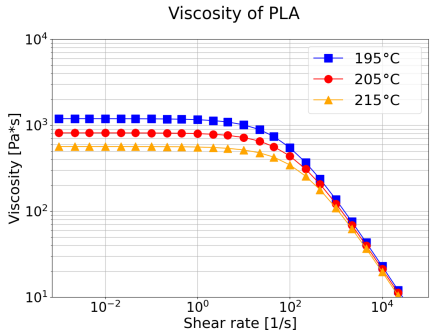


Figure 22: Viscosity curve for PLA at three different temperatures.

The values of the parameters that are used to plot this graph were obtained by an external research partner of Ultimaker. The values are listed in Table 2. The viscosity curves of the other materials can be found in Appendix E.1.

| | |
|---|---|
| $E_a$ $(J/mol)$ | 70,700 |
| $R$ $(J/(mol * K))$ | 8.314 |
| $T_{\text{ref}}$ $(K)$ | 473.15 |
| $\eta_0(T_{\text{ref}})$ $(Pa * s)$ | 982 |
| $\lambda(T_{ref})$ $(s)$ | 0.01 |
| $a$ (-) | 0.82 |

Table 2: Constants used to compute the viscosity curves for PLA. These are values from external research done by an Ultimaker partner.

*Nozzles*

Figure 23 illustrates the cross section of an Ultimaker nozzle. Depending on its type, a nozzle can have a plateau with diameter $D_p$ on the inside, above the nozzle die.

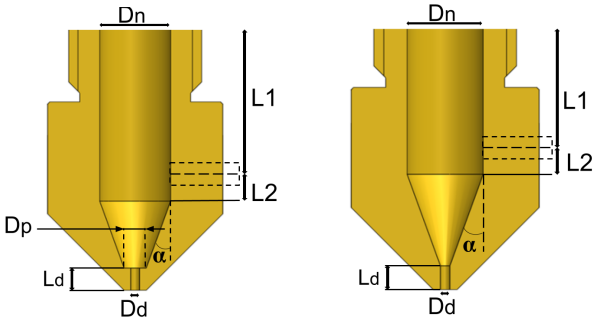


(a) Nozzle with a plateau above the die.

(b) Nozzle without a plateau.

Figure 23: This illustration shows the difference between nozzles. They differ in dimensions and they can have a plateau ($D_p$) or not.

Furthermore, nozzles differ in dimensions. Three different types of nozzles have been tested. Their dimensions can be found in Table 3. Important differences are that nozzle types 1 and 2 have a plateau, whereas nozzle type 3 does not; the plateau diameter is the same as the nozzle die diameter. Additionally, nozzle types 2 and 3 have a die diameter of 0.4 mm, whereas type 1 has a die diameter of 0.8 mm. The center point of the pin is always 1.1 mm above the tapered part of the nozzle ($L_2$).

| | **Nozzle type** | | |
|---|---|---|---|
| **Dimension** | **1** | **2** | **3** |
| $D_n$ [mm] | 3.2 | 3.2 | 3.2 |
| $L_1$ [mm] | 11.96 | 11.88 | 11.05 |
| $L_2$ [mm] | 1.1 | 1.1 | 1.1 |
| $\alpha$ [°] | 20 | 20 | 20 |
| $D_p$ [mm] | 1.5 | 1.0 | 0.4 |
| $L_d$ [mm] | 1.6 | 1.0 | 1.0 |
| $D_d$ [mm] | 0.8 | 0.4 | 0.4 |

Table 3: Dimensions of the three types of nozzles that have been tested. See Figure 23 for a clear image of the dimensions.

*Microscope*

Prior to testing, both the modified nozzle and the pin were imaged using a Leica DVM6 Digital Microscope. The diameters of the pin, the guidance tube and the nozzle die were measured using the microscope. Additionally, the equipment was checked for damage and inconsistencies. For example, the alignment of the guidance tube with the inner wall of the nozzle was checked, see Figure 24. More details about the microscope can be found in Appendix C.2.

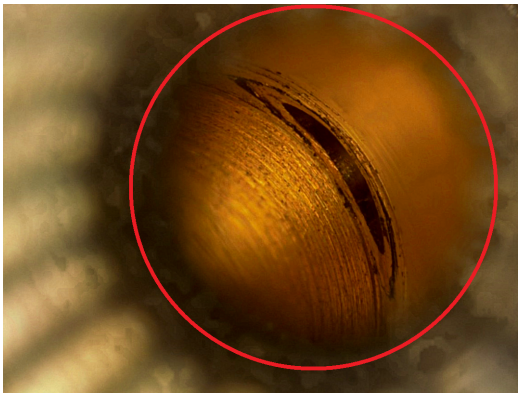

Figure 24: Example image of the alignment of the guidance tube that was press-fit into the nozzle.

*Experiment*

At the start of an experiment, the filament was fed to the liquefier with a constant feed-rate at a constant print temperature, which is different for each material. This action of purging the nozzle was performed for thirty minutes prior to each experiment. After purging, the system was idled and checked for failures. The data was checked for anomalies. The nozzle was reheated to a constant initial temperature, 195 °C for PLA. The feed-rate was set to the initial feed-rate, for example 1 $mm^3/s$. This constant extrusion was done for ten minutes and is referred to as a test. After every test, the data was stored as a single hierarchical data format 5 (hdf5) file. The feed-rate was increased and another ten minutes of constant extrusion was executed. In total, four feed-rates were tested. A ten second pause separates the tests from each other. After all the feed-rates were tested, the temperature was increased and the feed-rate was reset to the initial value again. The same four feed-rates were tested on a higher temperature. Finally, the temperature was increased again and another sequence of four feed-rates was tested. This cycle of 12 tests was repeated twice. Subsequently, in total a single experiment consists of 36 tests. Every test is a ten minute extrusion with a constant feed-rate and a constant temperature. In order to automate this process, Python was used to set the heater temperature and to program the control of the feeder. The temperature was kept constant with a separate PID control loop.

*Data analysis*

The terms extrusion force/pressure and nozzle force/pressure are used to discriminate between the two measured forces, as shown in Figure 25. The extrusion force is measured by a 35kg load cell and converted to pressure using the area of the solid filament. The nozzle force is transferred by a pin and measured by a 0.78kg load cell. The force is converted to pressure using the frontal area of the pin.

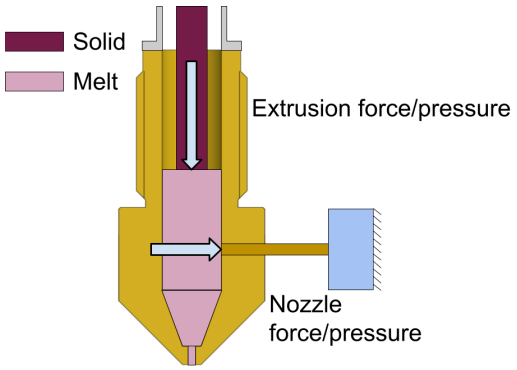


Figure 25: The extrusion force is measured by a 35kg load cell and converted to pressure using the area of the solid filament. The nozzle force is transferred by a pin and measured by a 0.78kg load cell. The force is converted to pressure using the frontal area of the pin.

For each ten minute test, with a constant temperature and constant feed-rate, the extrusion pressure and nozzle pressure were calculated using Equation 1 with their respective area. Figure 26 shows an example of a pressure-time graph of both pressures for a single test. Note that the pressure is calculated in Pa and converted to bar before plotted. It takes time for the system to reach steady-state, which generally happens after 150 s. The average value is calculated between that point and the end of the test, indicated by red dots.

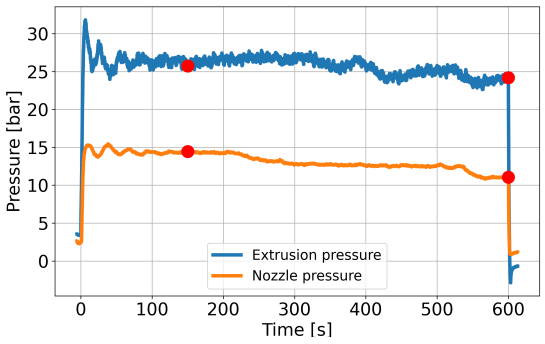


Figure 26: The extrusion pressure (blue) and nozzle pressure (orange) plotted against time for a single ten minute test. This example is with a type 2 nozzle, a feed-rate of 1 $mm^3/s$ and a temperature of 205 °C. The average pressure value is taken after reaching steady-state, between the two red dots.

Multiple feed-rate and temperature combinations were tested, averaged and plotted in a pressure-flow graph. Note that flow is not the same as feed-rate. Feed-rate is the set point of the volumetric flow of filament. Flow is the actual volumetric flow accounting for the slip of the feeder. Each test was repeated three

times. The error of the force was propagated with the error of the area to get the error of the pressure, according to

$$\sigma_P = P * \sqrt{(\frac{\sigma_F}{F})^2 + (\frac{\sigma_A}{A})^2}, \tag{5}$$

where $P$ is the pressure, $\sigma_P$ is the error of the pressure, $F$ is the average force, $\sigma_F$ is the error of the force, $A$ is the area and $\sigma_A$ is the error of the area. Calculation of $\sigma_F$, $\sigma_A$ and the error of the flow is described in Appendix C.1.

*Theoretical calculations*

The experimental data was compared to theoretically calculated pressure values. The theoretical pressure data is based on a relatively simple method for calculating the pressure drop throughout the nozzle, proposed by Bellini et al. [19]. They combined the law of conservation of mass and the law of conservation of momentum on a flow component throughout three different sections of the nozzle. They then applied the power law model of pseudoplastic melts to define a set of equations to calculate the pressure drop through each section. This study uses similar theory, but divides the nozzle into four sections, shown in Figure 27.

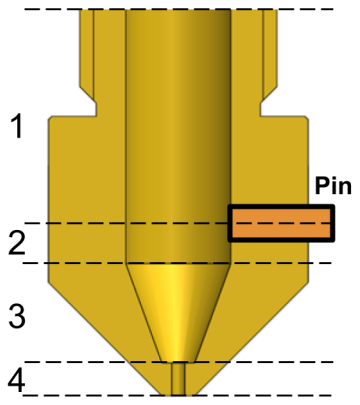


Figure 27: A nozzle divided into four sections. Section 1 ranges from the top of the nozzle to the center of the pressure monitoring pin. Section 2 ranges from the center of the pin to the start of the conical shape within the nozzle. Section 3 is the conically shaped part of the nozzle and section 4 is the nozzle die. The rectangle on the right illustrates the position of the pin.

Pseudoplastic melts exhibit shear-thinning behaviour; their viscosity decreases when their shear rate increases (see Figure 21). The power law is a method to describe such behaviour. It is a good compromise between its simplicity and its ability to fit the rheological data. The power law of pseudoplastic melts relates the shear stress and the shear rate of the fluid through its material properties:

$$\tau = \left(\frac{\dot{\gamma}}{\phi}\right)^{\frac{1}{m}} \tag{6}$$

where $\tau$ is the shear stress, $\dot{\gamma}$ is shear rate, $\phi$ is the fluidity of the material and $m$ is the flow exponent of the material, see Appendix B.1. The pressure drop equations through each section follow:

$$\Delta P_1 = 2 * L_1 * \left(\frac{v}{\phi}\right)^{\frac{1}{m}} * \left(\frac{m+3}{\left(\frac{D_n}{2}\right)^{m+1}}\right)^{\frac{1}{m}} \tag{7a}$$

$$\Delta P_2 = 2 * L_2 * \left(\frac{v}{\phi}\right)^{\frac{1}{m}} * \left(\frac{m+3}{\left(\frac{D_n}{2}\right)^{m+1}}\right)^{\frac{1}{m}} \tag{7b}$$

$$\Delta P_3 = \left(\frac{2*m}{3*\tan\alpha}\right) * \left(\frac{1}{D_p^{\frac{3}{m}}} - \frac{1}{D_n^{\frac{3}{m}}}\right) * \left(\left(\frac{D_n}{2}\right)^2 * (m+3) * 2^{m+3}\right)^{\frac{1}{m}} * \left(\frac{v}{\phi}\right)^{\frac{1}{m}} \tag{7c}$$

$$\Delta P_4 = 2 * L_d * \left(\frac{v}{\phi}\right)^{\frac{1}{m}} * \left(\frac{(m+3) * \left(\frac{D_n}{2}\right)^2}{\left(\frac{D_d}{2}\right)^{m+3}}\right)^{\frac{1}{m}} \tag{7d}$$

where $\Delta P_i$ is the pressure drop over a section $i$ and $v$ is the speed at which the filament enters the nozzle. The sections and variables $L_1$, $D_n$, $L_2$, $\alpha$, $D_p$, $L_d$ and $D_d$ are illustrated in Figure 23. Equation 7c, which describes the pressure drop over the conical part of the nozzle, has been corrected. In the paper of Bellini et al. [19], the term $\left(\frac{v}{\phi}\right)^{\frac{1}{m}}$ is missing, which has been added in this study. Appendix B.2 explains this in more detail.

## Results & Discussion

The first goal of this study is to evaluate if it is possible to measure the pressure inside the nozzle of an FFF 3D printer. Because PLA

is the most used material in FFF 3D printing, the focus of the pressure monitoring research was on PLA. Therefore, the majority of the results come from the experiments with PLA. Figures 28 and 29 show an example of a pressure-flow graph for the extrusion pressure and nozzle pressure, respectively. This example is from an experiment with a type 1 nozzle.

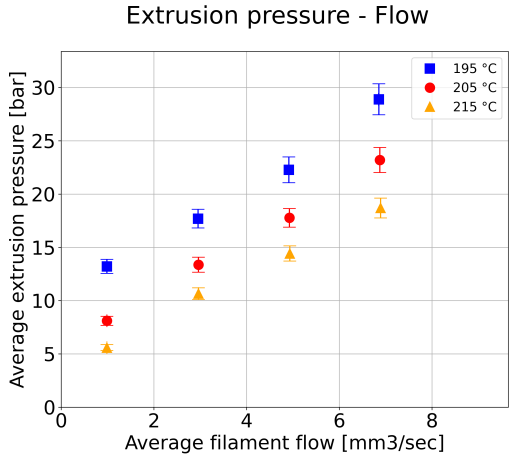


Figure 28: Extrusion pressure versus flow for four different feed-rates and three different temperatures with a type 1 nozzle.

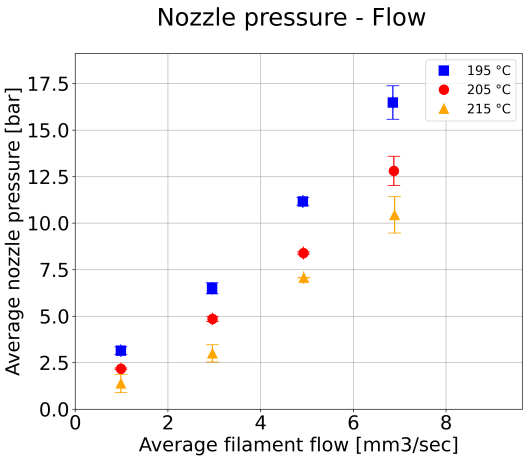


Figure 29: Nozzle pressure versus flow for four different feed-rates and three different temperatures with a type 1 nozzle.

These graphs clearly show that the nozzle pressure increases as the volumetric flow rate (flow) increases, which is expected. For the same flow, an increase in temperature results in a decrease in nozzle pressure. This is mainly due to the viscosity of the polymer, which decreases at increasing temperatures. In a single test, the standard deviation of the extrusion force is generally between 1% and 5%, with an average of 3%. The standard deviation of the nozzle force is generally between 0.5% and 3%, with an average of 2%. This is a measure of the deviation of the forces within a single test; constant temperature and constant feed rate. The standard deviation of repeated tests is within the same range. The average standard deviation is 4% and 2%, for the extrusion force and nozzle force respectively. Furthermore, a part to part analysis showed that the error between two identical nozzles is around 4% for both the extrusion force and the nozzle force. This indicates that the tests are repeatable.

During the experiments, polymer was recorded leaking out of the guidance tube. This could have an effect on the nozzle force measurements, illustrated in Figure 30.

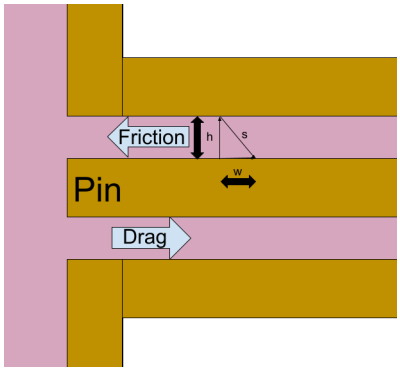


Figure 30: Melt in between the pin and guidance tube can have an effect on the measurements. The melt can drag the pin out increasing the measurements, or it can cause friction which decreases the measurements.

The flow of melt leaking out can drag the pin outwards resulting in higher force measurements. However, the flow of melt was low. Figure 31 shows the leakage recorded after 6.5 hours of extrusion. An approximation of the leakage based on this image results in a volumetric leakage of approximately 1 $mm^3$. As a comparison, when extruding at an average flow of 4 $mm^3/s$ for 6.5 hours, a total volume of 93,600 $mm^3$ is extruded. The flow of melt leaking out is 0.001%. Therefore, the drag force is considered negligible.

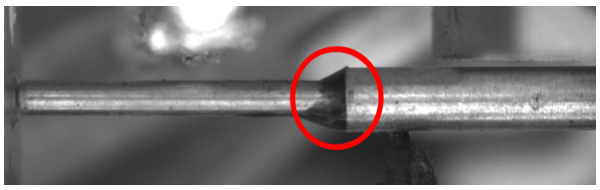

Figure 31: Leakage between guidance tube and pin. This image was taken after 6.5 hours of extrusion.

The friction force is approximated using the following equations:

$$F_{fr} = \sigma * A_L \tag{8a}$$

$$\sigma = G' * \epsilon \tag{8b}$$

$$\epsilon = \frac{w}{h} \tag{8c}$$

where $F_{fr}$ is the friction force, $\sigma$ is the stress within the leaking polymer, $A_L$ is the lateral area of the pin inside the tube, $G'$ is the elastic modulus of the leaking polymer, $\epsilon$ is the strain of the leaking polymer, $w$ is the horizontal displacement of the pin and $h$ is the distance between the pin and the guidance tube. The horizontal displacement $w$ depends on the pressure and is taken from the load cell calibrations values. Both $h$ and $A_L$ were calculated using the diameters of the pin and guidance tube obtained by the microscope, see Chapter *Methods: Microscope*. Thermal expansion of the equipment was accounted for using the temperature data from the thermocouple, see Chapter *Experiment design: Complete assembly*. The friction force is different for each nozzle, flow speed and temperature. Throughout the experiments with PLA it is estimated to lie between 0% and 5% of the measured nozzle force. For most data points, the friction is approximately 2%. Its contribution to the measurements is small and variable. Therefore, its influence is neglected. A more elaborate explanation of the approximation of the friction can be found in Appendix C.3.

At this point the experiment has proven to be able to repeatedly measure the pressure inside the nozzle of an FFF 3D printer. In order to make sense of the nozzle force data, it has been compared to the extrusion force data.

*Comparison of forces*

When comparing Figure 28 to Figure 29, the trend of the data points look similar. This is confirmed by Figure 32, which shows the average extrusion force plotted versus the average nozzle force. This graph is from the same experiment as Figures 28 and 29.

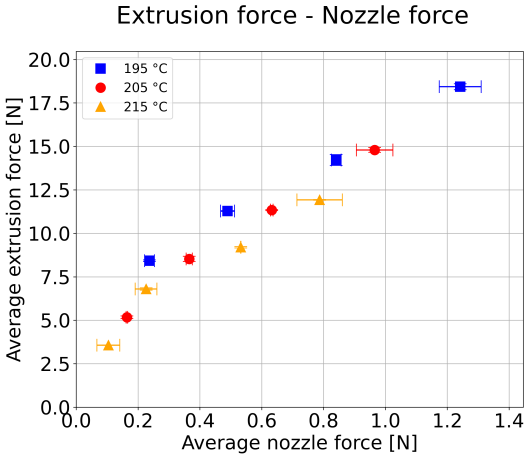


Figure 32: Average extrusion force plotted against average nozzle force. This graph shows that the nozzle force increases when the extrusion force increases.

Note that these data points are forces rather than pressures. That way the errors in the graph are purely force related and not affected by the errors of the area of the filament or pin. The trend of this graph shows that the nozzle force increases when the extrusion force increases. Moreover, when examining both forces during a single test more closely, they show similar behaviour in terms of fluctuation. This is illustrated in Figure 33.

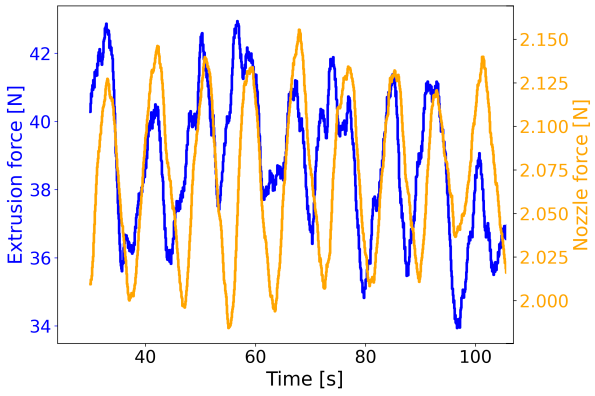


Figure 33: Extrusion force and nozzle force during a single test.

Figures 32 and 33 confirm that the trend of the measured nozzle pressure behaves similarly to the trend of the measured extrusion pressure, in real time and as a function of temperature and flow. However, it does not confirm the absolute values of the nozzle pressure data.

*Comparison to theory*

To better evaluate the absolute values of the extrusion pressure and the nozzle pressure, they have been compared to theoretical pressure calculations. The power law (Equation 6) was used to approach the non-Newtonian slope of the viscosity curves of PLA to determine the material properties $m$ and $\phi$, see appendix E.1. The speed of the filament $v$ was calculated by dividing the volumetric flow over the area of the filament. The speed, geometrical values of the nozzle and the material properties were inserted into the pressure drop equations (Equation 7). This was done for multiple flows and temperatures. The sum of the results of the pressure drop Equations 7b, 7c and 7d, which correspond to nozzle sections 2, 3 and 4, relates to the pressure drop from the center of the pin to the bottom of the nozzle. Those values were plotted in the nozzle pressure graph of a type 3 nozzle, shown in Figure 34.

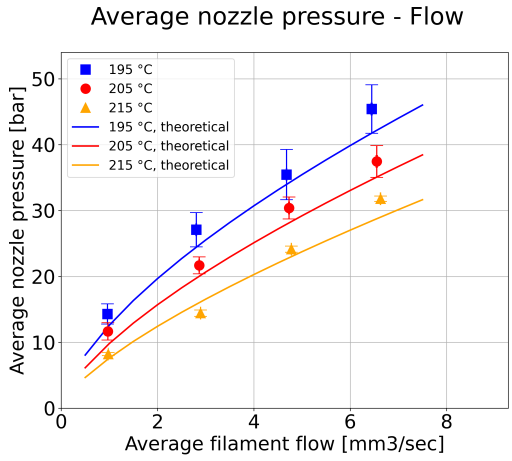


Figure 34: Nozzle pressure in a type 3 nozzle.

There is an excellent match between the theory and the experimental nozzle pressure data. As a comparison, the theory has been plotted versus the experimental extrusion pressure. The sum of the results of the pressure drop equations over all sections relates to the total pressure drop and was plotted in the extrusion pressure graph, shown in Figure 35.

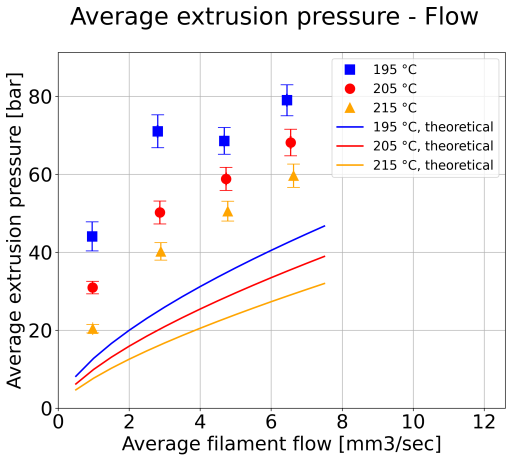


Figure 35: Extrusion pressure in a type 3 nozzle.

There is a mismatch between the experimental data and the theory. The measured extrusion pressure data is higher than the theory at any flow and temperature. The theoretical pressure drop over the first nozzle section is low compared to sections 3 and 4. That is why the theoretical pressure difference between Figures 34 and 35 is barely visible. However, the experimental nozzle pressure data is much lower than the experimental extrusion pressure data, and has a better match. This could be because not all of the extrusion force measured is due to the pressure, but also due to friction.

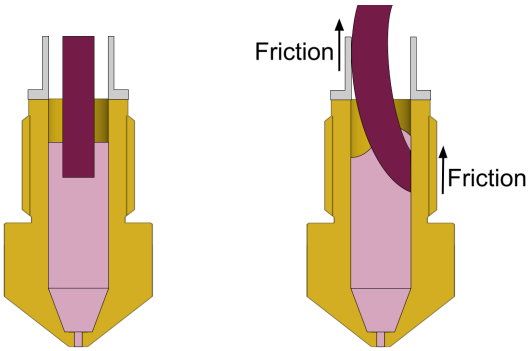


(a) The theory assumes perfectly straight filament entering in the center of the nozzle.

(b) In the experiment, the filament causes more friction due to contact with the walls.

Figure 36

For example, the filament that enters the nozzle has a curved shape because it is wound on a spool. This shape causes extra friction in the cold end and at the wall in the nozzle,

as shown in Figure 36. Moreover, the filament can buckle due to extrusion forces causing even more friction.

There is an excellent match between the nozzle pressure data and the theory for a type 3 nozzle. The extrusion pressure is higher than the theory because of entrance effects.

*Comparison of nozzle types*

Table 4 shows the important differences between the nozzle types.

| Type | $D_d$ (mm) | Plateau |
|---|---|---|
| 1 | 0.8 | Yes |
| 2 | 0.4 | Yes |
| 3 | 0.4 | No |

Table 4: Important differences between nozzle types. $D_d$ is the die diameter.

The results of an experiment with a type 2 nozzle are shown in Figures 37 and 38. This nozzle has the same die diameter as nozzle type 3, but it has a plateau.

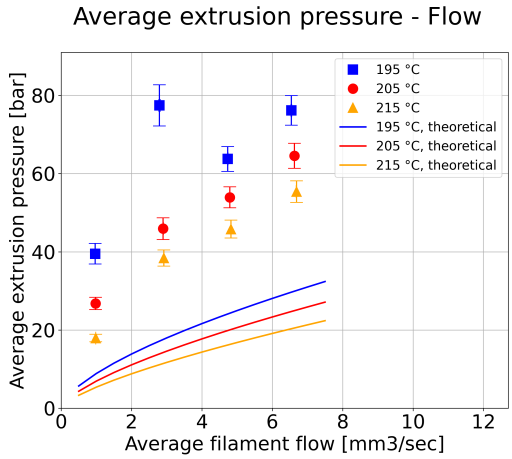


Figure 37: Extrusion pressure in a type 2 nozzle.

The experimental extrusion pressure and nozzle pressure are about 4% larger with the type 3 nozzle, compared to the type 2 nozzle. These values are within the same range as the error of the experiments, so the measured pressures in a type 2 and type 3 nozzle are approximately the same. However, the theoretical pressure in a type 2 nozzle is lower. The difference between these two nozzles is that nozzle type 2 has a plateau. The sudden change in nozzle diameter causes a pressure drop that is not accounted for in Equation 7, which results in an underestimation of the experimental pressure drop throughout all the flows and temperatures [34]. The larger mismatch with nozzle type 2 compared to nozzle type 3 suggests that the theory should not neglect the pressure drop over the plateau and a correction has to be made. Additionally, similar to nozzle type 3, due to entrance effects the mismatch between the theory and the extrusion pressure is higher compared to the mismatch between the theory and the nozzle pressure.

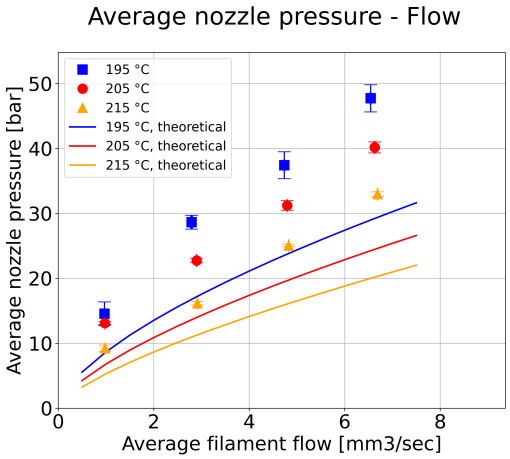


Figure 38: Nozzle pressure in a type 2 nozzle.

Interestingly, in nozzle types 2 and 3, the extrusion pressure around a flow of 3 $mm^3/s$ and a temperature of 195 °C is higher than the extrusion pressure around a flow of 5 $mm^3/s$ with the same temperature. This is not in line with the theory and requires a closer look. Note that this behaviour is not visible in the nozzle pressure graphs. Nozzle types 2 and 3 have been tested with similar temperatures, but with feed rates ranging from 1.6 to 4.4 $mm^3/s$. The results of the extrusion pressure for a type 3 nozzle are shown in Figure 39. The graph clearly shows a gradual increase and decrease in extrusion pressure. It happens with all three temperatures, although it is more extreme for lower temperatures. Figure 41 shows the results of the extrusion pressure for a type 2 nozzle. The results are similar. Figure 40 shows the graph of a single test. It is a test with a type 2 nozzle, a temperature of 195 °C and a feed rate of 2.8 $mm^3/s$.

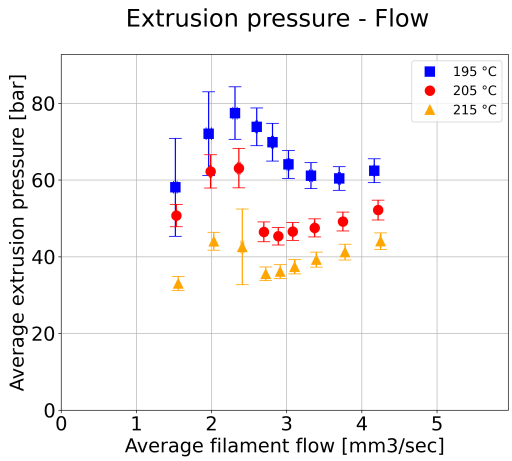


Figure 39: Extrusion pressure versus flow around a flow of 3 $mm^3/s$ within a type 3 nozzle.

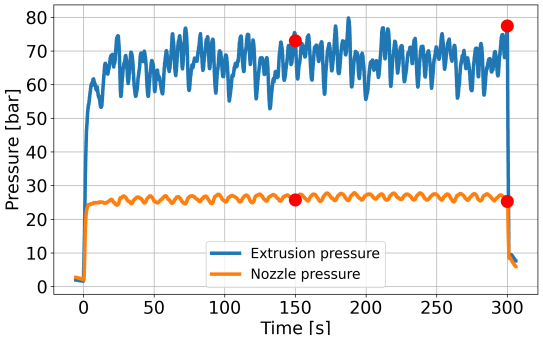


Figure 40: A single test with feed rate of 2.8 $mm^3/s$ shows fluctuations in the extrusion pressure and the nozzle pressure. The fluctuations in the extrusion pressure are about 20 bar.

Although this is a steady state test, the extrusion pressure has fluctuations of up to 20 bar, which is high. As a comparison, extrusion pressure fluctuations in other tests are about 5 bar. The nozzle pressure fluctuates as well, but is more damped. The average value of the extrusion pressure is higher than expected, the average nozzle pressure is in line with expectations. Therefore the cause of this anomaly must lie above the point where the nozzle pressure is measured. Even at steady state, the melt behaves dynamically and its height moves up and down during extrusion. According to Serdeczny et al. [18], that is because the backflow functions as a heat conductor between the nozzle wall and the solid filament which increases the heat transfer rate. As a result, the temperature increases, the viscosity decreases and the pressure drops.

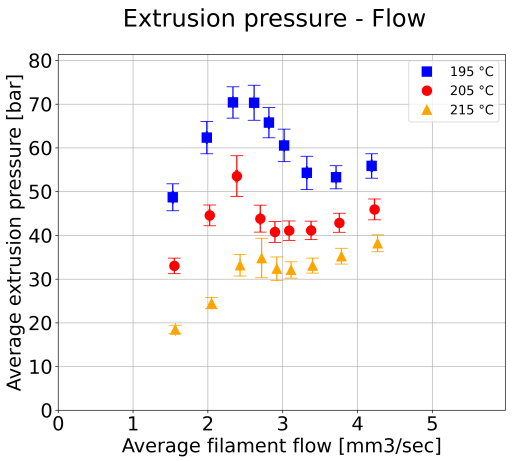


Figure 41: Extrusion pressure versus flow around a flow of 3 $mm^3/s$ within a type 2 nozzle.

The pressure drop causes the backflow to sink. Therefore, the heat transfer rate reduces, the temperature reduces and the viscosity of the melt increases. Consequently, the pressure increases, resulting in a higher backflow which causes the cycle to repeat itself. The hypothesis is that with a flow of 3 $mm^3/s$, the height of the melt outreaches the length of the nozzle and flows into the heat break. Figure 42 illustrates this phenomenon.

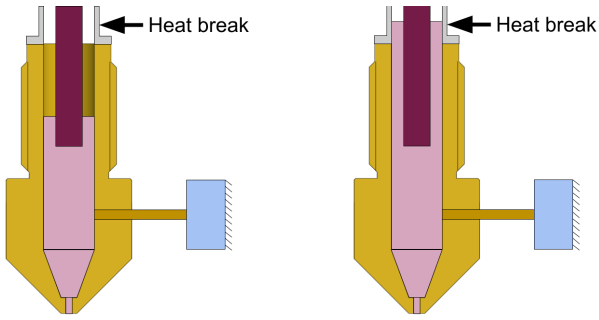


(a) Melt height is within the nozzle. It can fluctuate but it stays below the heat break.

(b) Melt height exceeds the length of the nozzle and flows into the heat break.

Figure 42

The heat break is a very thin part of the liquefier that separates the nozzle from the cold end. It has a low thermal conductivity so the temperature gradient in this region is large. When the melt enters the heat break, it rapidly cools down and starts to stick to the sides, creating a large friction force and blocking the entrance of the nozzle. This temporarily slows the throughput of new filament, which results in a decrease of pressure in the nozzle. The

feeder starts to push the filament with a higher force. Once the friction force is overcome, the polymer is pushed back in to the nozzle with great force. The pressure increases and the melt flows back in to the heat break again. This explains the sharply fluctuating peaks in the graph of Figure 40. It also explains why the average extrusion pressure is high, whereas the average nozzle pressure is not influenced.

The results for a type 1 nozzle are shown in Figures 43 and 44, for the extrusion pressure and nozzle pressure, respectively.

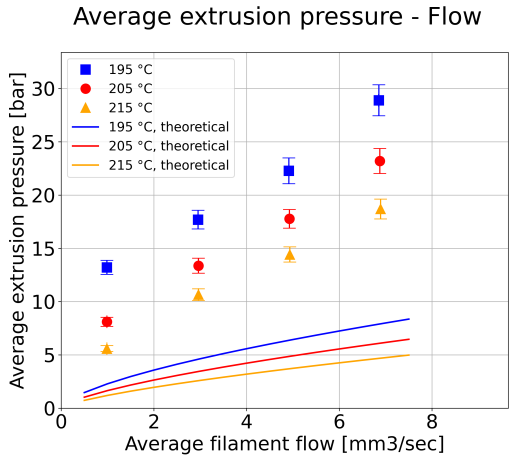


Figure 43: Extrusion pressure in a type 1 nozzle.

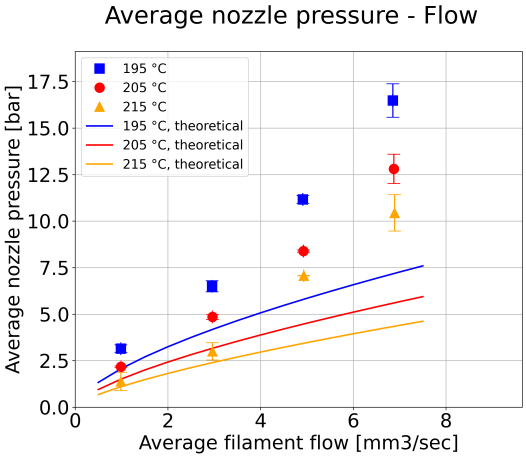


Figure 44: Nozzle pressure in a type 1 nozzle.

Compared to nozzle types 2 and 3, these graphs show lower absolute pressure values for the experimental extrusion pressure, experimental nozzle pressure and the theoretical calculations. This is expected because the nozzle die diameter for a type 1 nozzle is twice as large as the nozzle die diameter of the type 2 and 3 nozzle; the polymer flows through a larger area. The mismatch between the experimental data and the theory can be explained. Similar to nozzle type 2, the theory underestimates the experiments because it neglects the pressure drop over the plateau. Additionally, similar to nozzle types 2 and 3, due to entrance effects the mismatch between the theory and the extrusion pressure is higher compared to the mismatch between the theory and the nozzle pressure. Moreover, the mismatch increases at higher flows for the extrusion pressure and nozzle pressure.

A second experiment uses the same nozzle, but extrudes at higher flows. The results of that experiment have been plotted in the same graph as the theory. This is shown in Figures 45 and 46 for the extrusion pressure and nozzle pressure, respectively. Note that the temperatures are different in this experiment. That is because Ultimaker printers print at higher temperatures at these flows when using the type 1 nozzle. It was chosen to do the experiments with Ultimaker print settings to simulate their extrusion process.

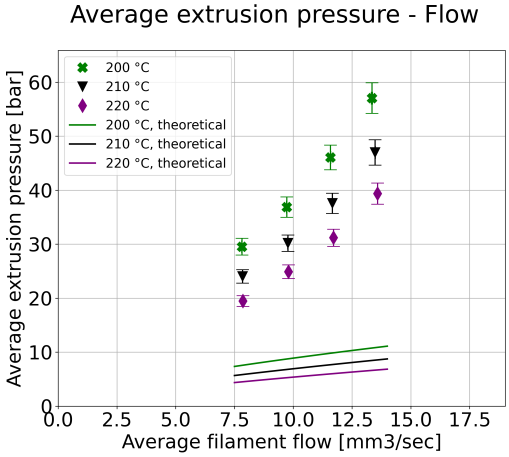


Figure 45: The theoretical extrusion pressure plotted against experimental data for higher flows and higher temperatures.

These results confirm the previous findings: due to entrance effects the mismatch between theory and experimental pressure is higher for the extrusion pressure compared to the nozzle pressure, and the mismatch between the theory and the experimental data deviates more at increasing flows. The latter could be explained

by the non-uniform temperature in the nozzle. The solid, cold filament that enters the nozzle decreases the average temperature of the melt. At higher flows, the throughput of new, cold filament is higher which means that the average temperature drops further. With lower temperatures, the viscosity of the melt is higher resulting in a higher pressure.

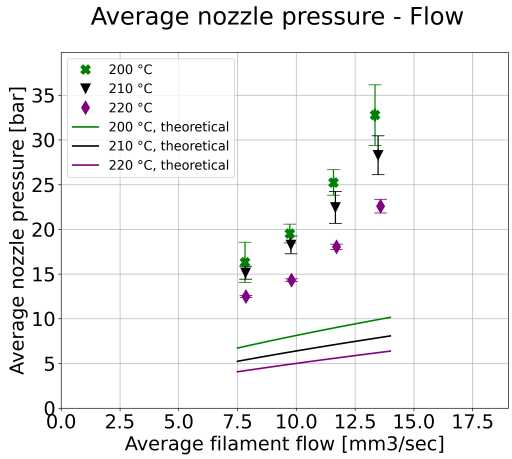


Figure 46: The theoretical nozzle pressure plotted against experimental data for higher flows and higher temperatures.

Additionally, the elasticity of the polymer could increase the pressure as well [35]. Due to the viscoelasticity of the polymers, when a stress is applied, the polymer rearranges at a molecular level; parts of the polymer chain change position. This effect creates back stress in the polymer and as a result, its elongational viscosity increases, resulting in a higher pressure. This effect is larger at higher flows.

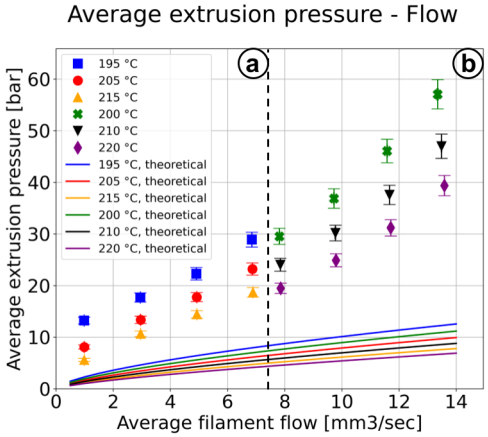


Figure 47: Extrusion pressure versus flow for a type 1 nozzle with PLA. This graph is a combination of two experiments. a) is an experiment at low flows. b) is an experiment at high flows.

The geometry of the nozzle influences the pressure during extrusion. In a nozzle with no plateau, the experimental nozzle pressure data and the theory have a good match for flows between 1 $mm^3/s$ and 7 $mm^3/s$ and temperatures between 195 °C and 215 °C. However, the theory must be corrected for nozzles with a plateau. A larger nozzle die diameter results in a lower pressure drop. Entrance effects increase the mismatch between the theory and extrusion pressure. Temperature non-uniformity and polymer elasticity could explain the increasing mismatch at higher flows.

*Materials*

Four different materials have been tested to see if the design set-up is able to measure the pressure in multiple pseudoplastic melts. The viscosity curves for PETG, PC and Nylon were only available for a single temperature. Rheological properties such as those in Table 2 were not available for these materials. Consequently, the viscosity curves for different temperatures could not be calculated using the Cross equation and the Arrhenius equation. Therefore, tests with these materials have been done at a single temperature; that of which the viscosity curve was available. A partner of Ultimaker provided the viscosity curves, which are shown in Appendix E.1. Figures 47 to 54 show the extrusion pressure and nozzle pressure curves for PLA, PETG, PC and Nylon tested with a type 1 nozzle.

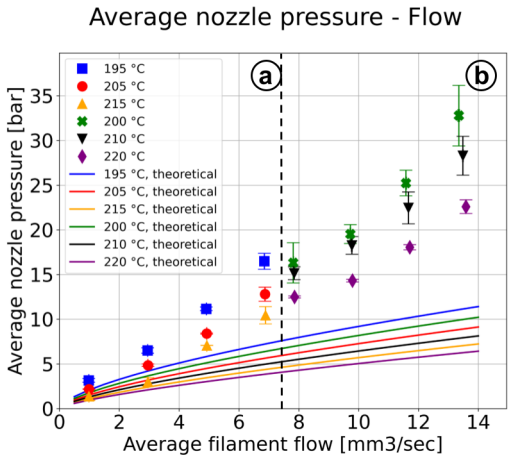


Figure 48: Nozzle pressure versus flow for a type 1 nozzle with PLA. This graph is a combination of two experiments. a) is an experiment at low flows. b) is an experiment at high flows.

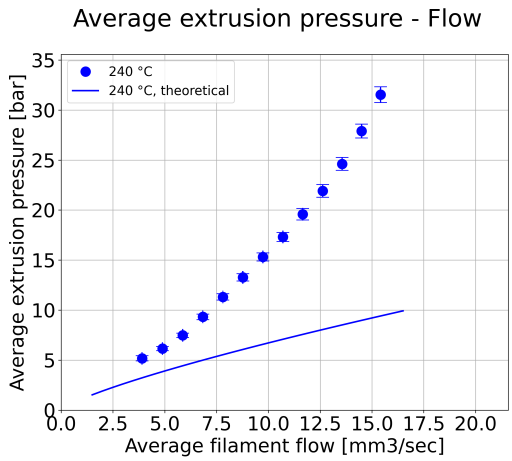


Figure 49: Extrusion pressure versus flow for a type 1 nozzle with PETG.

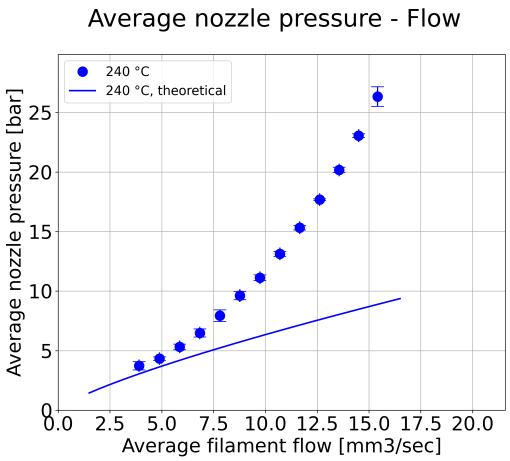


Figure 52: Nozzle pressure versus flow for a type 1 nozzle with PETG.

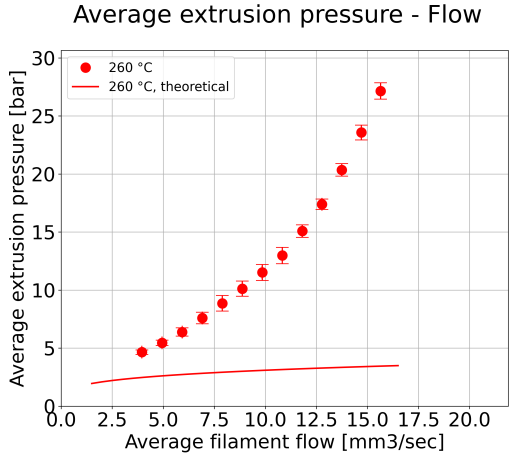


Figure 50: Extrusion pressure versus flow for a type 1 nozzle with PC.

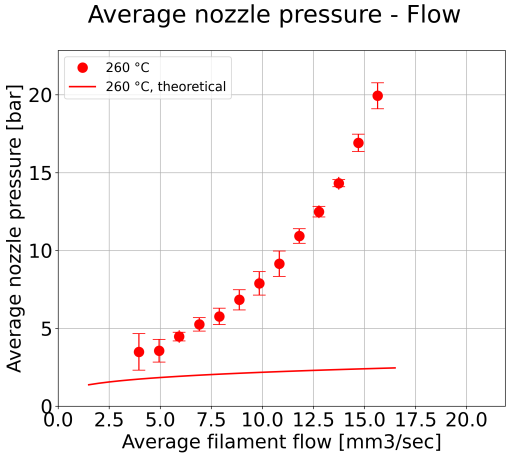


Figure 53: Nozzle pressure versus flow for a type 1 nozzle with PC.

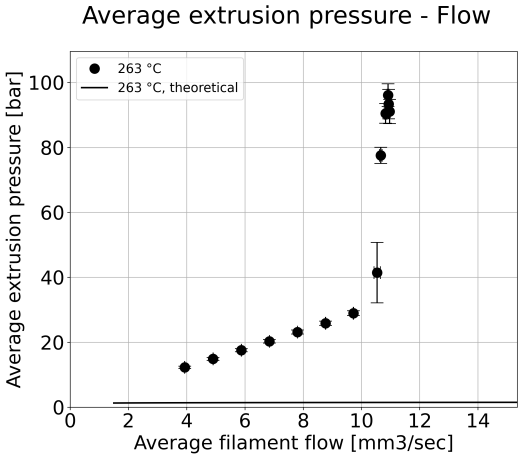


Figure 51: Extrusion pressure versus flow for a type 1 nozzle with Nylon.

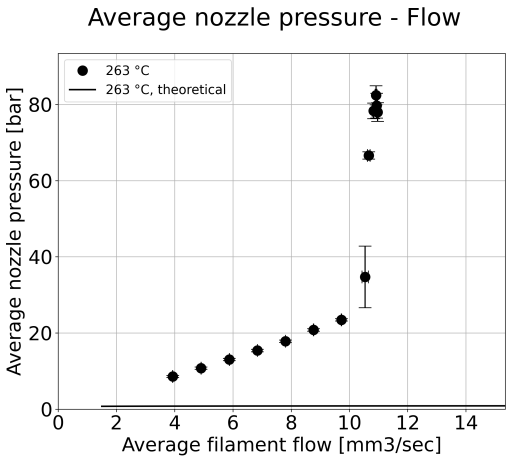


Figure 54: Nozzle pressure versus flow for a type 1 nozzle with Nylon.

The pressure data from these experiments also increases at higher flows. Additionally, it is repeatable; a repetition of tests resulted in the same pressure value. Although the absolute values of the pressures differ between materials, the trend of the graphs look similar. All theoretical extrusion pressures and nozzle pressures underestimate the experimental data. The experimental data deviates away from the theory at higher flows. Figures 55 and 56 show the pressure difference between the experiments and the theory for each material at three different flows.

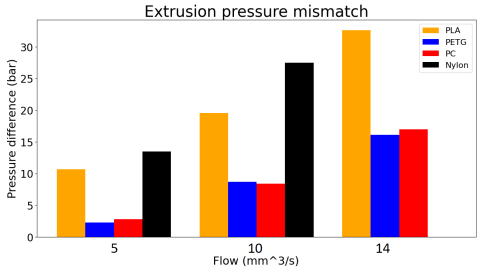


Figure 55: Extrusion pressure mismatch at three flows. Nylon has been excluded at a flow of 14 $mm^3/s$.

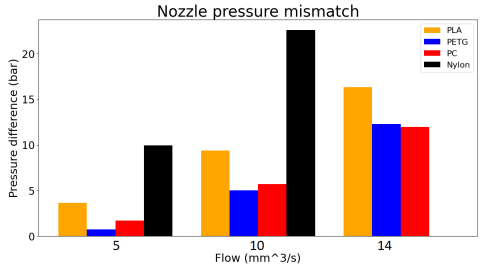


Figure 56: Nozzle pressure mismatch at three flows. Nylon has been excluded at a flow of 14 $mm^3/s$.

For all the materials and flows, the mismatch is larger in the extrusion pressure, which confirms that the entrance effects also play a role with other materials. However, for each material, the mismatch between measured pressure and theoretical pressure is different. This study cannot explain the difference in mismatch between the materials. However, Schuller et al. [36] are working on identifying the dimensionless mobility factor $\alpha$ for FFF printable polymers. The mobility factor gives more insight into material specific shear-thinning and elastic normal stresses. This might explain the difference in mismatch between the materials, although more research is needed.

With Nylon, there is a sudden pressure increase above feed rates of 11 $mm^3/s$, illustrated in Figures 51 and 54. Due to the high forces, the feeder cannot push the filament down and slips, resulting in an average flow speed that does not exceed 11 $mm^3/s$. Unlike the spike of extrusion pressure with PLA, as described in section *Comparison of nozzle types*, this pressure spike is also visible in the nozzle pressure. It indicates that the extreme pressure drop does not happen in the heat break, but somewhere below the point at which the nozzle pressure is measured. The author believes the failure is due to cold extrusion. That means that the solid filament can not melt quickly enough before it reaches the nozzle die, thereby clogging the nozzle. The pressure monitoring set-up is capable of detecting the high pressures even when the feeder fails. Moreover, the similar abrupt increase in extrusion pressure and nozzle pressure show that the origin of the defect lies below the pin.

The pressure monitoring set-up is capable to measure the pressure with different materials. Moreover, it is able to measure the difference in pressure drop between the materials. More research is needed into the material properties to explain the differences in the graphs and different mismatch with the theory.

## Conclusions

In this study, a novel way of monitoring the pressure inside the nozzle of a fused filament fabrication 3D printer has been designed and tested. The set-up has been found to reliably and repeatedly measure the pressure of the melt with different materials and nozzle geometries, at different temperatures and flows. In parallel, the pressure has been measured at the top of the nozzle, as proposed by previous studies. The pressure measured inside the nozzle behaves similarly to the pressure measured at the top of the nozzle, albeit at lower absolute values. Moreover, the pressure measured inside the nozzle has a better match with theoretical pressure calculations compared to the pressure monitoring set-up from previous studies. That is because entrance effects do not influence the nozzle pressure measurements. As expected, the mismatch between the theory and the ex-

perimental values varies with different nozzle geometries, temperatures, flows and materials. Generally, the experimental values deviate further from the theory at higher flows. This can be explained by the non-uniform temperature of the melt and the viscoelastic behaviour of the polymers, which play a larger role at higher flows. The theory matches the experimental nozzle pressure data very well for a nozzle without plateau, which indicates that the theory must be corrected to account for the pressure drop over a plateau.

In this study, non-linearities such as entrance effects, temperature non-uniformity and elastic melt behaviour are unprecedentedly captured by experimental data, for a range of materials. This novel way of monitoring the pressure inside the nozzle of an FFF 3D printer has proven to outperform the strategy that measures the pressure at the top of the nozzle. It provides the next step in using experimental pressure data to understand the complex dynamics of the extrusion process. Thereby, it enables a new possibility to develop improved extrusion control strategies.

### Acknowledgements

This study has been a collaboration between Delft University of Technology and Ultimaker. The author would like to thank Can Ayas for supervising this study on behalf of Delft University of Technology, and the involved employees of Ultimaker for their support and advice during the project: Paola Fanzio, Sam Kent, Koos Welling, Maqsood Alam, Ron van Dorssen, Siert Wijnia and Marc Joosen. The author would also like to thank Francisco Galindo-Rosales and Tomás Schuller Almeida Graça Barbosa from University of Porto for their contributions and insightful conversations.

## Bibliography

[1] Ugur M. Dilberoglua, Bahar Gharehpapagha, Ulas Yamana, and Melik Dolena. The role of additive manufacturing in the era of industry 4.0. *Procedia Manufacturing*, 11:545–554, 2017.

[2] J. A. Slotwinski. Additive manufacturing: Overview and nde challenges. *AIP Conference Proceedings*, 1581(1173), 2014.

[3] Michele Moretti, Federico Bianchi, and Nicola Senin. Towards the development of a smart fused filament fabrication system using multi-sensor data fusion for in-process monitoring. *Rapid Prototyping Journal*, 26(7):1249–1261, 2020.

[4] Eric Garner, Helena M. A. Kolken, Charlie C. L. Wang, Amir A. Zadpoor, and Jun Wu. Compatibility in microstructural optimization for additive manufacturing. *Additive Manufacturing*, 26:65–75, 2019.

[5] Kaufui V. Wong and Aldo Hernandez. A review of additive manufacturing. *ISRN Mechanical Engineering*, 2012(208760):10, 2012.

[6] J. Giannatsis, V. Dedoussis, and D. Karalekas. Architectural scale modelling using stereolitography. *Rapid Prototyping Journal*, 8(3):200–207, 2002.

[7] Ian Gibson, Thomas Kvan, and Ling Wai Ming. Rapid prototyping for architectural models. *Rapid Prototyping Journal*, 8(2):91–95, 2002.

[8] Richard van Noort. The future of dental devices is digital. *Dental Materials*, 28(1):3–12, 2012.

[9] F. Rengier, A. Mehndiratta, H. von Tengg-Kobligk, C. M. Zechmann, R. Unterhinninghofen, H. U. Kauczor, and F. L. Giesel. 3d printing based on imaging data: review of medical applications. *Int J Cars*, 5:335–341, 2010.

[10] Peter Shih-Hsin Chang, Thornwell H. Parker, Charles W. Jr Patrick, and Michael J. Miller. The accuracy of stereolitography in planning craniofacial bone replacement. *Journal of Craniofacial Surgery*, 14(2):164–170, 2003.

[11] Ilias El Aita, Jhinuk Rahman, Jorg Breitkreuz, and Julian Quodbach. 3d-printing with precise layer-wise dose adjustments for paediatric use via pressure-assisted microsyringe printing. *European Journal*

*of Pharmaceutics and Biopharmaceutics*, 157:59–65, 2020.

[12] Michael E. Mackay. The importance of rheological behavior in the additive manufacturing technique material extrusion. *Journal of Rheology*, 62(6):1549–1561, 2018.

[13] Vladimir E. Kuznetsov, Azamat G. Tavitov, Oleg D. Urzhumtsev, Mikhail V. Mikhalin, and Alexander I. Moiseev. Hardware factors influencing strength of parts obtained by fused filament fabrication. *Polymers*, 11(11), 2019.

[14] C. K. Chua, K. F. Leong, and C. S. Lim. *Rapid Prototyping: Principles and Applications*. World Scientific Publishing, 2010.

[15] Jim Flowers and Matt Moniz. Rapid prototyping in technology education. *The Technology Teacher*, pages 7–11, 2002.

[16] Eric L. Gilmer, Darren Miller, Camden A. Chatham, Callie Zawaski, Jacob J. Fallon, Allison Pekkanen, Timothy E. Long, Christopher B. Williams, and Michael J. Bortner. Model analysis of feedstock behavior in fused filament fabrication: Enabling rapid materials screening. *Polymer*, 152:51–61, 2018.

[17] Sung-Hoon Ahn, Micheal Montero, Dan Odell, Shad Roundy, and Paul K. Wright. Anisotropic material properties of fused deposition modeling abs. *Rapid Prototyping Journal*, 8(4):248–257, 2002.

[18] Marcin Piotr Serdeczny. Numerical and experimental analysis of filament-based material extrusion additive manufacturing. *Technical University of Denmark*, 2020.

[19] Anna Bellini, Selcuk Güceri, and Maurizio Bertoldi. Liquefier dynamics in fused deposition. *Journal of Manufacturing Science and Engineering*, 126:237–246, 2004.

[20] Timothy J. Coogan and David O. Kazmer. In-line rheological monitoring of fused deposition modeling. *Journal of Rheology*, 63:141–155, 2019.

[21] David D. Phan, Jeffrey S. Horner, Zachary R. Swain, Antony N. Beris, and Michael E. Mackay. Computational fluid dynamics simulation of the melting process in the fused filament fabrication additive manufacturing technique. *Additive Manufacturing*, 33:101–161, 2020.

[22] David A. Anderegg, Hunter A. Bryant, Devante C. Ruffin, Stephen M. Skrip Jr., Jacob J. Fallon, Eric L. Gilmer, and Michael J. Bortner. In-situ monitoring of polymer flow temperature and pressure in extrusion based additive manufacturing. *Additive Manufacturing*, 26:76–83, 2019.

[23] Tomás Rodrigues, Francisco J. Galindo-Rosales, and Laura Campo-Deaño. Towards an optimal pressure tap design for fluid-flow characterisation at microscales. *Materials*, 12(1086), 2019.

[24] Chris Rauwendaal. *Understanding Extrusion*. Hanser Publishers, 2010.

[25] Steve Carter, Alex Ned, John Chivers, and Andy Bemis. Selecting piezoresistive vs. piezoelectric pressure transducers. *General Measurement*, 2018.

[26] Timothy J. Coogan and David O. Kazmer. Modeling of interlayer contact and contact pressure during fused filament fabrication. *Journal of Rheology*, 63:655–672, 2019.

[27] M. Moretti, A. Rossi, and N. Senin. In-process simulation of the extrusion to support optimisation and real-time monitoring in fused filament fabrication. *Additive Manufacturing*, 38, 2021.

[28] Yedige Tlegenov, Geok Soon Hong, and Wen Feng Lu. Nozzle condition monitoring in 3d printing. *Robotics and computer integrated manufacturing*, 54:45–55, 2018.

[29] Antreas Kantaros and Dimitrios Piromalis. Employing a low-cost desktop 3d printer: Challenges, and how to overcome them by tuning key process parameters. *International Journal of Mechanics and Applications*, 10:11–19, 04 2021.

[30] Ultimaker. *Ultimaker PLA technical data sheet*, April 2022.

[31] DSM. *DSM Novamid ID 1030 Nylon 6/66, 3D Printing Grade*, April 2022.

[32] Ultimaker. *Ultimaker PETG technical data sheet*, April 2022.

[33] MatWeb. Dsm novamid id 1030 nylon pa6/66, 3d printing grade.

[34] Peter van Puyvelde, Marc Mangnus, and Anja Vananroye. On the pressure dependency of the bagley correction. *International Polymer Processing Journal of the Polymer Processing Society*, 2013.

[35] Walter Michaeli. *Extrusion Dies for Plastics and Rubber*. Hanser Publishers, 2 edition, 1992.

[36] Tomás Schuller, Paola Fanzio, and Francisco Galindo-Rosales. Analysis of the importance of shear-induced elastic stresses in material extrusion. *Additive Manufacturing*, 57, 2022.

[37] Yang Lyu, Jianguang Pang, Zijian Gao, Qingliang Zhang, and Xinyan Shi. Characterization of the compatibility of pvc/-pla blends by aid of rheological responses. *Polymer*, 176:20–29, 2019.

# Reflection

At the start of the project, I thought that 3D printing was easy; pushing plastic through a hot tube and move it around. I was wrong. Quickly, I realised that 3D printing is much more complex and requires a broad range of expertise to get it right. It takes great effort to get the interaction of materials, hardware and software right. Additionally, being able to operate a 3D printer is more difficult than I expected. It requires a lot of know how and experience to produce better prints. It is save to say that I learned a lot about 3D printing, especially in the field of extrusion. I never imagined all the phenomena that influence the extrusion process such as temperature uniformity, non-linear viscosity profiles, pressure drops, backflow, retractions, vortices, thermal expansion, compression etc. On top of that, they are all dependent on each other which creates a very complex situation. I remember trying to visualise everything that happened inside the nozzle and finding which phenomena influence each other and I ended up with a scrapbook full of notes and arrows; a complete mess. Simultaneously it was very insightful, I learned to zoom out, take a step back and look at the bigger picture. Not every detail on the subject is important, but what is important is to figure out which part of the problem is relevant, and which ones can be simplified.

## Project

The idea to measure the pressure inside the nozzle has existed for a long time within Ultimaker. When I signed up for the challenge I was quickly surrounded by enthusiastic colleagues, with a lot of expertise on the subject, who were willing to help me. That is one of the things I liked the most; it felt like I was in charge and did most of the decision making, but I had a team of experts that I could always reach out to and ask for advice or help in any way. I am very thankful for that and it made the project even more interesting. Especially because everybody had different ideas about how to tackle the problem and it was my job to dive deep into each idea to find a balance and come up with a feasible solution. It taught me a lot in terms of decision making, working efficiently and staying goal oriented.
Moreover, I liked that the project started from scratch and I was involved in the entire process. It taught me how to translate a research goal into an implementation strategy, which I think is a very useful skill to possess. The project started with research into literature and pressure monitoring techniques and evolved into concept planning and initial design sketches. The designs became more detailed until they were ready to be manufactured. I made virtual parts in SolidWorks and mechanical drawings that could be sent to the supplier. I had contact with several manufacturers and ordered the parts. When they were delivered I assembled everything, did a few tests and made some design improvements. I was in charge of testing, data analysis, theoretical pressure calculations and presenting the process to my colleagues. In other words, the multidisciplinary scope of the project is what I liked a lot and what I learned from the most.

Delft University of Technology teaches practical skills in forms of practical assignments or group projects which I think is crucial for any engineer. However, in this internship that practical experience has far exceeded anything I have done so far. Getting my hands dirty with printing, soldering, cables, programming, working with SolidWorks, making drawings, using Product Data Management (PDM) to actually create, print or order components to see how they work in real life is a valuable lesson. It has shown me a more realistic side of engineering: no matter how hard you think of all problems and solutions, reality can prove you wrong and sometimes it is more efficient to make a decision and try it out rather than trying to think everything through.

### Personal

Things that have helped me during the process is that I am not afraid to reach out to other people to ask for their expertise or help. This is especially true for colleagues with another field of expertise. They are keen to share their knowledge to an eager pair of ears. In this way it is possible to approach problems from multiple points of view creating a more complete sketch of the issue, and thus a more creative solution oriented way of thinking is possible. Moreover, I have been a team player since I can remember, which means that I can easily share all my findings and discuss them with others. In fact, I think a sparring partner is crucial for efficient progress, even for small issues. On the contrary, this means I need more confirmation before taking initiative in taking the next step. Especially so with practical things. I have tried to improve myself on this area, but I can still make progress there. Currently, I do still tend to ask the opinion of other people before undertaking action.

In fact, during my thesis, I found that I tend to overthink before I go to action. With every idea or solution I immediately try to find the drawbacks. This can be a good and a bad habit. For example, this critical mindset has helped me solve the leakage issue in detail, which makes me understand it and be able to present it in a logical manner. The critical mindset has also helped me find an error in the theory, a theory that is widely used. Additionally, it helps me reflect on myself and allows me to improve myself. However, it is time consuming and not always possible to foresee everything. Sometimes, it is better to make a few assumptions and get to action, because doing things can give critical insights which makes it easier to solve the problem.

Something that I learned about myself is that I appreciate the bigger picture. When I am burying my head deep into theory or a detail I like to ask myself questions such as: What is the motive for doing this, who will benefit, why do I do it this way, what are the alternatives? I have noticed that I am less interested in the purely technical part of a problem, and more interested in the overall scope of the project. To know a few things about everything appeals more to me than knowing everything about a few things. I believe that this was always inside me and that it is one of the reasons why I specifically wanted to graduate at a company. For example, during lunch breaks or at the coffee machine I could speak to different people about supply chain, about manufacturing, sales, IT, marketing or any other topic related to a company.

### Company

This internship has taught me work experience, something I value a lot. Things like contacting external companies, communicating with colleagues, securely sharing and documenting of the process, working in a team, handling legal concerns such as confidentiality and taking responsibility for your part of the work are all important aspects of a job in engineering. Besides time management, which is something crucial in university projects as well, the relevance of costs is very high in a commercial company. My wish to graduate at a company to get familiar with their way of working and get work experience was more than granted. Not only did I get my share of work experience, but I have witnessed a company during Covid times, I have witnessed a reorganisation and its impact on people, I have witnessed a merger with a company on the other side of the Atlantic ocean.
The whole 3D printing environment inspires creativity and I am intrigued by the mechatronics side of it, which motivates me. This field of engineering is fun and has a great impact on the industry, of which Ultimaker is one of the leading companies. The people within Ultimaker share that same passion resulting in a curious attitude towards the projects around the company, including the sensorised nozzle project. With their flat organisational structure, it is easy to speak to all colleagues informally, disregarding their position in the company, which creates a pleasant working environment.

## Afterword

In general, I look back at a fun and exciting project from which I have learned a lot. I met a lot of people and had great experiences. I look forward to joining Ultimaker as a junior mechanical engineer to further explore the amazing world of 3D printing. I wish to thank Can Ayas for supervising me on behalf of Delft University of Technology. I wish to thank Paola Fanzio and Sam Kent for taking the roles as supervisor on behalf of Ultimaker and guiding me in the development of this work. I would also like to thank all the colleagues that were involved in the project such as Koos Welling, Maqsood Alam, Ron van Dorssen, Siert Wijnia and Marc Joosen. Lastly I would like to thank the other colleagues at Ultimaker for their openness, enthusiasm and for sharing their ideas and expertise which have been very helpful in the development process.

# Appendices

# A Experiment design

This appendix describes in detail how the experimental set-up was designed, calibrated and assembled. The limits of the system and the assumptions made are also described.

## A.1 Concept selection

Measuring the pressure of a fluid in general is not that difficult and can be done in various different ways. Numerous types of pressure sensors exist on the market, which measure the pressure directly or indirectly. An example of measuring the pressure indirectly is by using a force sensor. The pressure can be calculated as long as the area over which the force is transferred is known according to

$$P = \frac{F}{A} \tag{9}$$

where $P$ is pressure, $F$ is the measured force and $A$ is the area over which the force is transferred. Pressure inside a tube creates stress in its walls which causes the tube to expand. Therefore, strain sensors on the wall of a pressure vessel could also be used to measure the pressure indirectly.

Measuring the pressure of a molten polymer inside the nozzle of a 3D printer is much more complex. A suitable sensor has to be capable of overcoming a combination of a few extreme conditions. For example, it should be a miniature sensor because the diameter of standard nozzles is around 3 mm. Additionally, 3D printers operate at temperatures of at least 200 ℃, so the sensor has to be heat resistant and cannot be influenced by a difference in temperature. Pressures are expected to go up to 94 bar. This value comes from previous internal research done by Ultimaker where they measured the compressive force of the filament before it entered the nozzle. Those forces reached 60 N. The area of the filament is $6.3794 * 10^{-6}$ m$^2$. By assuming that all of the compressive force comes from the pressure that is applied to the area of the filament, using equation 9 results in a pressure of approximately 94 bar. The sensor must also influence the flow of the molten material as little as possible to minimise the observer effect; observing a situation will change it. Possible leakage of the nozzle due to a design change can cause problems and must be avoided. In between measurements, the temperatures will drop and the polymer changes state. A sensor placed directly in the flow must therefore be able to withstand solidification on its measuring membrane. Preheating of the nozzle (and printing process) takes too long for a dynamic way of measuring steady state extrusion, which means that piezoelectric sensors are not a viable option because they dissipate charge over time and need to be constantly re-calibrated for longer measurements. Pressure at any point is equal in all directions which is convenient because orientation of possible sensors is not relevant. However, placement of the sensor is crucial because the pressure is not equal at any point in the flow.

Finally, to understand the current print process better, the sensor must be implemented in the current printhead design, so as to replicate the actual process as well as possible and not accidentally measure other phenomena. This means that the whole system has to be redesigned as little as possible. Obviously, the costs of the design have to be minimised as well.

One of the concepts that was evaluated uses a pressure transducer, see Figure 57.

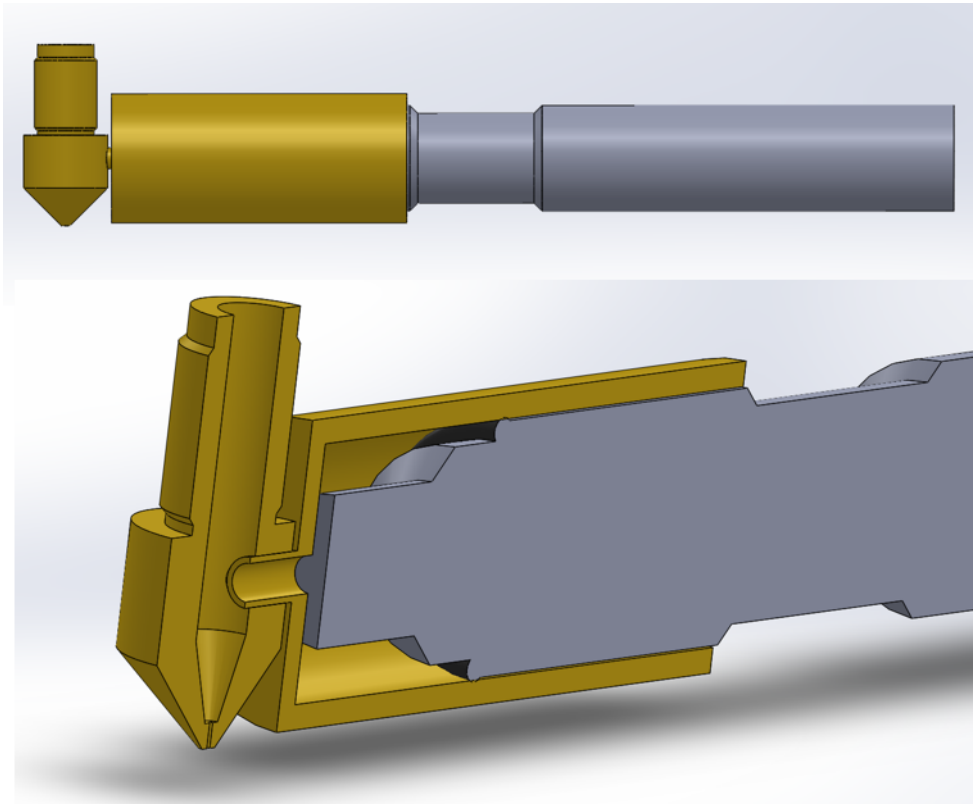

Figure 57

The advantage of this design is that the sensor is designed to measure the pressure in plastics (during injection moulding) and it is an off-the-shelf solution. In other words, the sensor will work and it requires little effort to measure with it. However, due to the size of the sensor, it requires a big modification of the nozzle. Note that this is one of the smallest pressure transducers in the market but it is still large for the nozzle of an FFF 3D printer. It cannot be placed directly into the melt, because its diameter is larger than that of the nozzle, so the idea was to add a chamber to the nozzle that would fill itself with the melt. This induces a few problems such as filament degradation in the chamber and leakage between the chamber and the nozzle. Moreover, because of the size of the chamber compared to the nozzle, the chamber must be separately heated to keep the temperature the same as the nozzle. The pressure would not be measured inside the nozzle, but away from it, so the relevance of the measurements would be dubious. It is not an ideal solution.

A second concept uses fiber Bragg grating (FBG) to measure the strain of the nozzle during extrusion, see Figure 58.

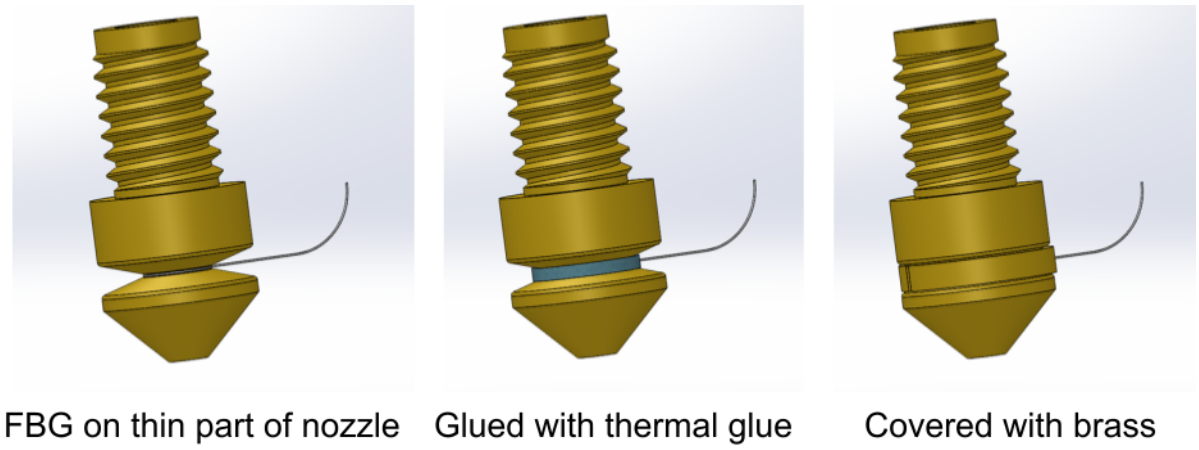


Figure 58

The nozzle strains due to a difference in temperature and pressure. The strain due to temperature is larger, so an accurate local measurement of the temperature is required. The strain due to temperature would be lower with a thinner nozzle wall and the strain due to pressure would be bigger with a thinner nozzle wall. Therefore, it was chosen to cut away part of the nozzle wall and place the fiber Bragg grating on a thin-walled part of the nozzle. The cut-away would be filled with thermal glue and extra brass to decrease the loss of heat flow towards the tip of the nozzle. The advantage of this concept is that it does not influence the flow and it requires little space. In fact, this concept could be placed in nozzles used in 3D printers to measure the pressure in-line. However, it is an expensive solution. Moreover, every nozzle is equipped with its own sensors and cannot be interchanged; it is impossible to swap nozzles without swapping the sensor. It is preferred to swap nozzles because they might clog or to test different inner geometries. This design exceeded the budget for the project and has not been chosen.

The concept that has been chosen for further development is similar to what Coogan and Kazmer [20] designed, with a few improvements. The design uses a tiny pin to transfer the force exerted by the polymer to an externally mounted sensor. A schematic has been included in Figure 59. With this concept, the modified nozzles are cheap to manufacture, cheap to replace and sensor independent; nozzles can be swapped without the need to change sensors. Lead times for components are short, which is great for quick results, and the extrusion process will hardly be influenced. Moreover, experimenting with this design can be done while barely changing the printhead of an Ultimaker.

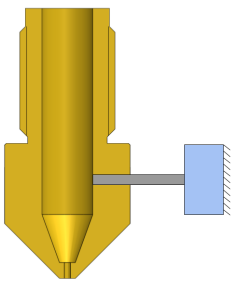

Figure 59: Schematic of the chosen concept. It roughly shows the crossection of a nozzle, a pin (in gray) and a force sensor (in blue).

This design is simple and cheap, it is a quick solution to get first-hand experiences and knowledge with pressure monitoring. The initial sketch of this concept is shown in Figure 60. The idea was to not modify the inner geometry of the nozzle to replicate a realistic extrusion process. The initial design includes leakage prevention by possibly including an O-ring. However, after consulting with O-ring manufacturers, it became clear that this was no guarantee for a leakage free set-up. Instead it would be costly to manufacture a few custom-made O-rings, which introduce a lot of friction. Some form of heat break is needed to prevent heat conducting to the sensor. It was important to make an extension of the nozzle to serve as a guidance to prevent buckling or tilting of the pin due to forces perpendicular to its axis. This image shows a thin part of the pin which serves as a hinge. This would simultaneously function as a heat break. However, the manufacturability of such a small hinge was not possible for several suppliers without increasing the costs drastically. Appendix A.4 describes the solution for these problems.

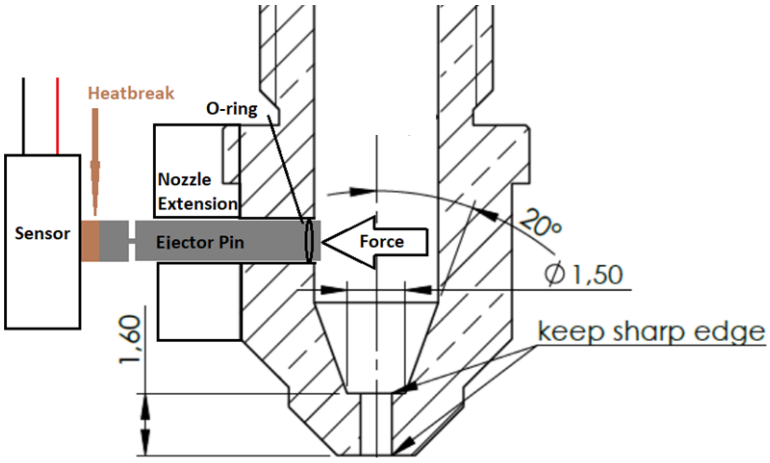


Figure 60: Simple sketch of ejector pin idea, initially

The sensor should not be attached to the nozzle because this conducts heat away from the nozzle, which would change the extrusion process. Moreover, this would heat the sensor which could influence its measurements. However, due to the vertical force that the filament exerts on the nozzle, the nozzle will move up and down a bit during extrusion. If the sensor would be externally attached, and not have the same movement, this difference in motion would induce friction forces and possibly bend the pin, resulting in a failure of the set-up. It was chosen to mount the sensor to an aluminum bracket, to which the nozzle would also be attached. In this way there is little heat conduction from the nozzle to the sensor (only through the pin). Assuming high stiffness of this design will result in a tiny difference in movement between the pin and the sensor. The thread of a nozzle, which is used to screw it into place, is randomly oriented. This is because the rotary orientation of the nozzle in a printer does not matter. In the current design, it does matter because there is limited space around the nozzle and the pin must align with the sensor. To align the pin, spacers between the nozzle and the aluminum bracket could be used. That way, the nozzle can still be tightly screwed into place, but with a different rotary orientation. This does however influence the height at which the pin is located. This height will be different for each nozzle, so the force measurements must not be influenced by the spot at which the force is applied. The final design set-up is illustrated in Appendix A.4.

## A.2 Force sensor

The expected maximum pressure is 94 bar. Using equation 9 and a pin diameter of 1 mm, the expected maximum force transferred is 7.4 N. The sensor that was chosen is a 0.78kg micro load cell, Wheatstone bridge sensor. This robust sensor can handle the maximum expected force, fits in the Ultimaker printhead, is easy to use, can be easily mounted due to its threaded holes and is cost efficient. On top of that, it is designed in such a way that the position of the force on the measuring area does not influence the measurements, which is a requirement. Figure 61 shows an image of the load cell. Figure 62 shows a mechanical drawing of the load cell.

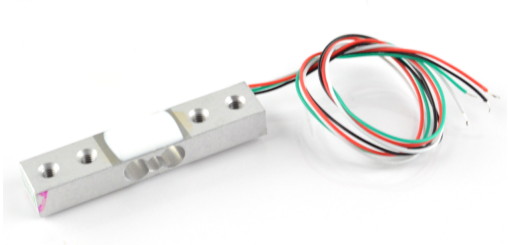

Figure 61: A 0.78kg micro load cell that was used in the experiments.

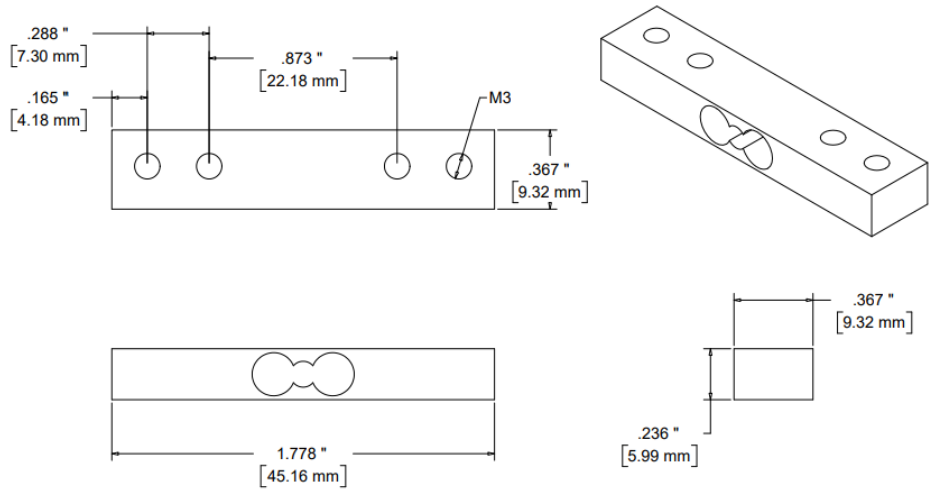


Figure 62: Mechanical drawing of the load cell.

## A.3 Sensor calibration

The feeder has been calibrated with a piece of filament marked at 270.0 mm. The filament was placed into the feeder and an extrusion distance of 270.0 mm was executed. The distance between the feeder entrance and the mark was measured with a caliper and the distance per revolution setting in the feeder configuration file was modified accordingly. This process was repeated until the mark was exactly at the entrance of the feeder three times without having to adjust the feeder configuration. The rotary encoder was calibrated by extruding 20.0 mm using the feeder. The encoder value was measured and the encoder count per distance setting in the encoder configuration file was adjusted accordingly. This process was repeated until the encoder value was within 0.01% of the feeder value three times without having to adjust the encoder configuration. Both load cells were calibrated using a Sauter FH-S force gauge mounted on a manually adjustable worm wheel. The deflection of the 0.78kg load cell during calibration was also measured with a caliper mounted to the worm wheel. An applied force of 7.0 N

corresponds with a deflection of 0.07 mm. A thermocouple was calibrated using an RS PRO temperature calibrator. That thermocouple was then used to calibrate the PT100s by sticking it into a molten polymer at 200 °C. The PID settings to maintain a constant temperature were taken from a standard Ultimaker heater block. They were tested and an overshoot of 1 °C was detected when heating from 20 °C to 200 °C. The settling time was about two seconds, so the PID settings were not adjusted.

With different nozzles, the pin touches the load cell at different points. This is explained in Appendix A.4. A second and third calibration were performed on the 0.78kg load cell, each by applying the force on a different spot. The difference between the different points was not measurable. In other words it does not matter where the pin hits the load cell, the measured force is the same.

## A.4 Assembly

This section thoroughly describes the assembly of the designed test set-up. This procedure was done every time a different nozzle was tested. Firstly, the inside of the nozzle was blasted with invertible butane duster, to remove dust or other debris that could be stuck inside the nozzle or guidance tube. The nozzle was screwed into the heater block. The thread of each nozzle is differently aligned because in a printer, the rotary orientation of the nozzle is not relevant. The heater and PT100 that stick into the heater block can only be inserted in one way, and cannot stick out in any direction due to the limited space around the nozzle. However, the thread of the heater block is also arbitrary. Different heater blocks were tried until one would fit and align well. After that, the nozzle was screwed into the cold end and into an aluminum bracket. The orientation of the nozzle with respect to the aluminum bracket is important, because the pin must be perpendicular to the surface area of the load cell for the force to be correctly applied. A spacer was used to be able to align the pin correctly. An image of the assembly so far is shown in Figure 63.

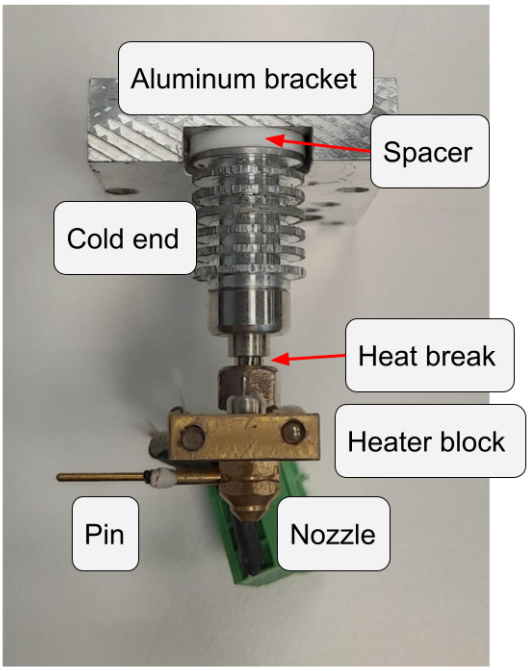


Figure 63: Front view of the basic pressure monitoring set-up. The heater block must be aligned such that its cables point backwards. A spacer is used to align the pin to the left.

The spacer creates a vertical offset. Therefore, the distance between the aluminum bracket and

the pin is different for each nozzle. A thermocouple was glued to the end of the guidance tube using Permasol Sauereisen No. 31 A/B adhesive. This glue can withstand high temperatures and is thermally conductive. The wire of the thermocouple is clamped onto the aluminum break with screws, a strap of wood and soft material to anchor the sensor, see Figure 64.

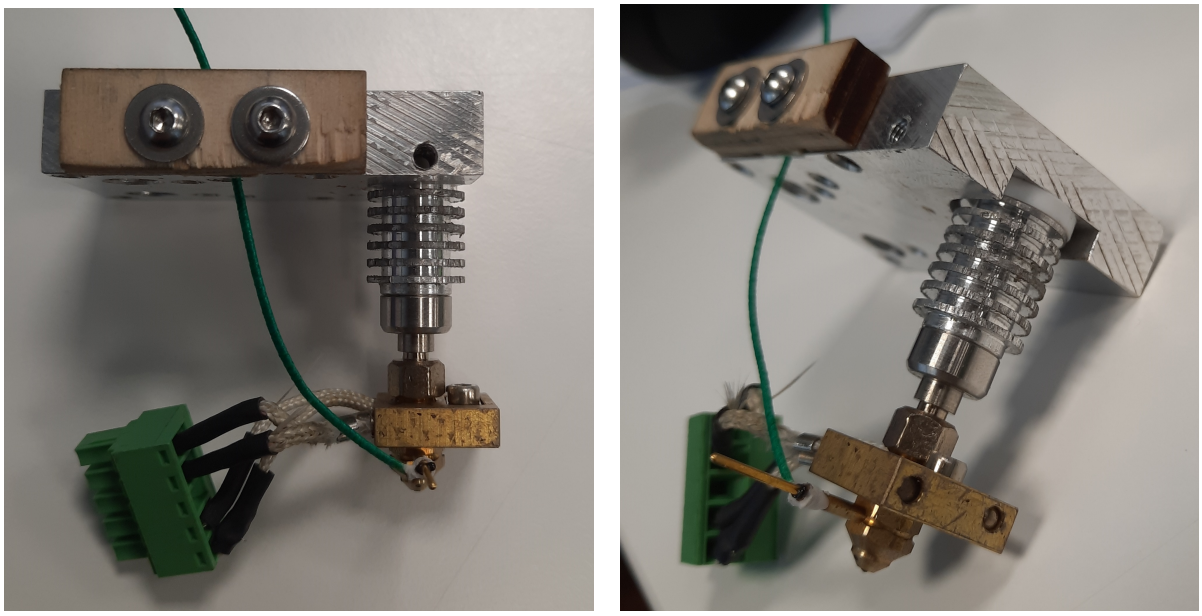

(a) Front view

(b) Trimetric view

Figure 64: A thermocouple is glued to the guidance tube. Its wire is clamped to the aluminum bracket.

A PT100 was glued into the load cell and the load cell was mounted to the aluminum bracket using a screw. Another spacer was used to offset the distance between the load cell and the nozzle, so that the pin would precisely align with the inner wall of the nozzle. This spacer also serves as a clamp for a five times folded piece of aluminum foil. The aluminum foil serves as a heat shield to minimise the load cell from heating up, see Figure 65.

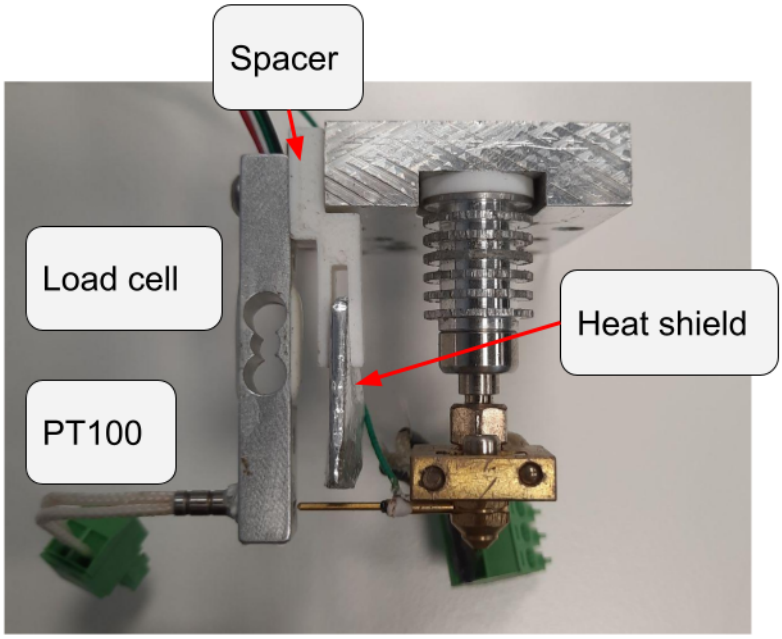


Figure 65: Front view.

Both spacers are 3D printed and allow for some compression to be more flexible in alignment. A caliper was used to measure the distance manually from the load cell to the center of the nozzle. The load cell is always mounted in the same position, whereas the pin has different heights for different nozzles. Therefore, the location at which the pin hits the load cell is different for each nozzle. A bracket was 3D printed to mount the fan to the aluminum bracket and to shield the heater block from the fan. Figure 66 is a SolidWorks sketch of this bracket. It was printed using an Ultimaker S5 in white tough PLA.

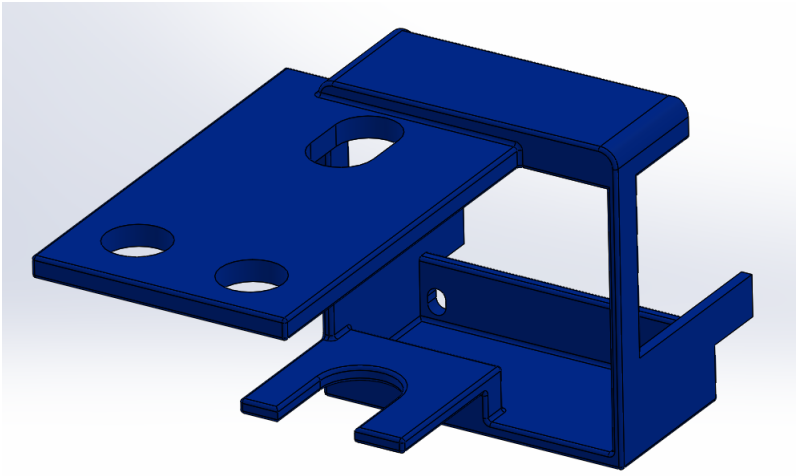

Figure 66

The bracket aims the fan at the cold end and load cell, to actively cool them. Simultaneously it shields the heater block, nozzle and pin from cold air flow caused by the fan. Figure 67 shows the assembly of the pressure monitoring set-up.

(a) Left view. (b) Front view. (c) Right view.

Figure 67: Assembly of the pressure monitoring set-up inside the nozzle.

This sub assembly was mounted to a 35kg load cell by means of a screw. Figure 68 shows the complete assembly. The rotary encoder and feeder are installed on a metal beam with bolts and nuts. The back of the cabinet has room for a spool of filament.

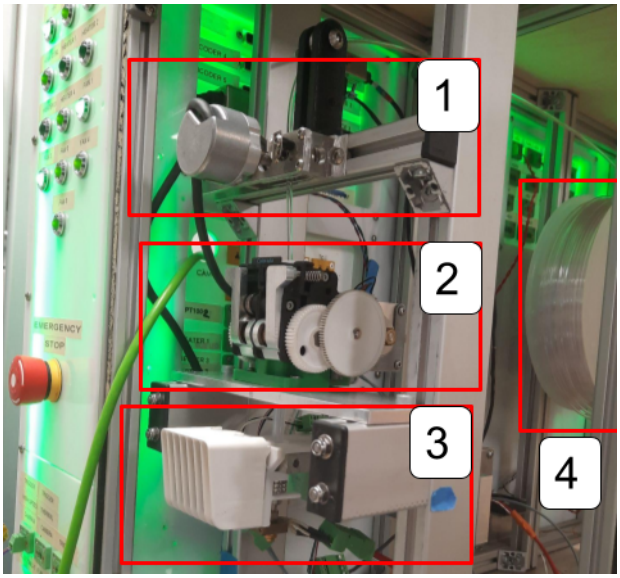


Figure 68: The complete test set-up. 1: Rotary encoder. 2: Feeder. 3: Modified nozzle assembly. 4: Filament.

## A.5 Assumptions and simplifications

Firstly, it is assumed that all the forces that are measured are due to the pressure, and that there are no other forces influencing the measurements. The area of the filament is assumed to be constant. For the extrusion force, it is clear that not all of the forces are due to pressure and that the pressures presented in the paper are too high. The pressure data for the nozzle pressure is discussed below.

The pressure monitoring set-up works under a few conditions. For example, it has been assumed that the leakage has no effect on the measurements. Appendix C.3 explains why. Additionally, it is assumed that the pin is in full contact with the melt at all times. In reality, it could be that the molten polymer does not get up to the point at which the pressure is measured. If part of the pin is in the melt, it would result in lower pressure measurements. According to another study performed by Ultimaker, the height of the melt flow is higher at lower flows and

vice versa. It implies that this phenomenon would more likely play a role at higher flows. When looking at the data, the pressure only increases at higher flows, so it is believed that melt is always high enough. Moreover, compared to the theory, the experimental data is never lower, which is another indication that this phenomenon does not happen.

In the bottom of the nozzle, the polymer is forced through the nozzle die. Not all the filament fits through and some of it crawls back up again creating vortices in the lower part of the nozzle. Figure 69 illustrates this.

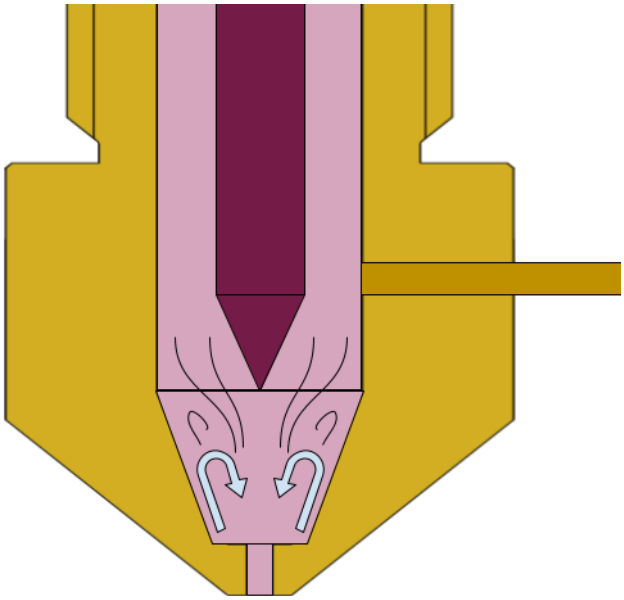

Figure 69: Vortices are created near the nozzle die.

If these vortices go as high as the pin, it can influence the readings. Moreover, the vortices will always flow from the nozzle wall towards the center, thereby decreasing the measured force. This study has not quantified the vortex behaviour. However, when comparing the experimental data to the theory, the experimental data is always higher, which implies that the vortices do not decrease the measurements. Additionally, a research partner of Ultimaker is simulating vortex behaviour. They have found that the vortices are more severe at high flows. According to their simulations, the flow has to be doubled before the vortices reach the location of the pin. Therefore, it is assumed that the vortices do not impact the measurements. However, if this set-up is to be used for higher flow measurements, it could be that the influence of vortices has to be taken in to account.
The load cell only behaves linearly at temperatures below 40 °C. A heat shield was placed between the nozzle and the load cell to prevent the load cell from reaching that temperature through convection, as discussed in Appendix A.4. Additionally, the pin was rounded at the end to prevent heat conduction through the pin. The PT100 attached to the load cell has recorded a maximum temperature of 29.8 °C, and was generally around 25 °C. Therefore, the non-linearity range of the load cell was not reached.
The limit of the pressure monitoring set-up has not been reached during the experiments. There have been no recordings of excessive leakage, damage, too high temperatures or too high forces. In an experiment with Nylon, the force limit of the load cell was almost reached. However, the feeder failed due to the high forces before the limit of the sensor was reached. Therefore, the set-up is robust in the sense that it can handle all the flows and temperatures of this study. However, a few pins and nozzles were damaged during assembly, due to its delicate design. In other words, the set-up is fragile during assembly, but robust once installed.

# B Theory

## B.1 Power law model

In the case of a Newtonian fluid, the shear stress $\tau$ is proportional to the shear rate $\dot{\gamma}$:

$$\tau = \eta * \dot{\gamma} \tag{10}$$

where $\eta$ is the constant proportional viscosity of the fluid, which is a measure of the internal resistance to flow under shear. In pseudoplastic polymers, such as the materials used in this study, the viscosity $\eta$ is not constant, but dependent on the shear rate $\dot{\gamma}$. In a log-log graph, with shear rate on the x-axis and viscosity on the y-axis, the viscosity of a Newtonian fluid would be a straight line, whereas the viscosity of pseudoplastic fluids would decrease as a function of shear rate. The Power Law of Ostwald and deWaele is the most widely used model for describing the non-Newtonian slope in the viscosity curve of pseudoplastics [35]. It relates the shear stress and the shear rate of the fluid through its material properties:

$$\dot{\gamma} = \phi * \tau^m \tag{11}$$

where $\dot{\gamma}$ is shear rate, $\tau$ is the shear stress, $\phi$ is the fluidity of the material and $m$ is the flow exponent of the material. Figure 70 illustrates the viscosity curve of a pseudplastic; PLA in this case. At low shear rates it behaves as a Newtonian fluid. With increasing shear rates, the viscosity drops. The power law approximates the slope of this non-Newtonian behaviour.

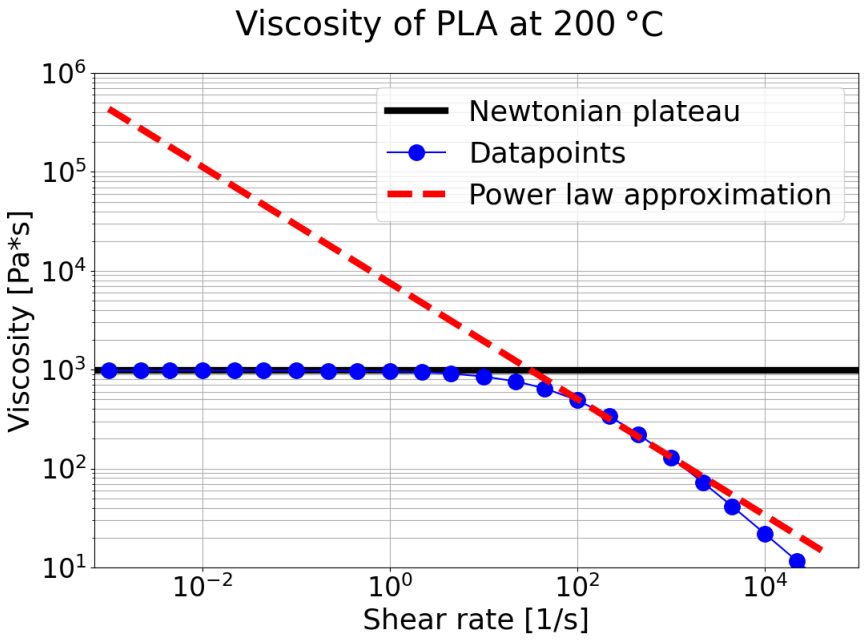


Figure 70: The power law approaches the non-Newtonian slope of the viscosity curve.

The flow exponent $m$ describes the ability of a material to flow and its deviation from the Newtonian behaviour [35] and is expressed as

$$m = \frac{\Delta log(\dot{\gamma})}{\Delta log(\tau)}. \tag{12}$$

In the viscosity curve, $m$ is the slope of the non-Newtonian region. For Newtonian fluids, $m = 1$ and $\phi = \frac{1}{\eta}$. For pseudoplastic fluids, $m > 1$. By rearranging Equation 11 for $\tau$, we get

$$\tau = \left(\frac{\dot{\gamma}}{\phi}\right)^{\frac{1}{m}} \tag{13}$$

which is implemented in the Cauchy momentum equation, as is described in Appendix B.2. This study uses the Python function curve_fit to find the best approximation of the non-Newtonian slope in the viscosity graph. It uses non-linear least square fitting of the data to find optimal parameters for $m$ and $\phi$ so that the sum of the squared residuals is minimised. A difficulty with this approach is defining the distinction between the Newtonian plateau and the non-Newtonian slope. It is a gradual transition from Newtonian plateau to non-Newtonian behaviour, rather than an abrupt set point. In this study, the data points that were included in the curve_fit function were manually selected for each material. Appendix E.1 shows the viscosity curves for each material. They include the manually selected set point that defines the start of the non-Newtonian slope of the curve. The values of $m$ and $\phi$ are listed in Table 5.

| Material | $m$ (-) | $\phi$ $(1/\eta)$ |
|---|---|---|
| PLA | 2.42 | 4.09E-10 |
| PETG | 1.28 | 1.79E-4 |
| PC | 4.13 | 1.62E-15 |
| Nylon | 15.04 | 1.19E-53 |

Table 5

According to Michaeli [35], the values of $m$ for polymeric melts lie between 1 and 6. In this study, the value $m$ for PLA, PETG and PC lie within that range. However, Nylon has a flow exponent $m$ of 15.04. This could indicate that the viscosity curve for Nylon is incorrectly measured, or that the approach of the Power Law does not fit well with Nylon. The high value for $m$ explains why the theoretical pressure drop for Nylon is very low.

## B.2 Pressure calculations

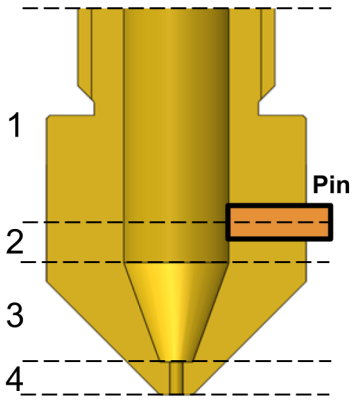


Figure 71: A nozzle divided into four sections. The rectangle on the right illustrates the position of the pin.

Section 1 ranges from the top of the nozzle to the center of the pressure monitoring pin. Section 2 ranges from the center of the pin to the start of the conical shape within the nozzle. Section 3 is the conically shaped part of the nozzle and section 4 is the nozzle die.

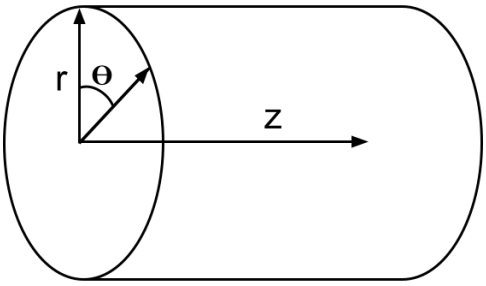


Figure 72

The Cauchy momentum equation was used to find the flow speed equation through a cylindrical tube. In cylindrical coordinates, for a flow in the direction of z, as shown in Figure 72, the equation holds:

$$\rho\left(\frac{\partial u_z}{\partial t}+u_r\frac{\partial u_z}{\partial r}+\frac{u_\theta}{r}\frac{\partial u_z}{\partial \theta}+u_z\frac{\partial u_z}{\partial z}\right)=-\frac{\partial P}{\partial z}-\frac{\partial \tau_{zz}}{\partial z}-\frac{1}{r}\frac{\partial \tau_{\theta z}}{\partial \theta}-\frac{1}{r}\frac{\partial (r\tau_{rz})}{\partial r}+\rho g_z. \tag{14}$$

Which states that there must be a conservation of momentum in the flow throughout the cylinder. To simplify the equation, a few assumptions are made. $\frac{\partial u_z}{\partial t}=0$ because the flow is assumed to have a constant speed. The flow is also assumed to be purely in the direction of z, which means that $u_r\frac{\partial u_z}{\partial r}=0$ and $\frac{u_\theta}{r}\frac{\partial u_z}{\partial \theta}=0$. By assuming a constant pressure gradient in the channel cross-section, the effects of normal stress can be omitted, which means that $\frac{\partial \tau_{zz}}{\partial z}=0$. Rotational symmetry throughout the cylinder yields that $\frac{1}{r}\frac{\partial \tau_{\theta z}}{\partial \theta}=0$. Gravitational forces are negligible compared to frictional forces and pressure, so $\rho g_z=0$ is assumed. These assumptions simplify Equation 14 into:

$$\rho\left(u_z\frac{\partial u_z}{\partial z}\right)=-\frac{\partial P}{\partial z}-\frac{1}{r}\frac{\partial (r\tau_{rz})}{\partial r}. \tag{15}$$

The continuity equation states that there must be a conservation of mass. In cylindrical coordinates this equation states:

$$\frac{\partial \rho}{\partial t}+\frac{1}{r}\frac{\partial}{\partial r}(r\rho u_r)+\frac{1}{r}\frac{\partial}{\partial \theta}(\rho u_\theta)+\frac{\partial}{\partial z}(\rho u_z)=0. \tag{16}$$

The melt is assumed to be incompressible, so the density is constant resulting in $\frac{\partial \rho}{\partial t}=0$. The speed is considered to be purely in z direction, so $\frac{1}{r}\frac{\partial}{\partial r}(r\rho u_r)=0$ and $\frac{1}{r}\frac{\partial}{\partial \theta}(\rho u_\theta)=0$. Therefore, $\frac{\partial}{\partial z}(\rho u_z)=0$, in other words $\frac{\partial \rho}{\partial z}*u_z+\frac{\partial u_z}{\partial z}*\rho=0$. Since the density is constant, $\frac{\partial \rho}{\partial z}*u_z=0$ and therefore $\frac{\partial u_z}{\partial z}*\rho=0$. Putting this result into equation 15 results in:

$$0=-\frac{\partial P}{\partial z}-\frac{1}{r}\frac{\partial (r\tau_{rz})}{\partial r}. \tag{17}$$

After rearranging and integrating over r this becomes

$$\int \frac{\partial}{\partial r}(r\tau_{rz}) \ = \int \frac{\partial P}{\partial z} * r \tag{18}$$

leading to

$$r\tau_{rz} = \frac{r^2}{2}\frac{\partial P}{\partial z} + C_1 \tag{19}$$

The stress in the flow at the middle of the cylinder is equal to zero. Therefore at $r = 0$, $\tau_{rz} = 0$ which results in $C_1 = 0$. Inserting and rearranging gives

$$\tau_{rz} = \frac{r}{2}\frac{\partial P}{\partial z} \tag{20}$$

According to the power law

$$\tau_{rz} = \left(\frac{\dot{\gamma}}{\phi}\right)^{\left(\frac{1}{m}\right)} \tag{21}$$

where the viscosity $\dot{\gamma}$ is $\frac{\partial u}{\partial r}$. Implementing the power law into Equation 21 results in

$$\frac{\partial u}{\partial r} = \frac{\phi}{2^m}\left(\frac{\partial P}{\partial z}\right)^m r^m \tag{22}$$

and after integration

$$u = \frac{\phi}{2^m}\left(\frac{\partial P}{\partial z}\right)^m \frac{r^{m+1}}{m+1} + C_2. \tag{23}$$

At the wall, the speed of the flow is zero: $u(r = R) = 0$. This means that

$$\frac{\phi}{2^m}\left(\frac{\partial P}{\partial z}\right)^m \frac{R^{m+1}}{m+1} + C_2 = 0 \tag{24}$$

which means that

$$C_2 = -\frac{\phi}{2^m}\left(\frac{\partial P}{\partial z}\right)^m \frac{R^{m+1}}{m+1} \tag{25}$$

Therefore, the general equation of the flow speed in the cross section of a channel with radius R is

$$u(r) = \frac{\phi}{2^m}\left(\frac{\partial P}{\partial z}\right)^m \frac{r^{m+1} - R^{m+1}}{m+1} \tag{26}$$

The average flow at a point in the cylinder can be computed by taking the double integral over the speed profile from Equation 26, and dividing by the initial area (with radius $R_n$) of the cylinder:

$$\overline{u} = \frac{1}{\pi R_n^2}\iint u(r)\, dr\, d\theta \tag{27}$$

The following paragraphs show the pressure drop calculations over each of the sections described in Figure 71.

### *B.2.1 Section 1*

Section 1 can be seen as a cylinder with radius $R_n$ and length $L_1$, as shown in Figure 73.

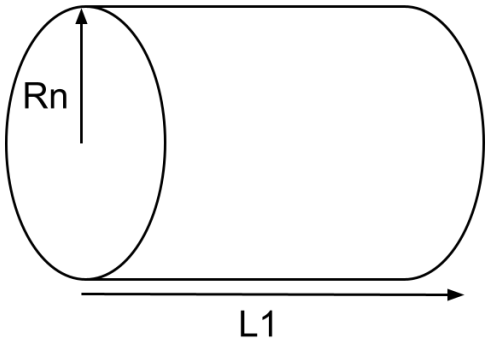


Figure 73: Section 1 of the nozzle is approached as a cylinder with radius $R_n$ and length $L_1$.

The average velocity of the flow in the cross section of this cylinder, according to Equation 27, is

$$\overline{u} = \frac{1}{\pi R_n^2} \int_0^{R_n} 2\pi r * u_{R_n}(r)\, dr. \tag{28}$$

Inserting Equation 26 gives

$$\overline{u} = \frac{2}{R_n^2} \int_0^{R_n} r \left( \frac{\phi}{2^m} \left( \frac{\partial P}{\partial z} \right)^m \right) \frac{r^{m+1} - R_n^{m+1}}{m+1}\, dr \tag{29}$$

equals

$$\overline{u} = A * \int_0^{R_n} r \left( r^{m+1} - R_n^{m+1} \right)\, dr \tag{30}$$

where

$$A = \frac{\phi}{2^m} \left( \frac{\partial P}{\partial z} \right)^m \frac{2}{R_n^2 (m+1)}. \tag{31}$$

This results in

$$\overline{u} = A * \left( \int_0^{R_n} r^{m+2}\, dr - \int_0^{R_n} r R_n^{m+1}\, dr \right) \tag{32}$$

equals

$$A * \left[ \frac{r^{m+3}}{m+3} \Big|_0^{R_n} - R_n^{m+1} * \frac{r^2}{2} \Big|_0^{R_n} \right] = A * \left[ \frac{R_n^{m+3}}{m+3} - R_n^{m+1} * \frac{R_n^2}{2} \right] \tag{33}$$

equals

$$\overline{u} = -\phi \left( \frac{\partial P}{\partial z} \right)^m * \frac{R_n^{m+1}}{2^m (m+3)}. \tag{34}$$

Rearranging and integrating over the length $L_1$ results in the pressure drop equation for section 1:

$$\Delta P_1 = 2 * L_1 * \left( \frac{v}{\phi} \right)^{\frac{1}{m}} * \left( \frac{m+3}{\left(\frac{D_n}{2}\right)^{m+1}} \right)^{\frac{1}{m}} \tag{35}$$

where $v$ is the same as the average velocity $\overline{u}$ and $\frac{D_n}{2}$ is the same as the radius $R_n$.

### *B.2.2 Section 2*

Section 2 can be approached as a cylinder with radius $R_n$ and length $L_2$. Therefore, the same steps have been taken as in Section 1, but instead Equation 34 has been rearranged and integrated over the length $L_2$ leading to

$$\Delta P_2 = 2 * L_2 * \left( \frac{v}{\phi} \right)^{\frac{1}{m}} * \left( \frac{m+3}{\left(\frac{D_n}{2}\right)^{m+1}} \right)^{\frac{1}{m}}. \tag{36}$$

### *B.2.3 Section 3*

Section 3 can be seen as a cone with radius $R_n$ which linearly decreases to radius $R_p$ under an angle $\alpha$, with a length $L$. It is approached as a sequence of infinitesimal small circular pipes.

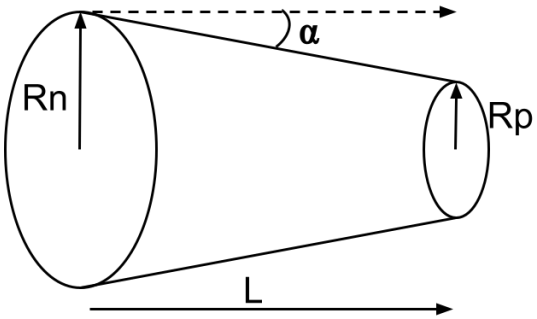


Figure 74: Section 3 of the nozzle is approached as a cone with radius $R_n$ which linearly decreases to radius $R_p$ under an angle $\alpha$, with length $L$.

Using Equations 26 and 27 with these variables results in

$$\overline{u} = \frac{2}{R_n^2} \int_0^{R_d} r \left( \frac{\phi}{2^m} \left( \frac{\partial P}{\partial z} \right)^m \right) \frac{r^{m+1} - R^{m+1}}{m+1} \, dr \tag{37}$$

Where $R$ is a function of z according to

$$R = R_n - \tan\alpha * z. \tag{38}$$

Solving this equation yields

$$\overline{u} = -\phi \left(\frac{\partial P}{\partial z}\right)^m * \frac{R^{m+3}}{R_n^2} \frac{1}{2^m * (m+3)}. \tag{39}$$

Rearranging gives

$$\Delta P = B \int_0^L (C * z * R_n)^{\frac{-m-3}{m}}\, dz \tag{40}$$

with

$$B = \left(\frac{\overline{u} * R_n^2 * 2^m * (m+3)}{\phi}\right)^{\left(\frac{1}{m}\right)} \tag{41}$$

and

$$C = \frac{R_n - R_p}{L} \tag{42}$$

$$L = \frac{R_n - R_p}{\tan\alpha}. \tag{43}$$

Integration results in

$$\Delta P = -\frac{B * m}{3 * C} * \left((C * L + R_n)^{\frac{-3}{m}} - R_n^{\frac{-3}{m}}\right). \tag{44}$$

Implementing and simplifying results in the pressure drop over section 3:

$$\begin{aligned} \Delta P_3 = &\left(\frac{2 * m}{3 * \tan\alpha}\right) * \left(\frac{1}{D_p^{\frac{3}{m}}} - \frac{1}{D_n^{\frac{3}{m}}}\right) * \\ &\left(\left(\frac{D_n}{2}\right)^2 * (m+3) * 2^{m+3}\right)^{\frac{1}{m}} * \left(\frac{v}{\phi}\right)^{\frac{1}{m}} \end{aligned} \tag{45}$$

where $v$ is the same as $\overline{u}$, $D_p$ is the same as $2 * R_p$ and $D_n$ is the same as $2 * R_n$. Compared to the pressure drop over this section as proposed by Bellini et al. [19], the term $\left(\frac{v}{\phi}\right)^{\frac{1}{m}}$ is now included in the equation.

### *B.2.4 Section 4*

Section 4 can be seen as a cylinder with radius $R_d$ and length $L_d$, as shown in Figure 75.

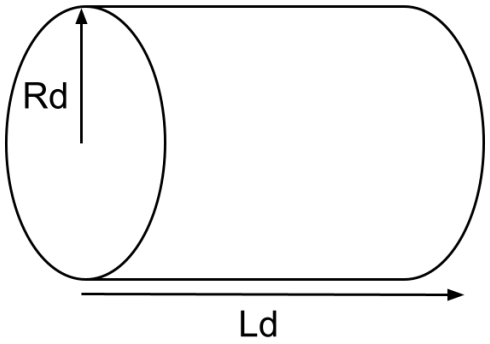


Figure 75: Section 4 of the nozzle is approached as a cylinder with radius $R_d$ and length $L_d$.

Using Equations 26 and 27 with these variables results in

$$\overline{u} = \frac{2}{R_n^2} \int_0^{R_d} r \left( \frac{\phi}{2^m} \left( \frac{\partial P}{\partial z} \right)^m \right) \frac{r^{m+1} - R_d^{m+1}}{m+1} \, dr. \tag{46}$$

Solving this integral results in

$$\overline{u} = -\phi \left( \frac{\partial P}{\partial z} \right)^m * \frac{R_d^{m+3}}{R_n^2} \frac{1}{2^m * (m+3)}. \tag{47}$$

Rearranging and integrating over the length $L_d$ results in the pressure drop equation for section 4:

$$\Delta P_4 = 2 * L_d * \left( \frac{v}{\phi} \right)^{\frac{1}{m}} * \left( \frac{(m+3) * \left( \frac{D_n}{2} \right)^2}{\left( \frac{D_d}{2} \right)^{m+3}} \right)^{\frac{1}{m}} \tag{48}$$

where v is the average velocity $\overline{u}$, $\frac{D_n}{2}$ is the same as $R_n$ and $\frac{D_d}{2}$ is the same as $R_d$.

# C Peripherals

## C.1 Error propagation

The average pressure was calculated at different flows and temperatures. For each average pressure that was calculated, the error of the pressure was calculated according to

$$\sigma_P = P * \sqrt{(\frac{\sigma_F}{F})^2 + (\frac{\sigma_A}{A})^2} \tag{49}$$

where $P$ is the pressure, $\sigma_P$ is the error of the pressure, $F$ is the average force, $\sigma_F$ is the error of the force, $A$ is the area and $\sigma_A$ is the error of the area. The error of the force $\sigma_F$ is the standard deviation of all the data points in the test, calculated using

$$\sigma_F = \sqrt{\frac{\sum_{i=1}^{N} |f_i - \mu_f|^2}{N}} \tag{50}$$

where N is the total number of data points in the tests at the corresponding flow and temperature, $f$ is the data point of a single force measurement and $\mu_f$ is the mean of the data points. The error on the area of the pin is computed by means of error propagation of the diameter of the pin according to

$$\sigma_{A_p} = A_p * \sqrt{\left(\frac{\sigma_d}{d}\right)^2 * 2} \tag{51}$$

where $d$ is the diameter of the pin and $\sigma_d$ is the standard deviation of the diameter of the pin. The standard deviation of the diameter of the pin was calculated using

$$\sigma_d = \sqrt{\frac{\sum_{i=1}^{N} |d_i - \mu_d|^2}{N}} \tag{52}$$

which is similar to Equation 50. The mean diameter of the pin was obtained by three microscopical images, as further explained in Appendix C.2. The error on the area of the filament is calculated using

$$\sigma_{A_f} = A_f * \sqrt{\left(\frac{\sigma_D}{D}\right)^2 * 2} \tag{53}$$

where $D$ is the diameter of the filament and $\sigma_D$ is the error of the diameter of the filament. These values are taken from the data sheets of the corresponding material. The error of the flow is the standard deviation of the different flows in repeating tests according to

$$\sigma_{fl} = \sqrt{\frac{\sum_{i=1}^{N} |fl_i - \mu_{fl}|^2}{N}}. \tag{54}$$

## C.2 Microscope

Prior to testing, the modified nozzle and the pin were placed under a Leica DVM6 Digital Microscope. The diameters of the pin, the guidance tube and the nozzle die were measured using the microscope. Additionally, the equipment was checked for damage and inconsistencies. This paragraph shows some example images of one combination of nozzle and pin. Figure 76 shows a closeup image of the front of the pin. The Leica software allows for the detection of the diameter by manually drawing a circle within the image.

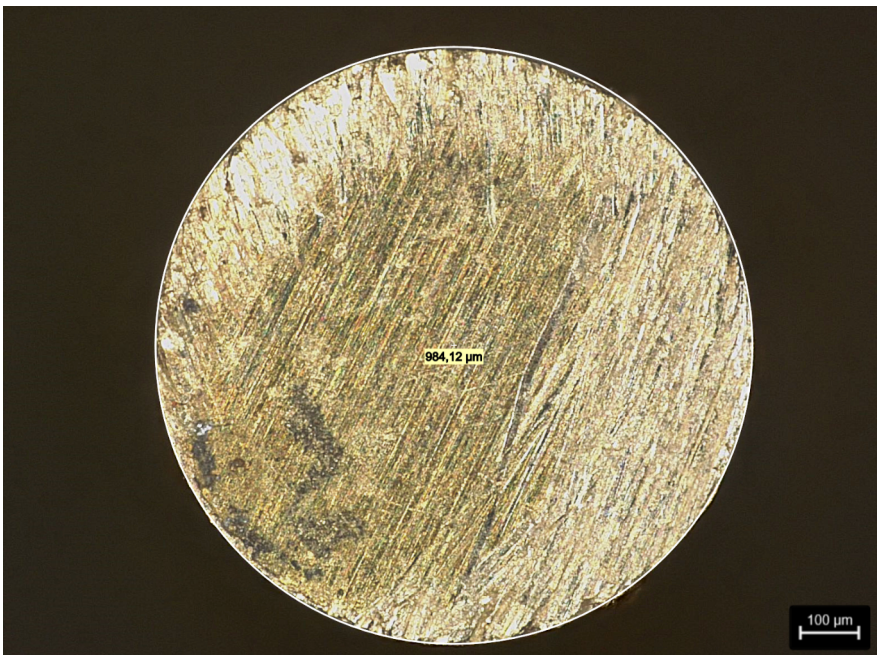


Figure 76: Example image of the frontal area of the pin. A circle has been drawn to capture the diameter using the software provided by the digital microscope.

For each different pin, three different images of the frontal surface have been taken. The average diameter of the three images was used to calculate the frontal area and the pressure inside the nozzle. The error of the three images was propagated, as explained in Appendix C.1. Additionally, the average value was used in the friction calculation, as explained in Appendix C.3. The diameter of the tube is also used for the friction force calculation. Similarly, three values from three images were averaged. Figure 77 shows an example.

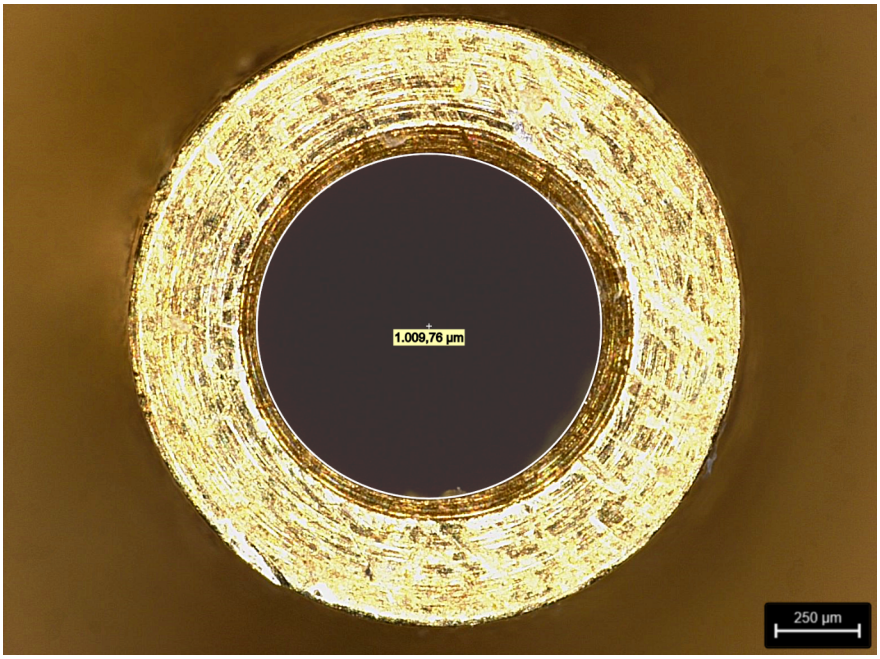


Figure 77: Example image of the opening of the guidance tube. A circle has been drawn to capture the diameter using the software provided by the digital microscope.

For the theoretical pressure calculations, the nozzle die diameter is used. The diameter was also found by averaging the diameter of three images. An example is shown in Figure 78.

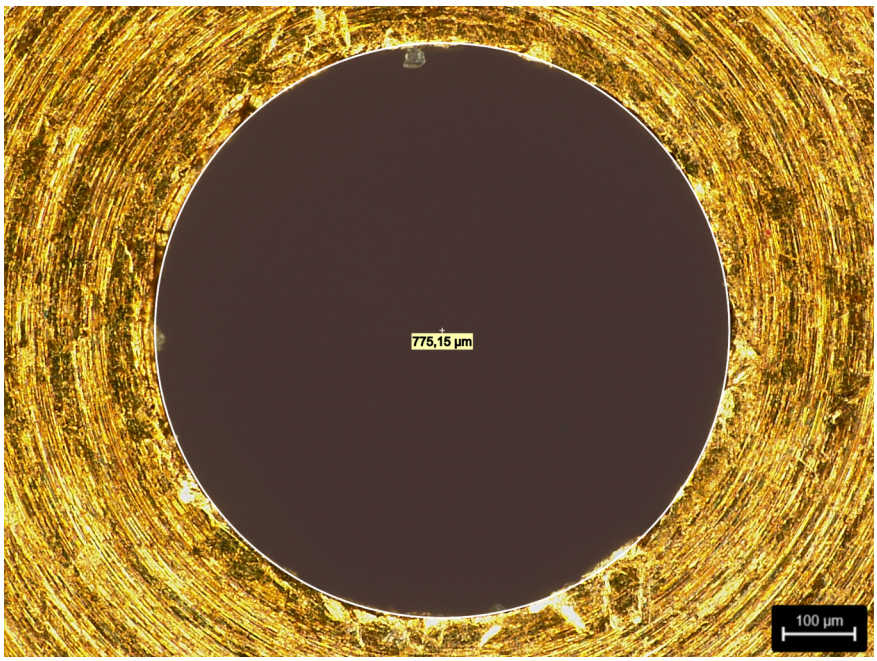


Figure 78: Example image of the nozzle die. A circle has been drawn to capture the diameter using the software provided by the digital microscope.

Another image was also taken from the nozzle die, but then seen from the top. This was done to see possible inconsistencies such as scratch marks. Figure 79 shows an example. None of the modified nozzles showed inconsistencies so severe that they would be rejected.

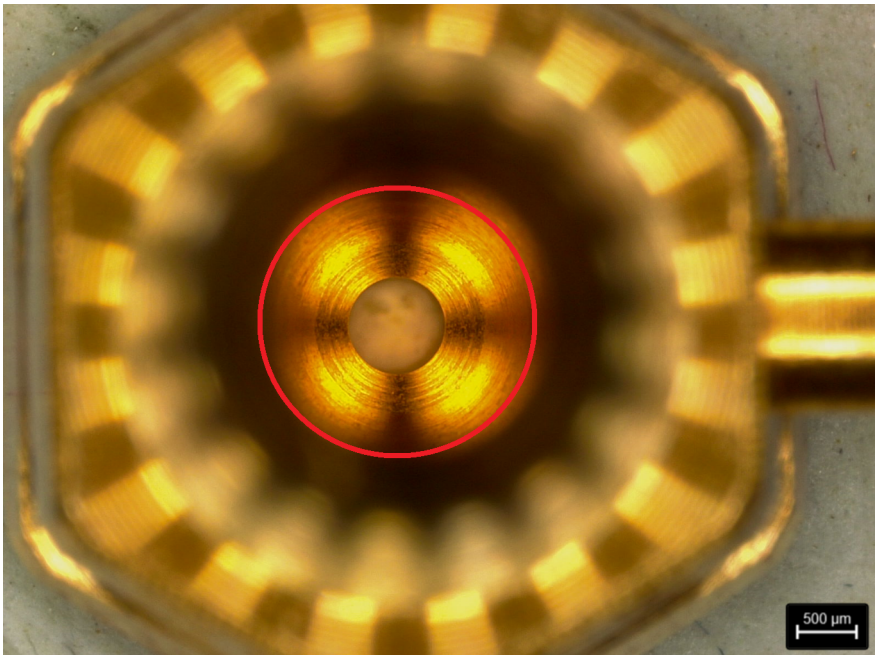


Figure 79: Example image of the nozzle die as seen from above. This image shows no scratch marks or other damage.

The alignment of the guidance tube that was press-fit into the nozzle was also checked using the microscope. Figure 80 shown an example. Generally, the alignment was very accurate.

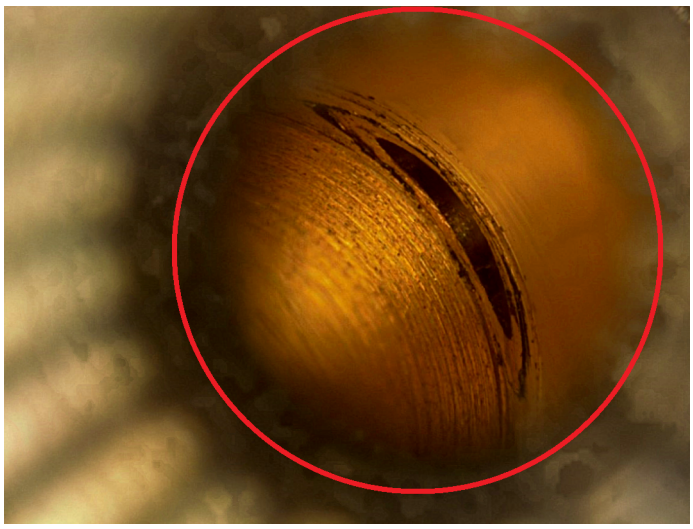

Figure 80: Example image of the alignment of the guidance tube that was press-fit into the nozzle.

## C.3 Leakage

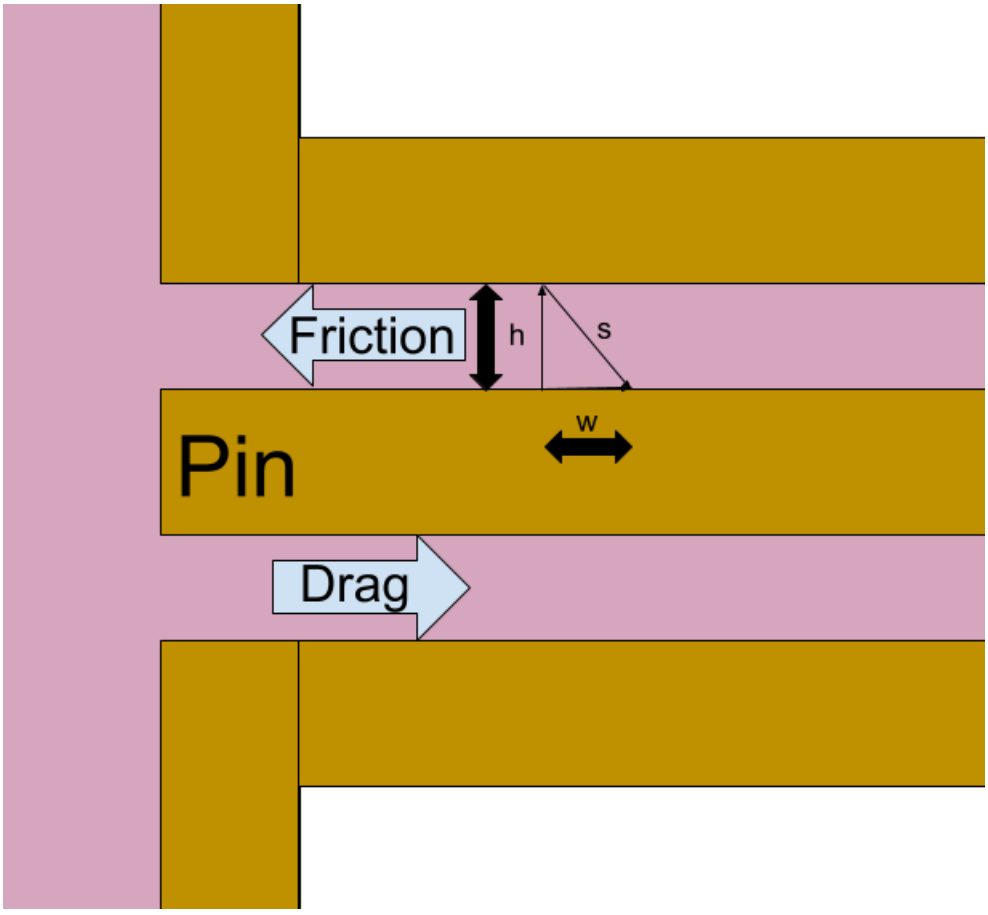


Figure 81: Melt in between the pin and guidance tube can have an effect on the measurements. The melt can drag the pin out increasing the measurements, or it can cause friction which decreases the measurements.

The flow of melt leaking out can drag the pin outwards resulting in higher force measurements. However, the flow of melt was low. Figure 82 shows the leakage recorded after 6.5 hours of extrusion. An approximation of the leakage based on this image results in a volumetric leakage

of $\pm$ 1 mm$^3$. As a comparison, when extruding at an average speed of 4 mm$^3/s$ for 6.5 hours, a total volume of 93,600 mm$^3$ is extruded. The flow of melt leaking out is 0.001%. Therefore, the drag force is considered negligible.

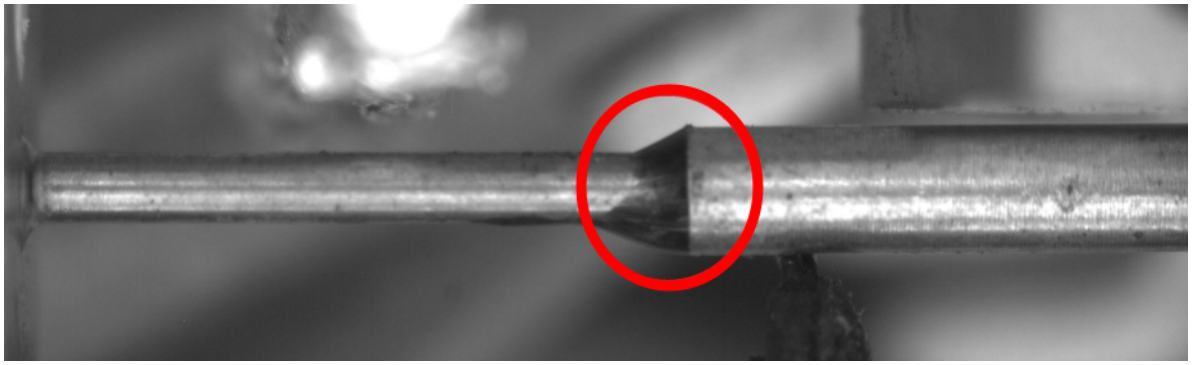

Figure 82: Leakage between guidance tube and pin. This image was taken after 6.5 hours of extrusion.

The polymer can also decrease the measurements due to friction. The friction force is approximated using the following equations:

$$F_{fr} = \sigma * A_L \tag{55a}$$

$$\sigma = G' * \epsilon \tag{55b}$$

$$\epsilon = \frac{w}{h} \tag{55c}$$

where $F_{fr}$ is the friction force, $\sigma$ is the stress within the leaking polymer, $A_L$ is the lateral area of the pin inside the tube, $G'$ is the elastic modulus of the leaking polymer, $\epsilon$ is the strain of the leaking polymer, $w$ is the horizontal displacement of the pin and $h$ is the distance between the pin and the guidance tube. The horizontal displacement $w$ depends on the pressure and is taken from the load cell calibrations values, see Appendix A.3. The distance between the guidance tube and the pin $h$ has been calculated according to

$$h = \frac{D_h - d_h}{2} \tag{56}$$

where $D_h$ is the hot (temperature at extrusion) inner diameter of the guidance tube and $d_h$ is the hot diameter of the pin. Thermal expansion has been accounted for by using

$$D_h = D_c * (1 + \Delta T * \alpha_T) \tag{57}$$

and

$$d_h = d_c * (1 + \Delta T * \alpha_T) \tag{58}$$

where $D_c$ and $d_c$ are the cold (room temperature, 20 °C) diameters of the guidance tube and pin, respectively. These values are different for each nozzle and pin, and have been obtained with the help of microscopical imaging, see Appendix C.2. $\Delta T$ is the temperature difference between room temperature (at which the microscope images have been taken) and the temperature that the thermocouple recorded during extrusion, see Figure 83. The thermal expansion coefficient $\alpha_T$ is the same for the pin and the guidance tube because they are made from the same material; CuZn39Pb3. Its value is 0.0000214 K$^{-1}$.

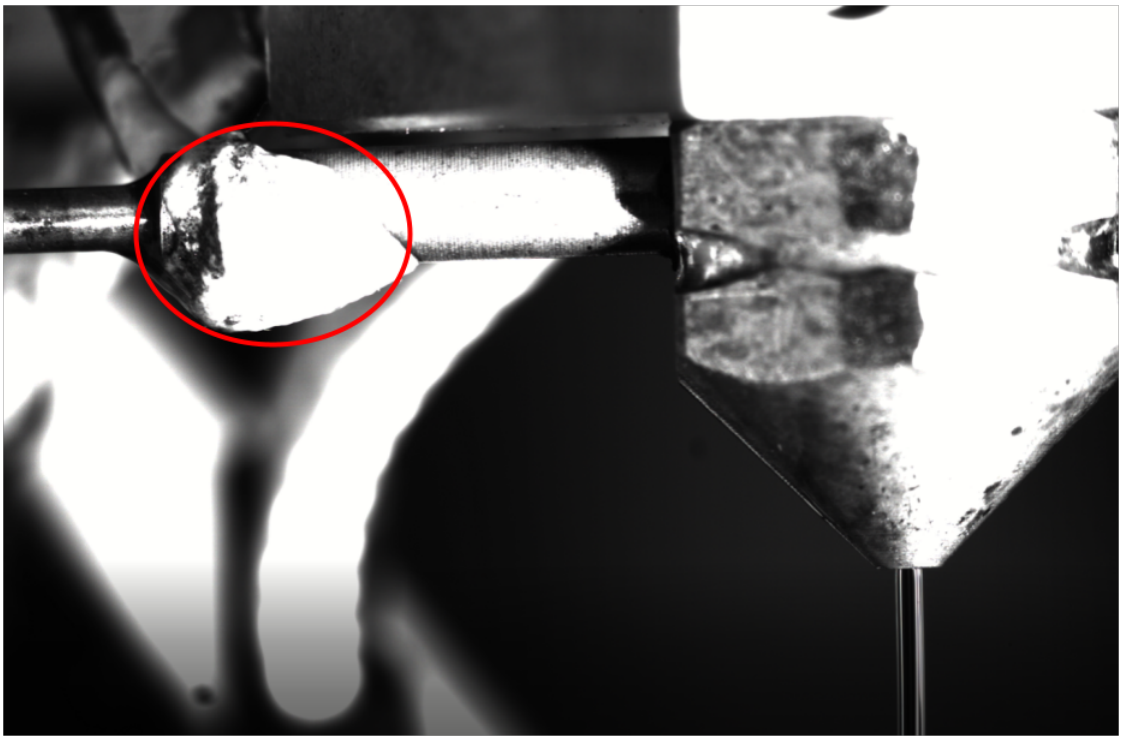

Figure 83: Image of the nozzle, guidance tube, pin and thermocouple during extrusion. The white blob on the guidance tube is thermal conducting glue that covers the thermocouple.

The value from the thermocouple has been assumed to be the same temperature as the melt within the guidance tube, the guidance tube and the pin. The elastic modulus ($G'$) for PLA depends on the temperature and on the shear strain of the melt. Figure 84 shows a graph of the elastic modulus versus strain at a temperature of 160 $°C$. The black curve is for PLA. On the x-axis, the strain is defined as the slope between $w$ and $h$ in percentage; if $w = h$, the slope is 100%. Data of the elastic modulus versus strain for the exact polymer in this study is not available. There are only a few graphs available in literature and elastic modulii can vary slightly between different PLA blends. Additionally, this graph is at a melt temperature of 160 °C, whereas the lowest measured temperature in the experiments with PLA was 167 °C, ranging up to 185 °C. As stated before, the guidance tube temperature is at its lowest at the point at which it is measured. Lower temperatures of the melt increase the elastic modulus. Therefore, the calculated friction forces based on this graph are higher than in reality, to determine the worst case scenario.

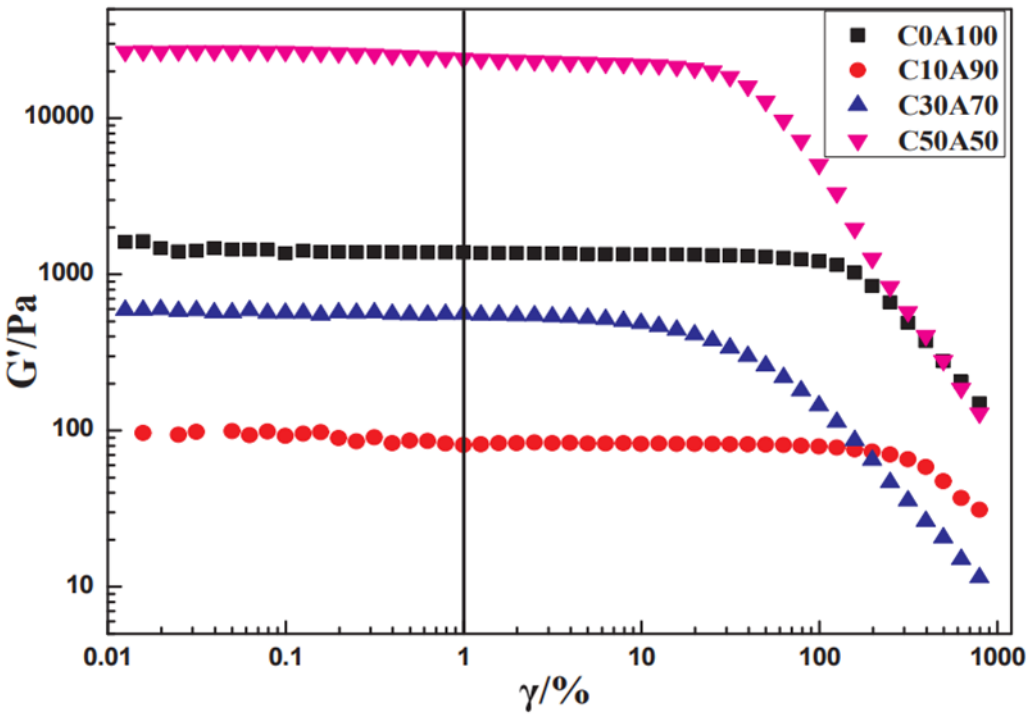


Figure 84: Elastic modulus versus strain. The black curve (C0A100) is for PLA. Image from [37]

In other words, the friction forces calculated with this theory are an approximation of the real friction forces, to determine their order of magnitude. Based on these calculations, the friction forces lie between 0% and 5%. With most flow and temperature combinations the friction forces are approximately 2%. Because the friction forces are variable estimations that are mostly in the order of magnitude of 2%, their influence has been neglected. Moreover, in practice, the nozzle force returned to zero after every experiment. Because the friction would also work in opposite direction when the pin moves inward again, this confirms that friction forces play a minor role.

An example calculation is given below, it is from a type 2 nozzle, with a temperature of 205 °C and a flow of 3 $mm^3/s$. The microscopic values for $D_c$ are 1008.94 $\mu$m, 1007.09 $\mu$m and 1006.02 $\mu$m resulting in an average of 1007 $\mu$m. The microscopic values for $d_c$ are 978.87 $\mu$m, 980.54 $\mu$m and 979.66 $\mu$m resulting in an average of 980 $\mu$m. The average recorded temperature at the end of the guidance tube is 176.5 °C, which means that $\Delta$T is 156.5 °C. Equations 56, 57 and 58 give $h = 13.5$ mm. With an average nozzle force of 1.7 N, the horizontal displacement is approximately 15 $\mu$m resulting in a strain of 111%. Reading from the graph yields an elastic modulus of about 1000 Pa. With a lateral area of $2.47 * 10^{-5}$ m (the pin sticks 8 mm into the guidance tube), Equations 55 results in a friction force of 0.27 N, which is approximately 1.6% of the nozzle force. As stated before, the estimation of the elastic modulus assumes a melt temperature of 160 °C throughout the entire guidance tube. In reality, the temperature in the guidance tube is a gradient between 176 °C and 205 °C, which would result in a much lower elastic modulus, and therefore a much lower friction force.

# D Subsequent Research

## D.1 Comparison to enhanced theory

The theoretical pressure calculations used in this study are relatively simple. Due to the limited time of the project and the resources available, it was chosen to use this theory over more complex theory. Nonetheless, keeping in mind the simplifications and assumptions of the used theory, the experimental is in line with the theory. It would be very interesting to compare the experimental data with more advanced theory. For example models that include more phenomena such as elastic behaviour, temperature non-uniformity, backflow of the melt and more accurate viscosity models. It would be interesting to see the similarities and deviations between the experimental data from this study and the theoretical pressure from more advanced models to shine light on the impact of other phenomena on the pressure drop in the nozzle of a fused filament fabrication 3D printer.

## D.2 Dynamic measurements

All the experiments performed in this study are steady-state experiments. Even in steady-state, the pressure is fluctuating. According to Serdeczny et al. [18], that is because the backflow functions as a heat conductor between the nozzle wall and the solid filament which increases the heat transfer rate. As a result, the temperature increases, the viscosity decreases and the pressure drops. The pressure drop causes the backflow to sink. Therefore, the heat transfer rate reduces, the temperature reduces and the viscosity of the melt increases. Consequently, the pressure increases, resulting in a higher backflow which causes the cycle to repeat itself. This study omits this effect by taking the average pressure over a range of ten minutes. However, it would be interesting to do more experiments on this dynamic behaviour. Moreover, it would be interesting to test dynamic states by varying temperature and feed rates during extrusion. This could give more insights into the settling time of the polymers, the temperature influence and the history dependence of pressure. Furthermore, this experimental set-up could be used to supplement dynamic-state theoretical models.

## D.3 Printing

This study tests a nozzle that extrudes in open air. There is no print head movement and there is no back pressure from the print bed. These could influence the pressure within the nozzle and it would be interesting to test this design in an actual printer. The design proposed in this study is suitable to be implemented in the print head of an Ultimaker S5. The modified nozzle and pin fit in a standard print core (see Figure 85). A print core is basically a cartridge that can be easily swapped in Ultimaker printers.

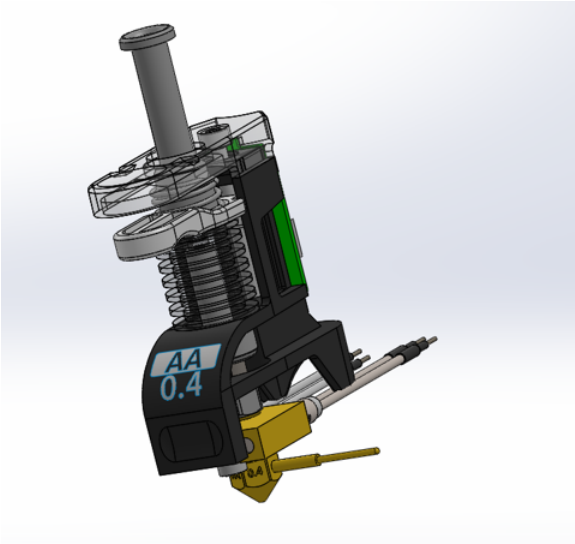


Figure 85: Modified nozzle inside a standard Ultimaker print core.

The print head of an Ultimaker S5 consists of two slots for print cores. This design uses the space of the second slot to fit the load cell using a customised mounting bracket. The mounting bracket, illustrated in blue in Figure 86, should be made of a stiff material.

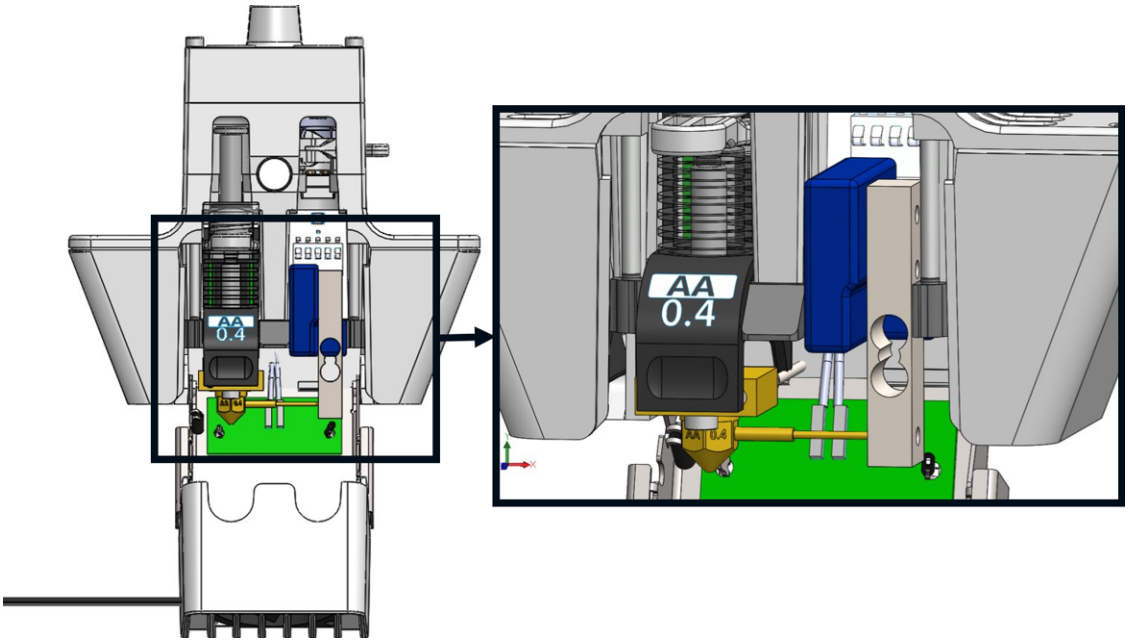


Figure 86: Sketch of dynamic printing set-up.

The same data logging module that was used in this study cannot be re-used in in-line printing, because the printer firmware/software is not compatible; a new module has to be designed. However, a simple proof-of-concept implementation has been made. The load cell was connected to an Arduino to see force fluctuations when extruding at different flows. A closeup of this test is shown in Figure 87.

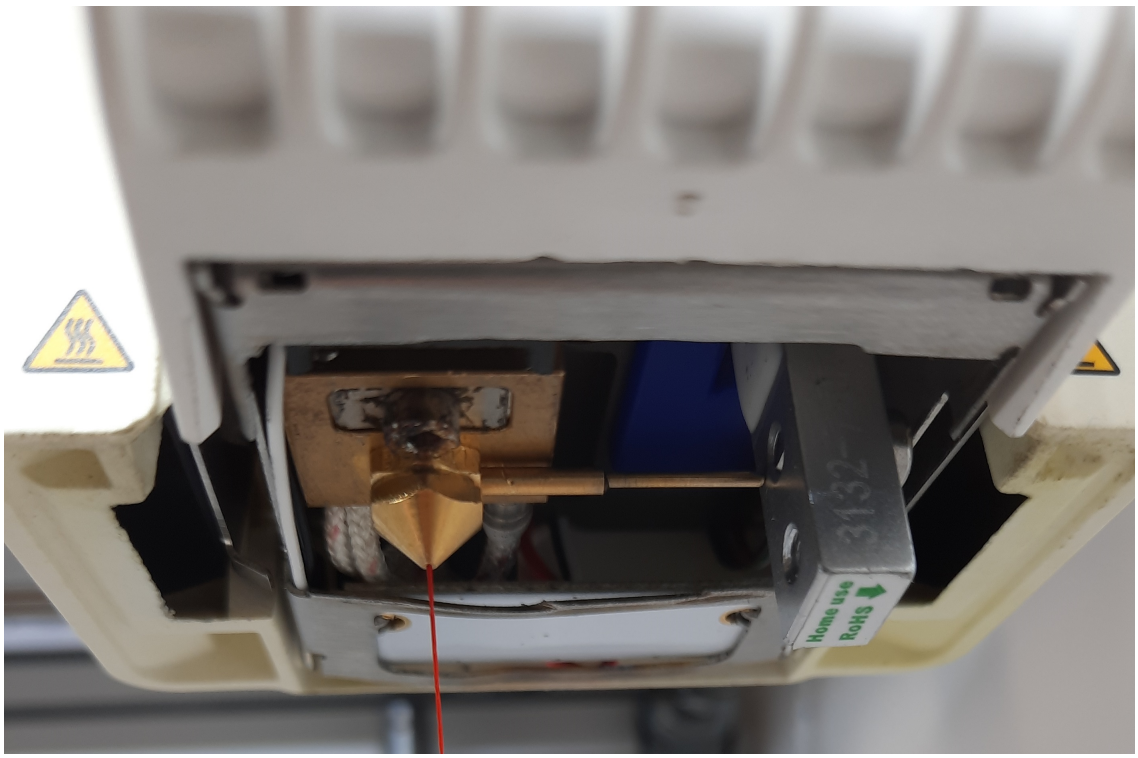


Figure 87: Proof-of-concept test inside the print head of a printer.

The force readings increased at higher flows and returned to zero after resetting the flow to zero. An elaborate investigation is necessary to see if this set-up will work, but the initial test is promising. For example, the influence of print head movement was not investigated, which is crucial when testing in a printer. Alternatively, a printer that has a moveable print bed rather than a moveable print head can be used.

## D.4 Extrudate

Ultimately, to improve print quality, the extrusion flow (flow that comes out the nozzle) has to be controlled in a better way. Currently, there is no defined relation between the pressure inside the nozzle and the amount of polymer that is extruded. It is clear that the pressure is important, as well as the temperature [24]. However, a clear quantification has not been made yet. The relation between pressure and extrusion flow will be dependent on, but not limited to, the temperature, material, back pressure of previous layers, print speed and nozzle type. It is necessary to investigate this further to implement extrusion control.

# E Graphs

## E.1 Viscosity curves

As explained in Appendix B.1, the set point to find the slope of the non-Newtonian region was manually picked. In the following graphs, the set point has been included as a dashed black line.

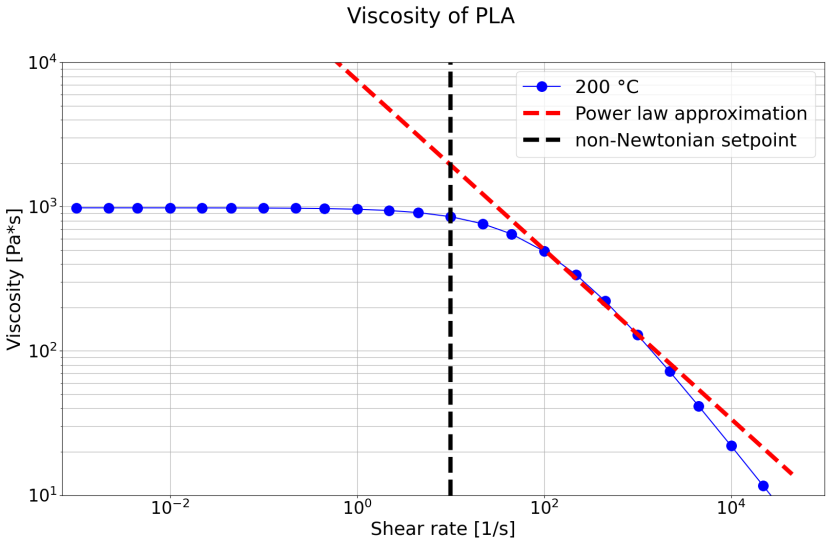


Figure 88: Viscosity curve of PLA at 200 °C.

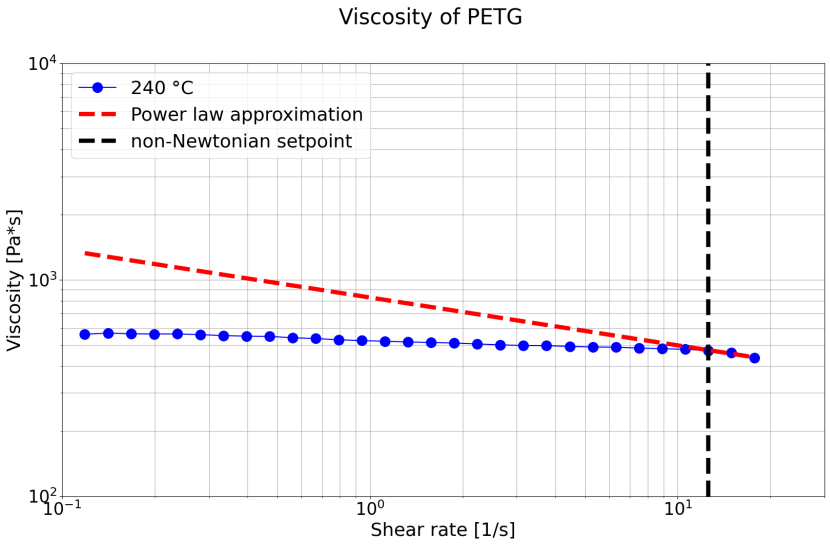


Figure 89: Viscosity curve of PETG at 240 °C.

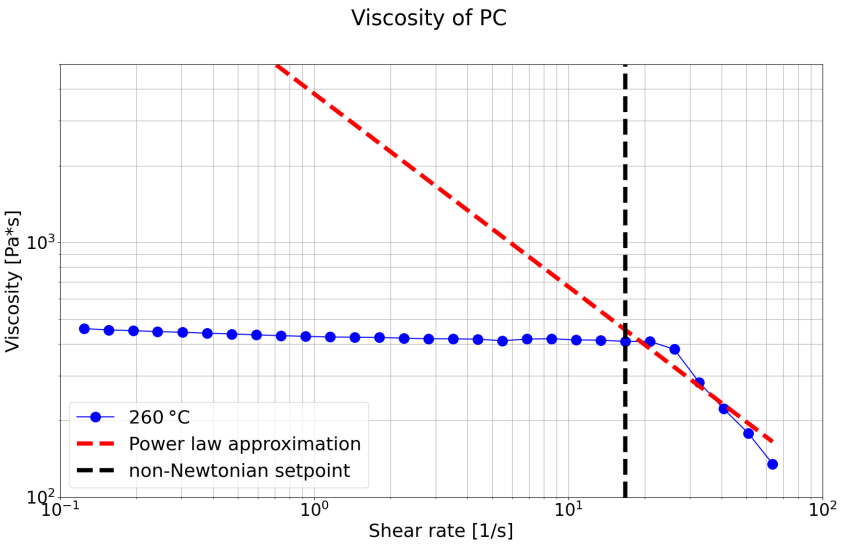


Figure 90: Viscosity curve of PC at 260 °C.

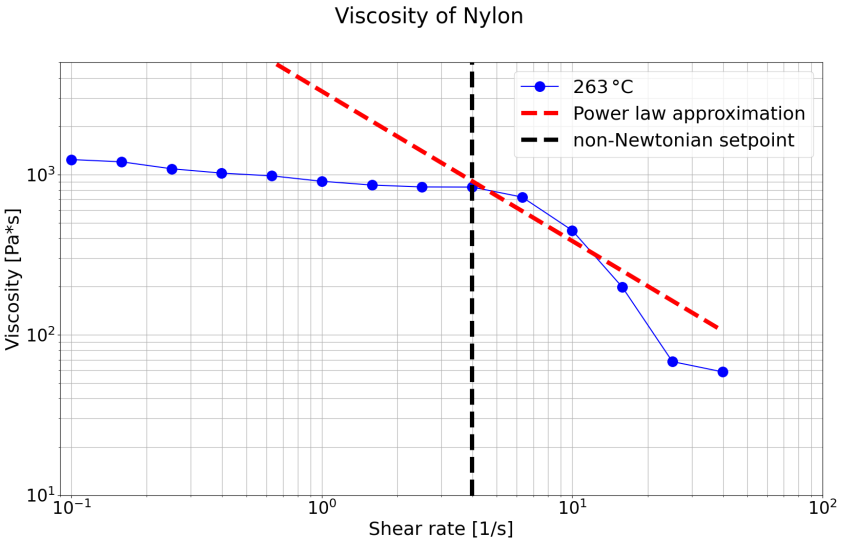


Figure 91: Viscosity curve of Nylon at 263 °C.

## E.2 Pressure graphs

### *E.2.1 Nozzle type 1*

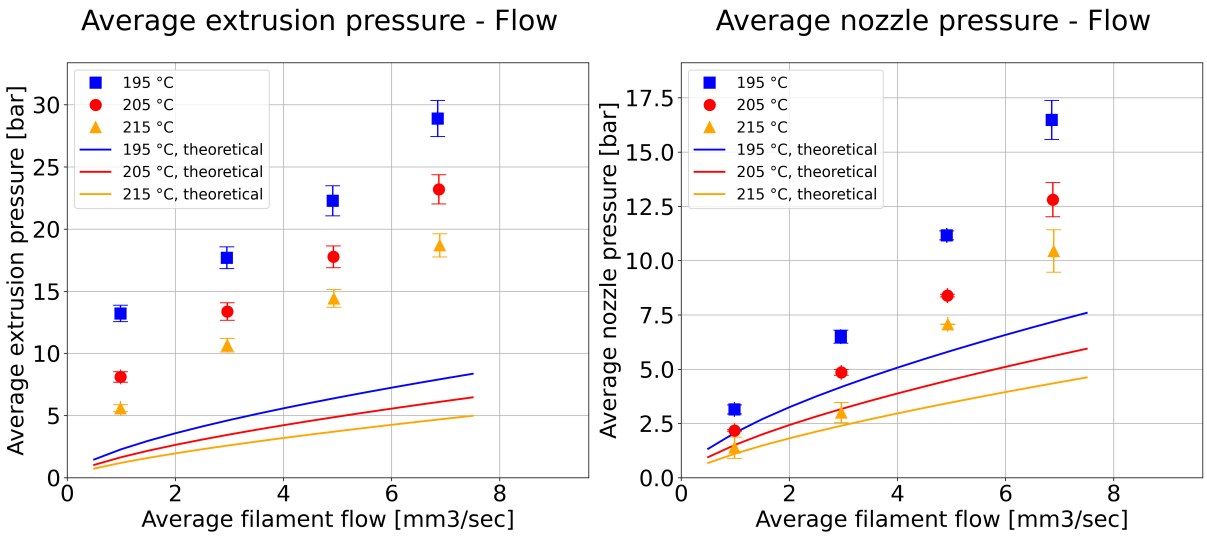


(a) Extrusion pressure.

(b) Nozzle pressure.

Figure 92: Nozzle type 1, PLA.

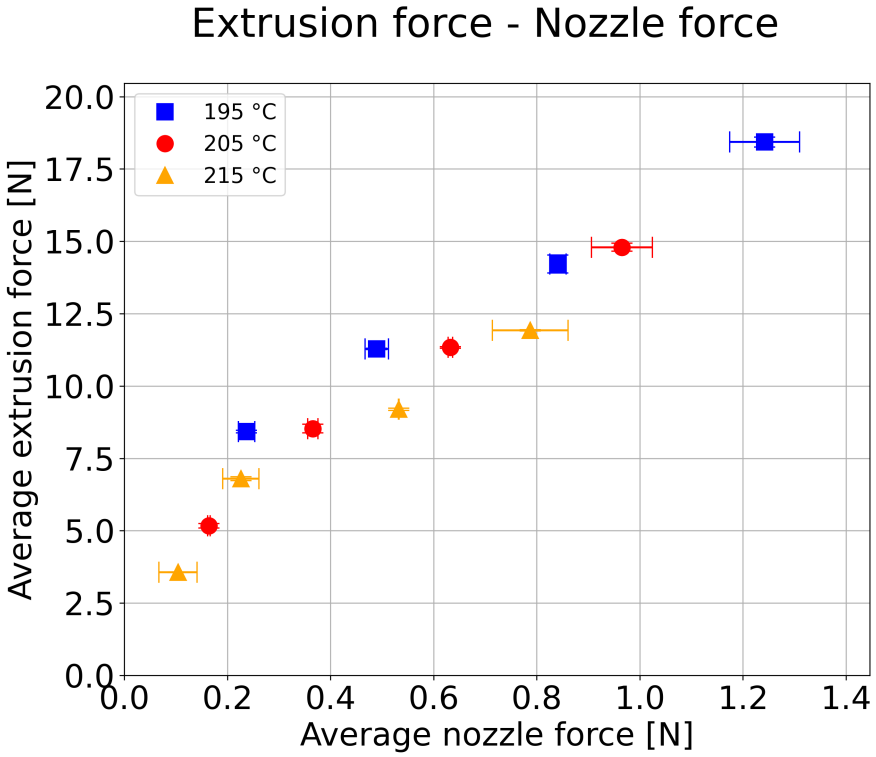


Figure 93: Extrusion force versus nozzle force. Nozzle type 1, PLA.

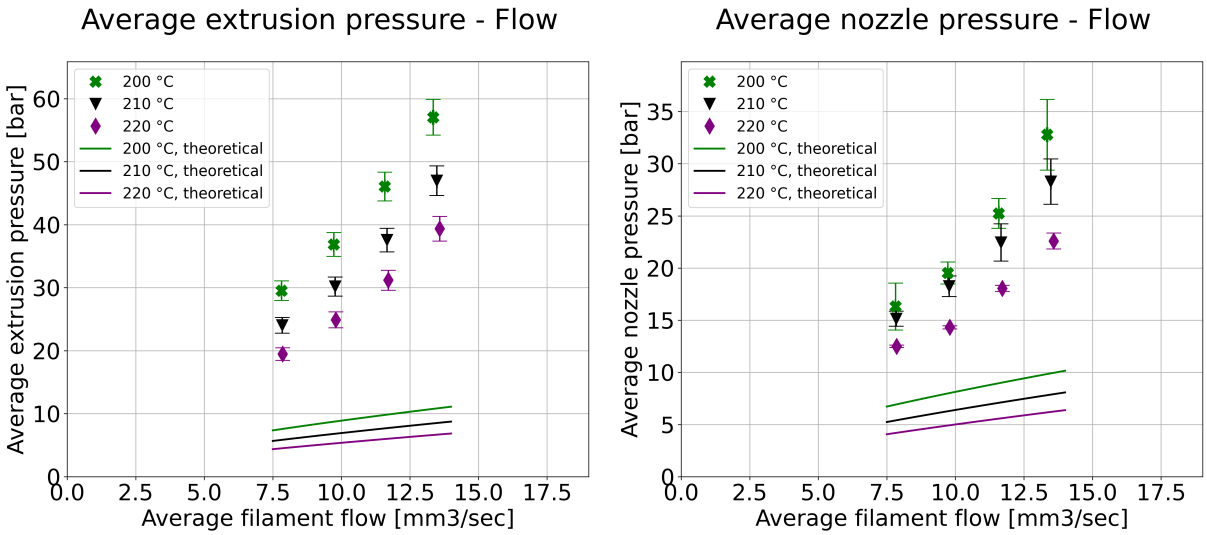


(a) Extrusion pressure.

(b) Nozzle pressure.

Figure 94: Nozzle type 1, PLA.

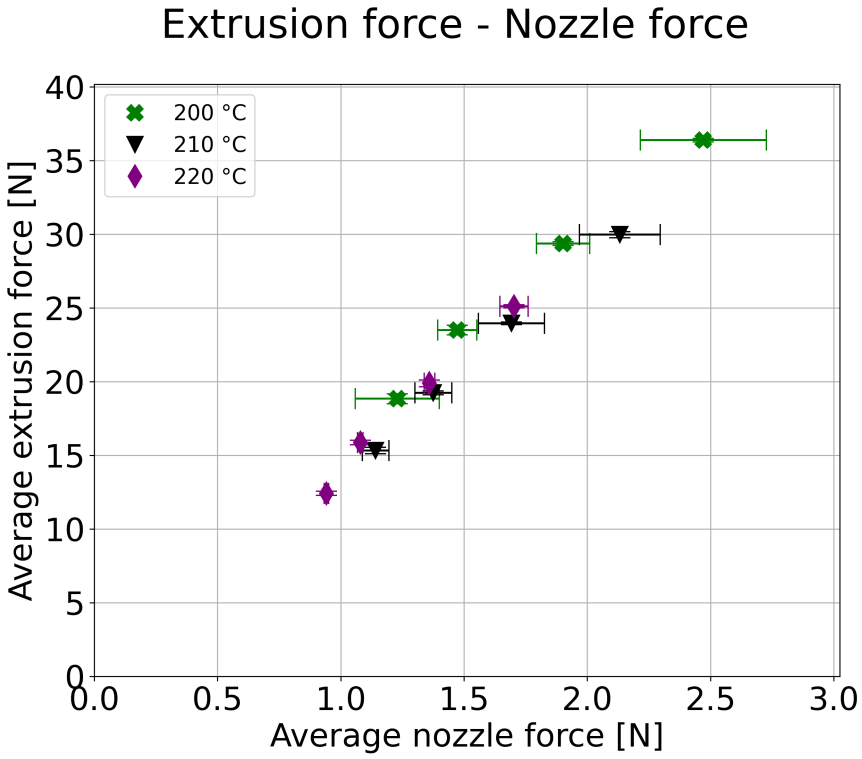


Figure 95: Extrusion force versus nozzle force. Nozzle type 1, PLA.

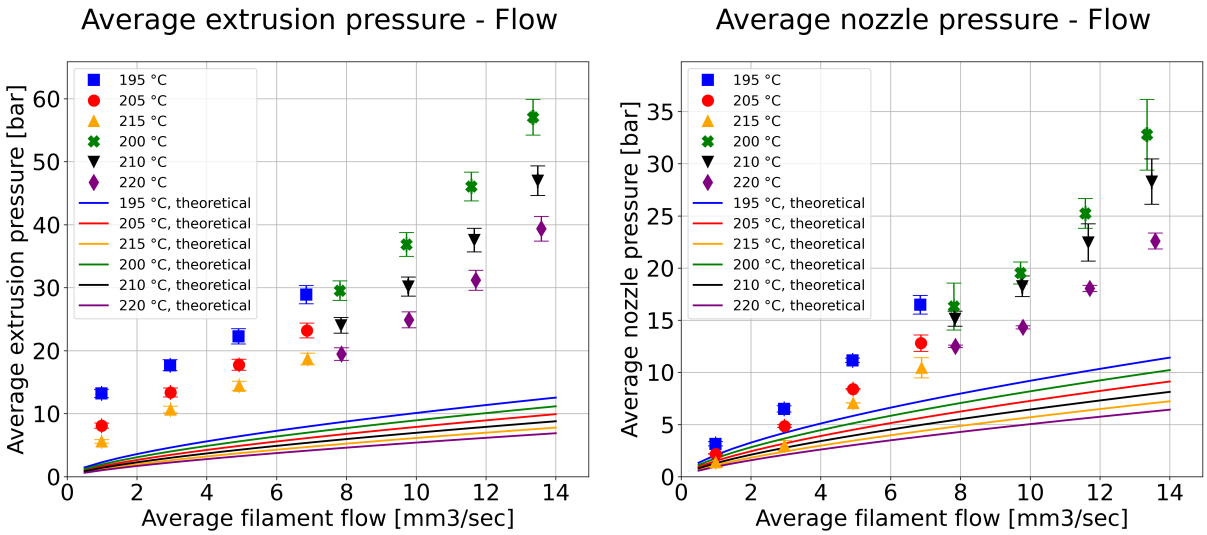


(a) Extrusion pressure.

(b) Nozzle pressure.

Figure 96: Nozzle type 1, PLA.

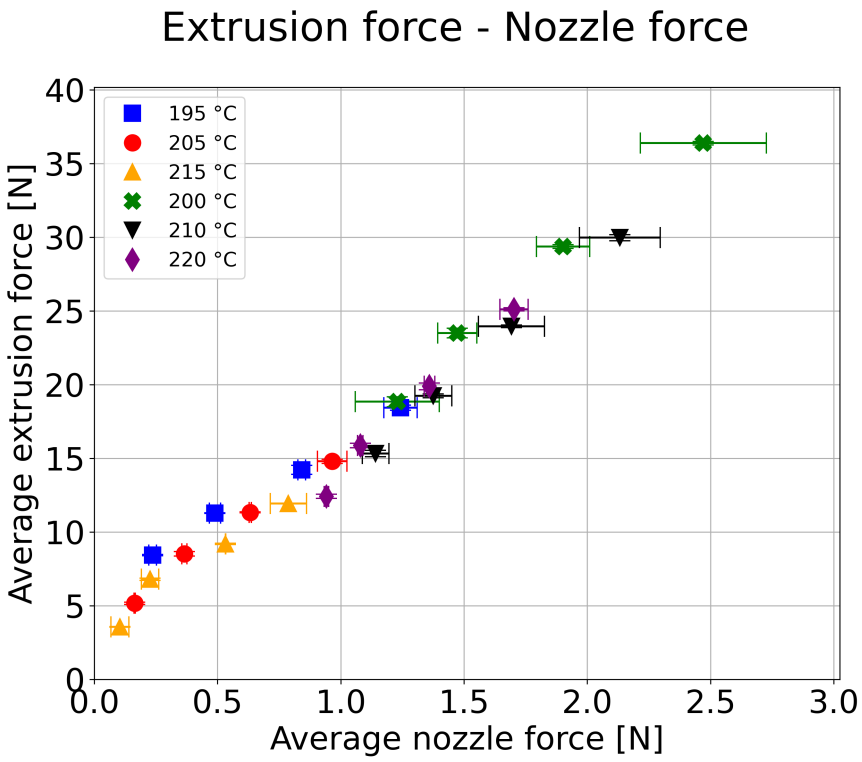


Figure 97: Extrusion force versus nozzle force. Nozzle type 1, PLA.

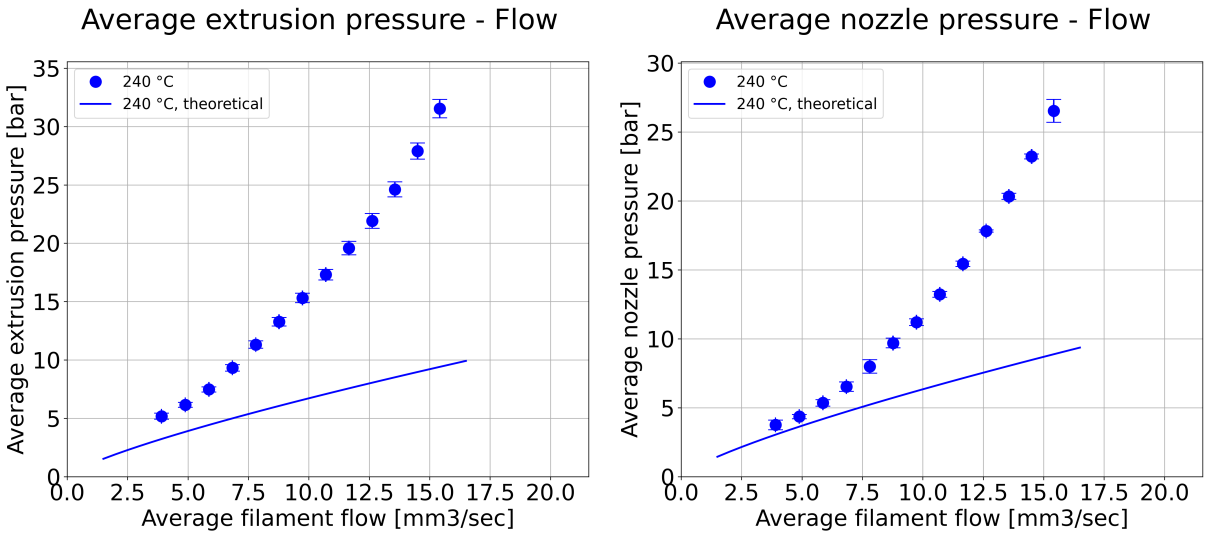


(a) Extrusion pressure.

(b) Nozzle pressure.

Figure 98: Nozzle type 1, PETG.

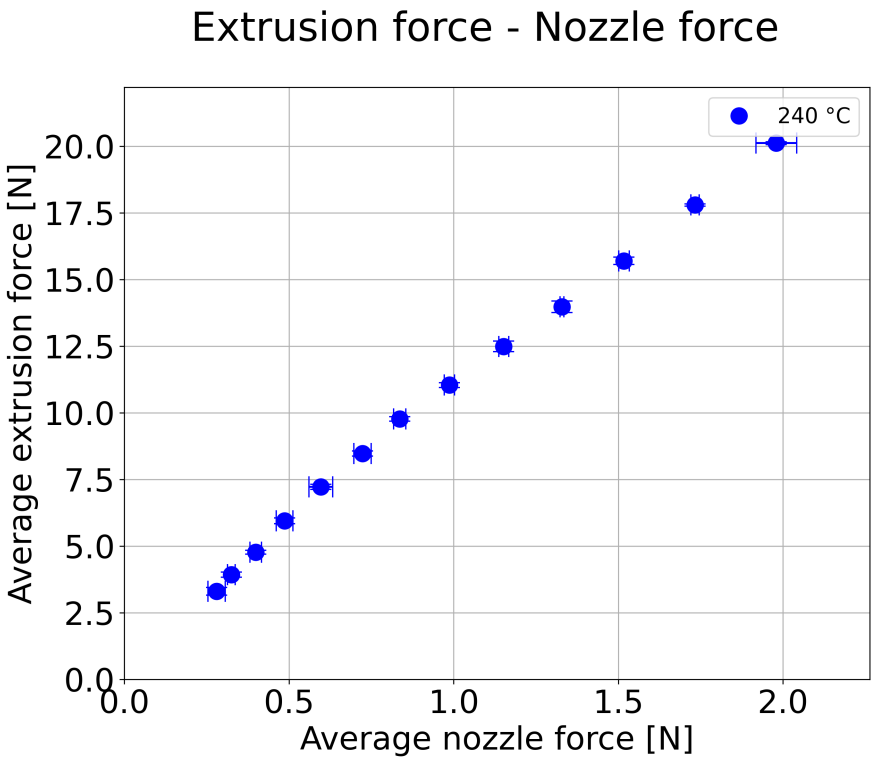


Figure 99: Extrusion force versus nozzle force. Nozzle type 1, PETG.

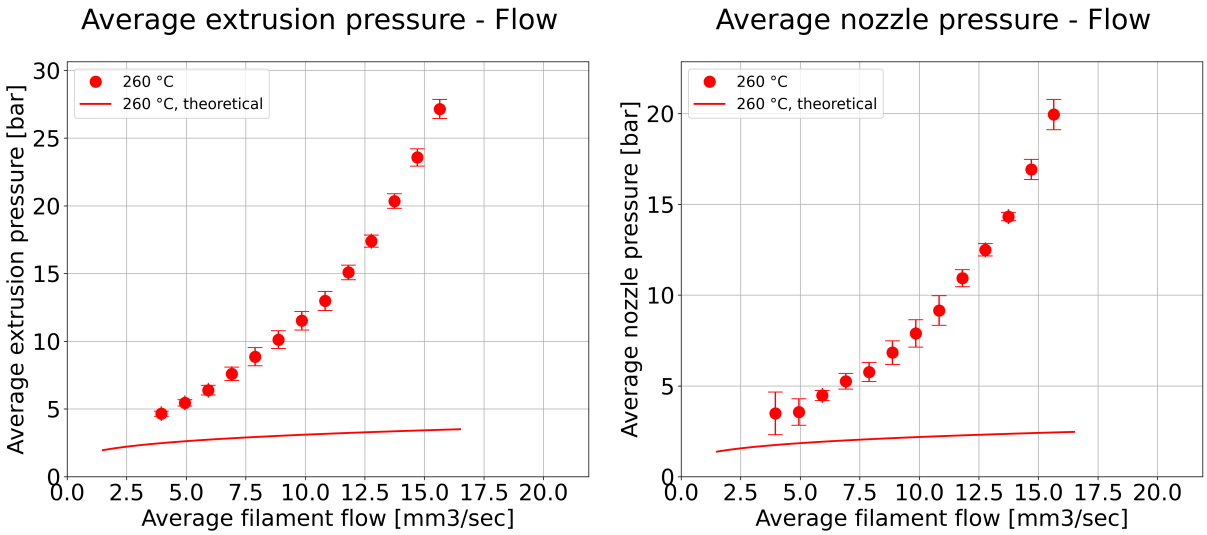


(a) Extrusion pressure.

(b) Nozzle pressure.

Figure 100: Nozzle type 1, PC.

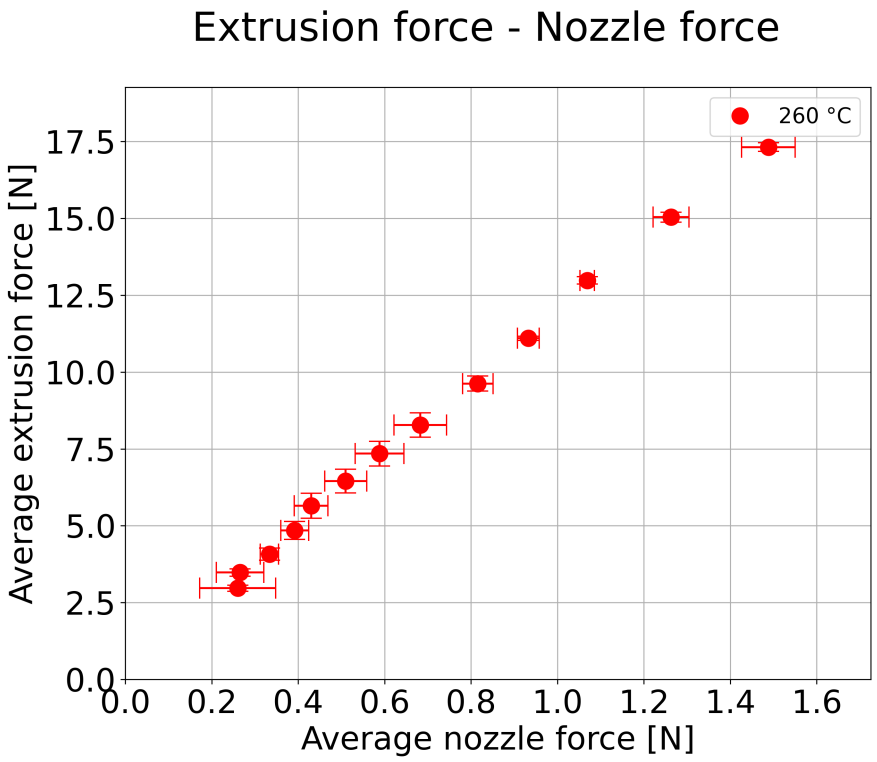


Figure 101: Extrusion force versus nozzle force. Nozzle type 1, PC.

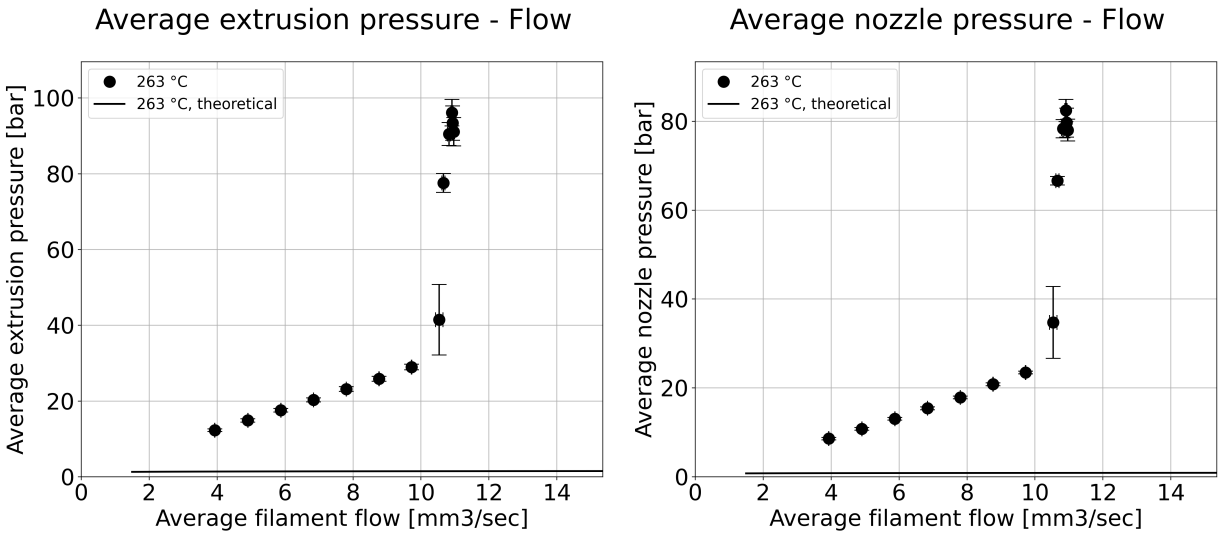


(a) Extrusion pressure.

(b) Nozzle pressure.

Figure 102: Nozzle type 1, Nylon.

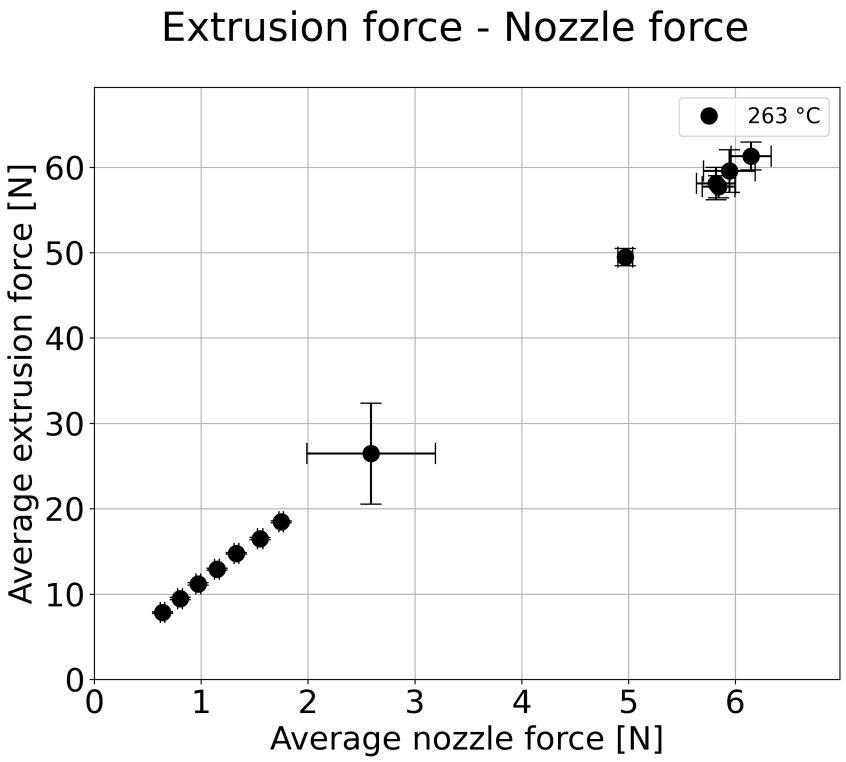


Figure 103: Extrusion force versus nozzle force. Nozzle type 1, Nylon.

### *E.2.2 Nozzle type 2*

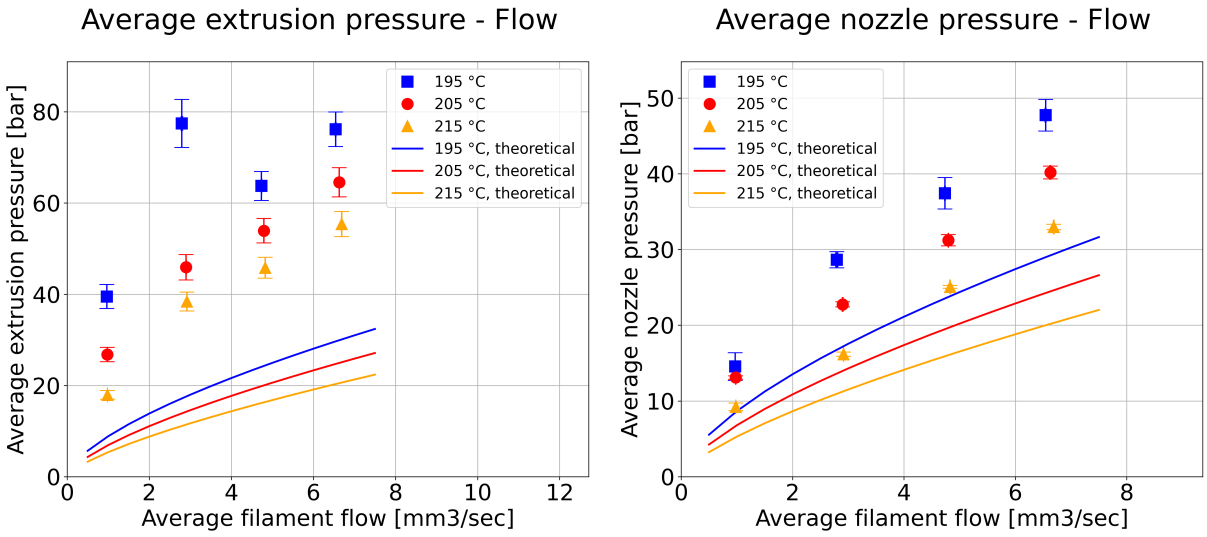


(a) Extrusion pressure.

(b) Nozzle pressure.

Figure 104: Nozzle type 2, PLA.

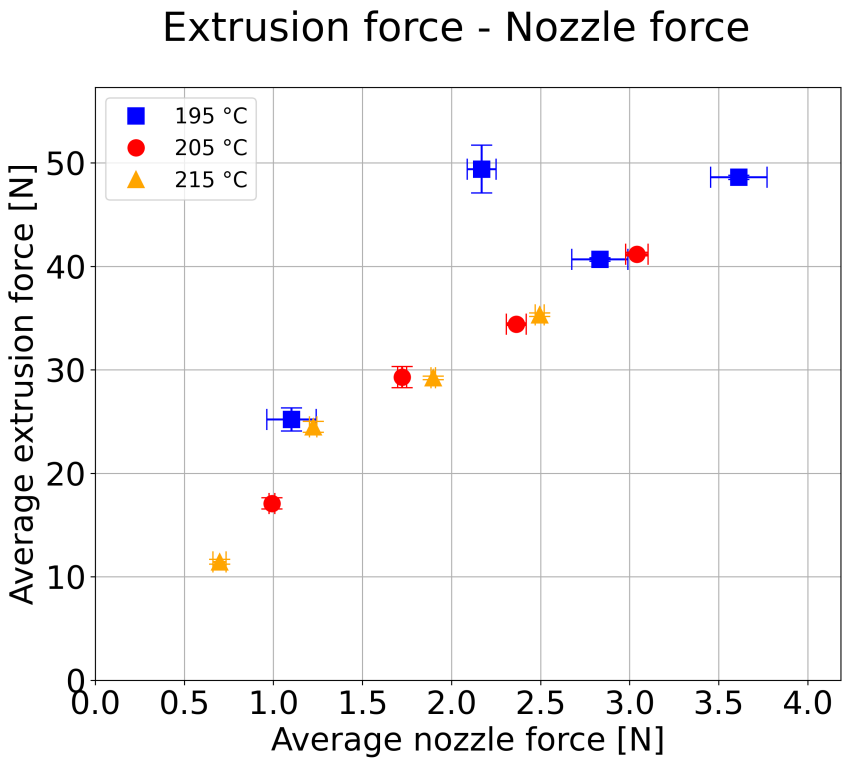


Figure 105: Extrusion force versus nozzle force. Nozzle type 2, PLA.

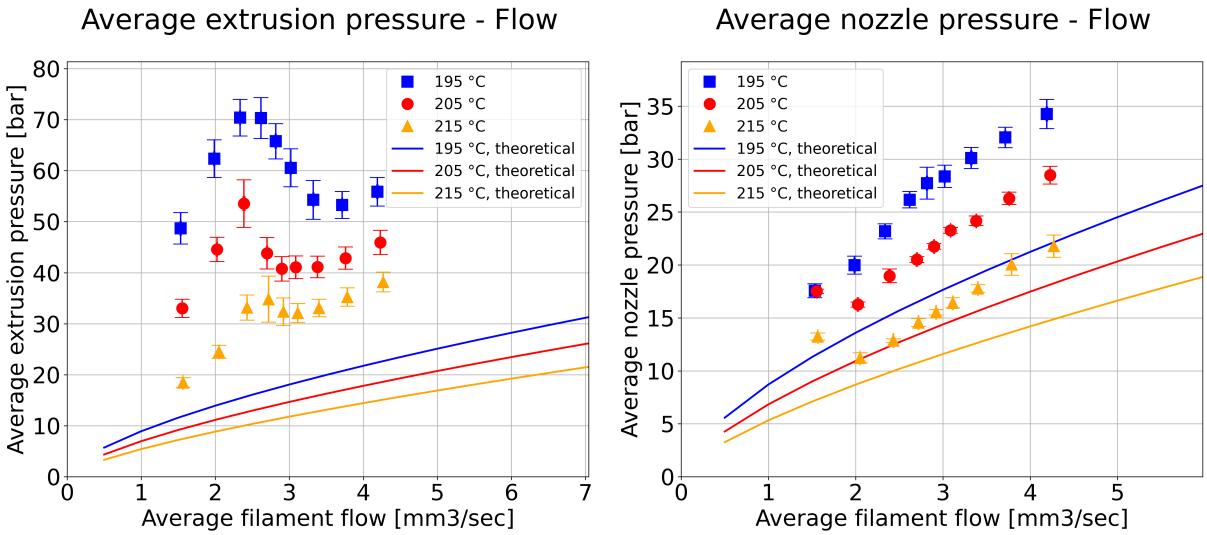


(a) Extrusion pressure.

(b) Nozzle pressure.

Figure 106: Nozzle type 2, PLA.

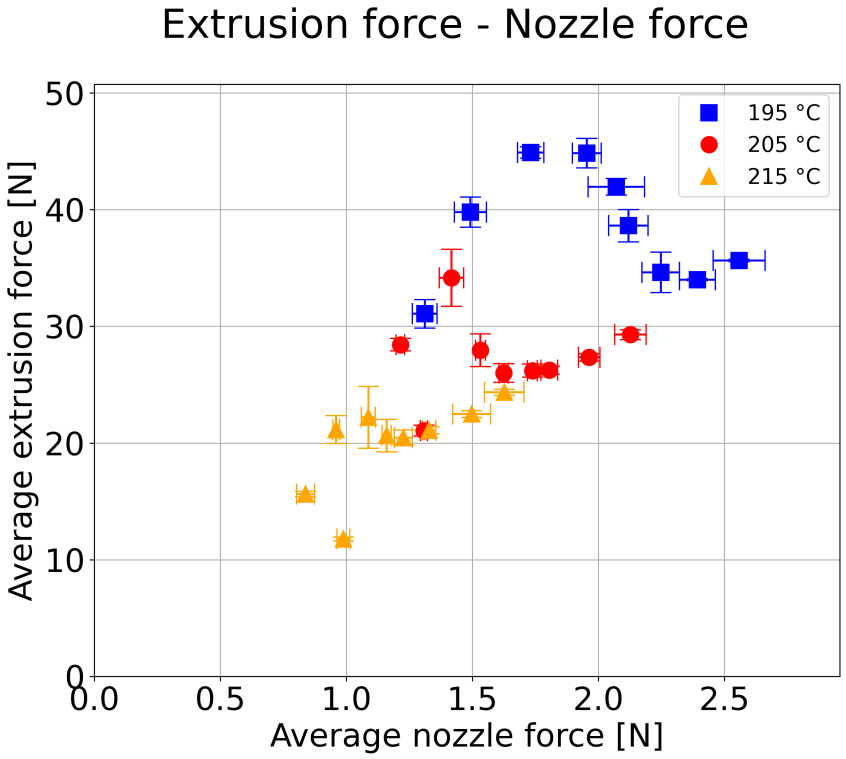


Figure 107: Extrusion force versus nozzle force. Nozzle type 2, PLA.

### *E.2.3 Nozzle type 3*

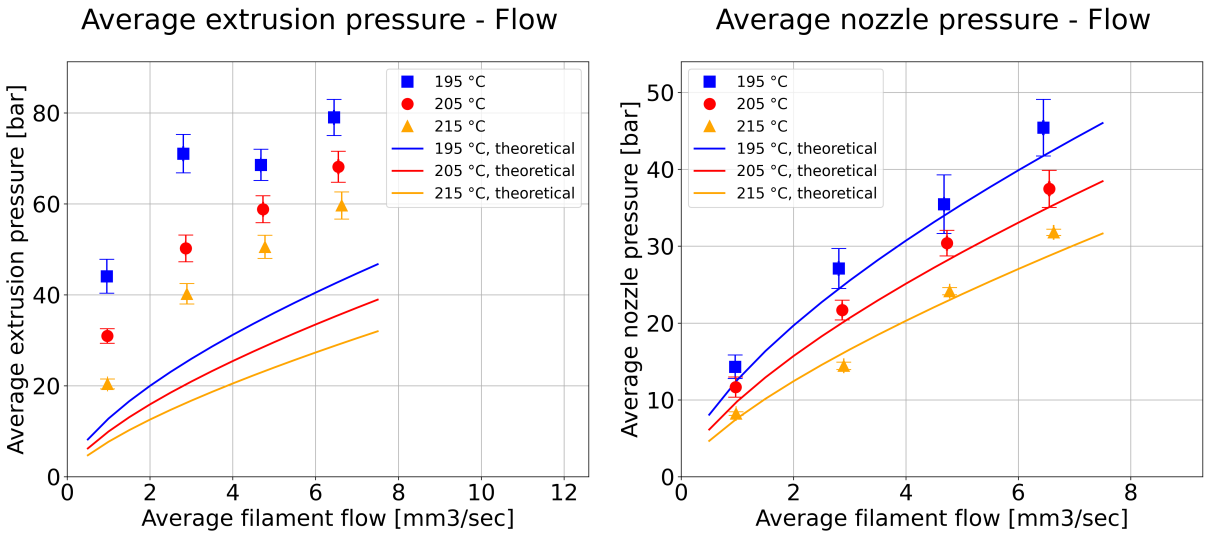


(a) Extrusion pressure.

(b) Nozzle pressure.

Figure 108: Nozzle type 3, PLA.

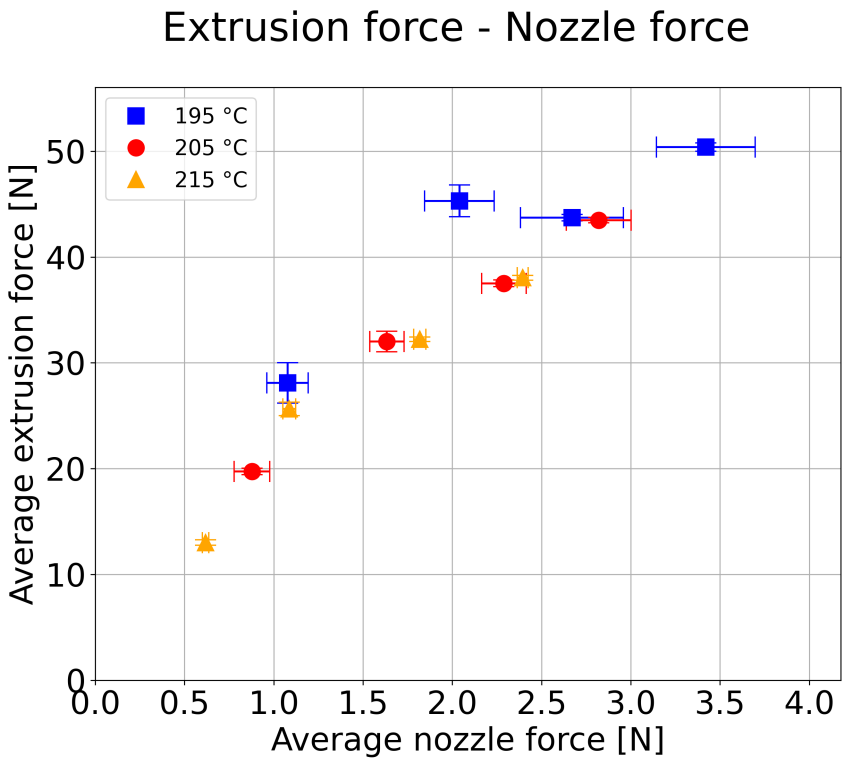


Figure 109: Extrusion force versus nozzle force. Nozzle type 3, PLA.

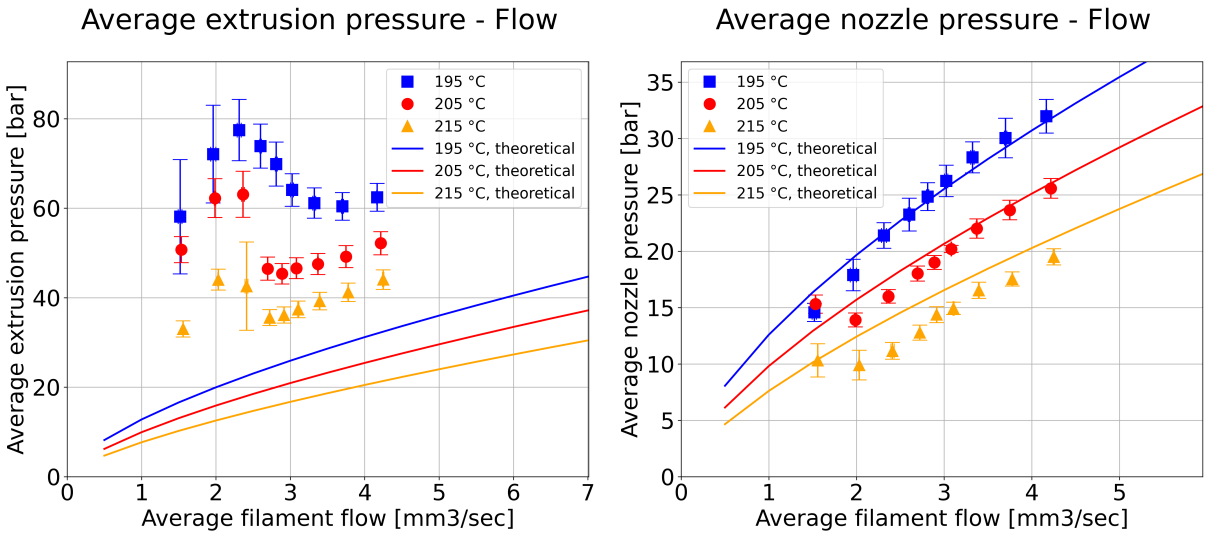


(a) Extrusion pressure.

(b) Nozzle pressure.

Figure 110: Nozzle type 3, PLA.

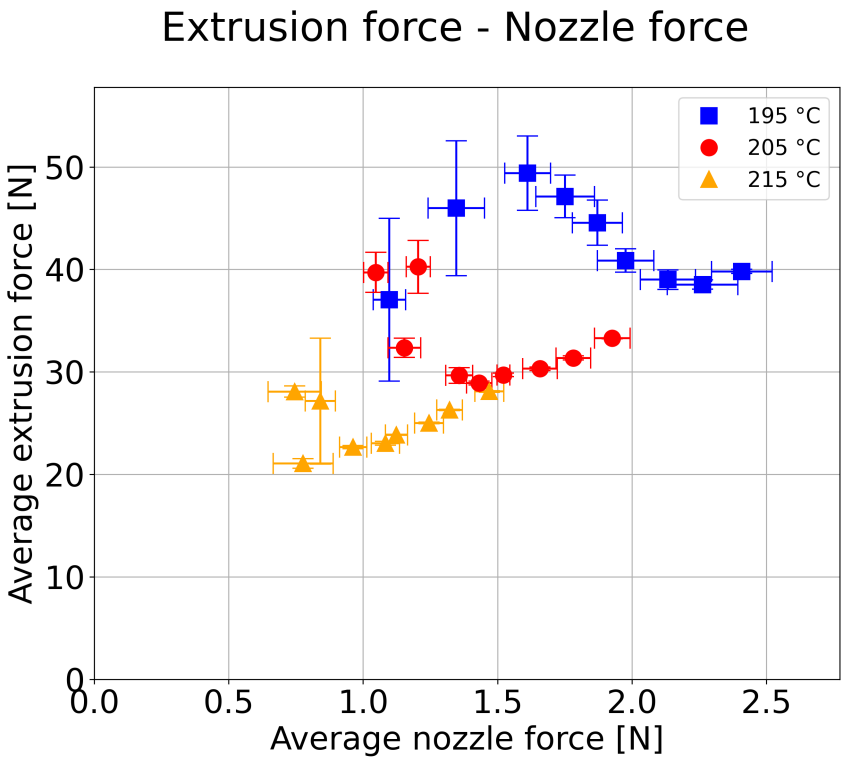


Figure 111: Extrusion force versus nozzle force. Nozzle type 3, PLA.

# F Example code

```
#%% PREPARE EXPERIMENT:
run_time = 2*60        #[sec]
N_repeats = 1          #[-] number of times the test cycle is repeated. NO REPEATS: N_repeats = 0
dia_fil = machine.getFilamentDiameter()
dia_crosss = pi / 4 * dia_fil ** 2

tests = getProcessWindow_UserInput()
n_totaltests = getCountNrOfTests(tests)*(N_repeats+1)
metadata = createMetaDataHeader_All()
experiment = '*' + metadata['Project']['Name'] + '_SOP_static'
metadata['Protocol'] = getMetaDataHeader_ProtocolInputOnce()
metadata['Tests'] = {"Duration":run_time, "Repeats":N_repeats}
metadata['Tests'].update(tests)
variable_output_tuple = tuple([v[0], v[1]] for v in metadata["Connections"].values())

machine.print("### STARTING PROTOCOL: Feeder Characteristics ###")
machine.print("? Check if extrusion force is zero!")
machine.print("# ABORT if you are unsure.")
machine.print(f"# Ready to run {n_totaltests} measurement?")
#FIRST WE SHOULD ASK USER IF EXTRUSION FORCE IS ZERO-ED!!!
#COULD WE CREATE AN INPUTBOX(caption,default text)?

machine.print(f"# Heating up ({list(tests.keys())[0]} [dC]) wait for priming...")
machine.setVariable("Heater 3", "enable", True)
machine.setVariable("Heater 3", "target_temperature", list(tests.keys())[0])
while not machine.isReady("Heater 3"):
    sleep(0.1)

l = 20. #mm Purge liquifier
v = 0.2 #mm/sec
t = l / v #sec210: [1, 2, 4, 6, 8, 10, 12, 14, 16]
machine.print(f"# Purging {l} [mm] during {t} [sec]...")
machine.extrudeAt(v) #start extruding [mm/s]
sleep(t) #sec
machine.extrudeAt(0) #stop extruding
sleep(5)   #add some settling time...

#%% START EXPERIMENT:
machine.print("### STARTING PROTOCOL ###")
n_testnr=0
machine.initializeExperiment(base, experiment)
for n in range(N_repeats+1): # repeat cycles
    machine.print(f"# Repeated tests: {n} of {N_repeats}")
    for tempX, flows in tests.items():
        #machine.print(f"# Set heater to { (tempX-66) } [dC] and wait...") #offset for ceramic core (sometimes)
        machine.print(f"# Set heater to {tempX} [dC] and wait...")
        machine.setVariable("Heater 3", "target_temperature", tempX)
        while not machine.isReady("Heater 3"):
            sleep(0.1)
```

Figure 112: Example code for performing an experiment and saving the data, part 1. See next page...

```
            sleep(0.1)
        for flowX in flows:
            #pre-pare:
            n_testnr = n_testnr + 1
            distanceX = flowX / dia_crosss * run_time #[mm] assuming mm as input unit
            getUpdatedMetaData_CurrentTest(metadata)
            machine.zeroingEncoder("*") #zeroing all encoders
            machine.setVariable("Stepper 1", 'reset', True)  #zeroing feeder

            #start recording:
            machine.startRecording(file_path=None)
            sleep(5) # [sec] including idling time at front
            machine.print(f"# Run ({n_testnr}/{n_totaltests}) at {tempX} [dC] with flow {flowX} [mm3/s]...")
            #cur_pos = machine.getVariable("Stepper 1", "position_meters") * 1000
            s = flowX / dia_crosss * 60 #[mm/min]

            machine.addGCode([f"G1 E{distanceX} F{s}", f"G1 E{distanceX-0.5} F{s}", END_OF_GCODE])
            while not machine.gcodeIsExecuting(): #first need to be sure previous commands are emptied
                pass
            while machine.gcodeIsExecuting(): #now we wait till current gcode is processed.
                pass
            sleep(10) #[sec] including waiting/settling time
            machine.print(f"# End run.")

            machine.stopRecording()
            if machine.aborted:
                break
            ##machine.openExperimentFile(stored) DO NOT USE, SINCE SCRIPTING FILENAME IS UPDATED BY METADATA!!
            machine.openExperimentFile(metadata['File']['Name'])
            machine.addExperimentMetadata(metadata) # put dict here.
            #machine.backupScript() #KHW/KP: does not work. -> check.
            machine.addExperimentConfigs()
            machine.addExperimentLogs()
            machine.addExperimentMeasurements(*variable_output_tuple)
            machine.closeExperimentFile()
            machine.print(f"# File stored.")
        if machine.aborted:
            break
    if machine.aborted:
        break

machine.print(f"## Retract at end of test:")
machine.addGCode([f"G1 E{-2} F{s}", END_OF_GCODE])

machine.print(f"## End of protocol.")
machine.close() #shut down actuators & close.
```

Figure 113: Example code for performing an experiment and saving the data, part 2.

```
for tsX in self.DataSet:
    if tsX.VariableSetIsAnalyzed:  # When there are results, read them:
        sKey = "T" + str(tsX.TS_metaX["Procedure"]["Temperature"]) + "F" +\
               str(round(tsX.TS_metaX['Procedure']['Flow'], 2))
        if not tsX.TS_metaX["Procedure"]["Temperature"] in temperatures:
            temperatures.append(tsX.TS_metaX["Procedure"]["Temperature"])
        if not sKey in myDict:
            myDict[sKey] = {"flowave": list(), "flow":list(), "flowtxt": list(), "force": list(),
                            "force2": list(), "force_std":list(), "force2_std":list()}
        myDict[sKey]["flowave"].append(tsX.TS_results['filament_flow_mean'])
        myDict[sKey]["flow"].append(round(tsX.TS_metaX['Procedure']['Flow'], 2))
        myDict[sKey]["force"].append(tsX.TS_results['extrusion_force_mean'])
        myDict[sKey]["force2"].append(tsX.TS_results['loadcell2_force_mean'])
        myDict[sKey]["flowtxt"].append(str(tsX.TimeSerieID))
        myDict[sKey]["force_std"].append(tsX.TS_results['extrusion_force_std'])
        myDict[sKey]["force2_std"].append(tsX.TS_results['loadcell2_force_std'])

for test in myDict:
    for item in myDict[test]:
        if item == 'flowave':
            flows_to_plot.append(np.mean(myDict[test][item]))
            flow_errors.append(np.std(myDict[test][item]))

        if item == 'force':
            for experiment in myDict[test]["flowtxt"]:
                if int(experiment) in self._GetFailedTests():
                    myDict[test][item].pop((int(experiment) // self._GetNumberOfTests()))
            for element in myDict[test]['force_std']:
                propagate_error.append(element ** 2)
            forces1.append(np.mean(myDict[test][item]))
            force1_errors.append(np.std(myDict[test][item]))

            f = forces1[-1] #F1
            s_f = force1_errors[-1] #sigmaF1

            pressures1.append( f / area_filament )
            pressure1_errors.append( pressures1[-1] * np.sqrt( (s_f/f)**2 +
                                                               (std_area_filament/area_filament)**2 ) )

            propagate_error = []

        if item == 'force2':
            for experiment in myDict[test]["flowtxt"]:
                if int(experiment) in self._GetFailedTests():
                    myDict[test][item].pop((int(experiment) // self._GetNumberOfTests()))
            for element in myDict[test]['force2_std']:
                propagate_error.append(element ** 2)
            forces2.append(np.mean(myDict[test][item]))
            force2_errors.append(np.std(myDict[test][item]))

            f = forces2[-1] #F2
            s_f = force2_errors[-1] #sigmaF2

            pressures2.append( f / area_pin )
            pressure2_errors.append( pressures2[-1] * np.sqrt( (s_f/f)**2 + (std_area_pin/area_pin)**2 ) )

            propagate_error = []

    pressures_to_plot.append( (pressures1[-1] - pressures2[-1]) * 1e-5 )
    pressure_errors.append( (np.sqrt( pressure1_errors[-1]**2 + pressure2_errors[-1]**2 )) * 1e-5 )
```

Figure 114: Example code for plotting a pressure graph, part 1. See next page...

```
    if pressures_to_plot[-1] >= highest_pressure:
        highest_pressure = pressures_to_plot[-1]
        highest_pressure_error = pressure_errors[-1]

if enumOutputFormat.ListOnScreen in listOutputFormat:
    print('Steady State Force - Flow characteristic')

figuresize = (10, 8)
fig, ax = plt.subplots(1, 1, sharex=True, figsize=figuresize)
i = 0
p = []
q = []
index1 = int(self._GetManualInputs()[1])/3
index2 = index1 * 2
for k, v in myDict.items():
    q.append(k[1:4] + ' \u00B0C')
    if enumOutputFormat.ListOnScreen in listOutputFormat:
        print('...', k, str(v['flowave']))
    p.append(ax.errorbar(flows_to_plot[i], pressures_to_plot[i], xerr=flow_errors[i], yerr=pressure_errors[i],
                         linestyle='None', capsize=8, ms=12, marker=GetMarkerStrFromIndex(k[0:4]),
                         color=GetColorStrFromTKey(k[0:4])))
    p[-1][0].set_linewidth(2)
    i += 1

# Include the theoretical force according to Bellini
results = self._GetTheoreticalPressure(temperatures)
bellini = [None] * len(temperatures)
bellini_label = []
i = 0
for T in temperatures:
    flows = results[T]["flows"]
    k = "T" + str(T)
    pressures = results[T]["pressures1"]
    bellini[i], = ax.plot(flows, pressures, label=k[1:] + ' \u00B0C, theoretical',
                          color=GetColorStrFromTKey(k), linewidth=2)
    bellini_label.append(k[1:] + ' \u00B0C, theoretical')
    i += 1

ax.grid()
ax.legend([(p[0][0]), (p[int(index1)][0]), (p[int(index2)][0]), (bellini[0]), (bellini[1]), (bellini[2])],
          [q[0], q[int(index1)], q[int(index2)], bellini_label[0], bellini_label[1], bellini_label[2]],
          handler_map={tuple: HandlerTuple(ndivide=None)}, loc=0, fontsize=16)
plt.axis([0, flows_to_plot[-1] * 1.4, 0, (highest_pressure+highest_pressure_error) * 1.1])
fig.suptitle('Liquefier pressure drop - Flow', fontsize=30)
ax.set_ylabel('Liquefier pressure drop [bar]', fontsize=24)
ax.set_xlabel('Average filament flow [mm3/sec]', fontsize=24)
for label in (ax.get_xticklabels() + ax.get_yticklabels()):
    label.set_fontsize(24)

if enumOutputFormat.PlotOnScreen in listOutputFormat:
    plt.show()
if enumOutputFormat.SaveToPDF in listOutputFormat:
    plt.savefig(self.PDFreport, format='pdf')
if enumOutputFormat.SaveToPNG in listOutputFormat:
    plt.savefig(self.ExportFolder + '/graphs/' + self.DataSet[0].TS_metaX['Protocol'][
        'DatasetID'] + '_Pliquefier-flow-Average-Bellini.png', transparent=False, dpi=300)
if not (enumOutputFormat.PlotOnScreen in listOutputFormat):
    plt.close()
# b: Predict nozzle friction, based on polinomal(s)
# c: Create nozzle characteristic (pressure versus flow)
return True
```

Figure 115: Example code for plotting a pressure graph, part 2.